III-NITRIDE ULTRAVIOLET LASER

A Ph.D. Dissertation
Presented to
The Academic Faculty

by

Xiaohang Li

In Partial Fulfillment
of the Requirements for the Degree
Doctor of Philosophy in the
School of Electrical and Computer Engineering

Georgia Institute of Technology
August 2015

III-NITRIDE ULTRAVIOLET LASER

Approved by:

Dr. Russell D. Dupuis, Advisor
School of Electrical and Computer Engineering
Georgia Institute of Technology

Dr. Shyh-Chiang Shen
School of Electrical and Computer Engineering
Georgia Institute of Technology

Dr. P. Douglas Yoder
School of Electrical and Computer Engineering
Georgia Institute of Technology

Dr. Stephen Ralph
School of Electrical and Computer Engineering
Georgia Institute of Technology

Dr. Fernando A. Ponce
Department of Physics
Arizona State University

Date Approved: July 21, 2015

ACKNOWLEDGEMENTS

I would like to express my sincerest gratitude to those who have help me along the way in making this work and dissertation possible. First and foremost, I would like to thank my advisor, Dr. Russell D. Dupuis. Dr. Dupuis has provided me invaluable academic guidance, state-of-the-art research facilities, and freedom of thought to conduct truly cutting-edge research projects in this field. His work ethic, professionalism, and love of science have been always leading-by-example and will continue to inspire me in the future. I am very proud and fortunate to work with him in the Advanced Materials and Devices Group (AMDG) at Georgia Tech.

I would like to thank my committee members, Dr. P. Douglas Yoder, Dr. Shyh-Chiang Shen, Dr. Fernando A. Ponce and Dr. Stephen Ralph. Some of their groups have been primary collaborators of my research projects. Their great efforts are indispensable for the progress and achievement. They have also given me valuable comments and suggestions for this dissertation. It is my great honor to have their names on this dissertation.

I am very thankful to my current and past colleagues in AMDG: Dr. Theeradetch Detchprohm, Dr. Jae-Hyun Ryou, Dr. Hee-Jin Kim, Dr. Suk Choi, Dr. Zachary Lochner, Dr. Jeomoh Kim, Mi-Hee Ji, Yuh-Shiuan Liu, Devin James Justice, Nordine Sebki, and Rumin Gong, as well as the staff members at Georgia Tech's Institute of Institute for Electronics and Nanotechnology. They have been very supportive and helpful for the advance of my research. There have been great discussions and joys working with them.

In addition, I am grateful to know and work with the members in the research groups of Dr. Andrew A. Allerman at Sandia National Laboratory, Dr. Michael Wraback

at Army Research Laboratory, Dr. Michael Kneissl at Technical University of Berlin, Dr. Peter Parbrook at University College Cork, and Dr. Samuel Graham at Georgia Tech. I also want to thank Dr. Zhixuan Xia for his help and advice before I came to Atlanta. Moreover, I appreciate the guidance and support from my former advisors, Dr. Zhiping Zhou at Peking University, Dr. Yonghong Xiong at Huazhong University of Science and Technology, and Dr. Nelson Tansu at Lehigh University. They have brought me into the scientific research and given me numerous valuable advice.

Moreover, I sincerely appreciate the financial support from the federal agencies and organizations that have sponsored my works, including but not limited to, Georgia Tech, National Science Foundation, Department of Energy, Defense Advanced Research Projects Agency, IEEE Photonics Society, SPIE-the International Society for Optics and Photonics, Steve W. Chaddick Fellowship Endowment Fund, Georgia Research Alliance, Anne Robinson Clough International Student Endowment Fund, and Edison Innovation Foundation. Without them, my research activities would not have been viable.

Finally, I would like to thank my family. My parents have given me their unconditional love and support in my life. My wife Guangyu has been my strongest supporter in this challenging journey of pursuing the doctoral degree in a distant city. There have been countless blessings and encouragement from all the other family members. Your love has been the power source of my efforts.

TABLE OF CONTENTS

LIST OF TABLES

LIST OF FIGURES

Page

SUMMARY

Coherent deep-ultraviolet (DUV) lasing light from compact semiconductor devices is expected to have numerous applications in material processing, data storage, sterilization, communication and biochemical sensing. Because of direct bandgaps and a proper bandgap range, III-nitride semiconductors (III-nitrides) are the materials of choice for generation of DUV lasing. This dissertation starts with brief introductions to III-nitrides and III-nitride lasers. Then it discusses various pioneering studies in demonstrating III-nitride DUV lasers on sapphire and AlN substrates by optical pumping, which is a critical milestone in the pursuit of electrically-pumped DUV laser diodes (LDs).

The first study (Chapter 3) focuses on the growth of AlGaN heterostructure on the bulk AlN substrate for optical pumping experiments. The AlN substrate is promising for the growth of DUV lasers because it has a very low dislocation density of ~10^5 cm^{-2} and close lattice with high-Al AlGaN. The heterostructures were epitaxially grown by metalorganic chemical vapor deposition (MOCVD). A pulsed 193-nm excimer laser was used for optical pumping at room temperature (RT). DUV lasing at 266.0 nm was obtained. The threshold pumping power density of the lasing was 124 kW/cm^2, which is comparable with the state-of-the-art laser emitting at similar wavelengths. Transverse electric (TE) polarization dominated the laser emission above threshold. This study demonstrates excellent candidacy of the AlN substrate for electrically-driven DUV diode lasers.

The development of DUV lasers on sapphire is of particular importance and interest. This is because on one hand, the sapphire substrate has been employed as the primary substrates to mass-produce III-nitride devices such as visible light-emitting diodes (LEDs) and LD. Therefore it is much more inexpensive and scalable compared with the

AlN and SiC substrates. On the other hand, short-wavelength (< 260 nm) DUV lasers on sapphire had not been demonstrated prior to the works leading to this dissertation. Since the AlN layer is transparent to DUV emission and has close lattice constants to III-nitrides, it is used as a template layer between the sapphire and laser structure.

The second study (Chapter 4) focuses on the growth of AlGaN heterostructure on the AlN layer on sapphire substrate (AlN/sapphire template) for optical pumping experiments. The dislocation density of AlN layer is estimated to be ~10^{10} cm^{-2} by X-ray diffraction (XRD). The heterostructure was epitaxially grown by MOCVD. The pulsed 193-nm excimer laser was used for optical pumping at RT. Superluminescence at 259.7 nm from surface emission of AlGaN multiple quantum wells (MQWs) on the sapphire substrate was achieved, which represented superluminescence with the shortest wavelength from the AlGaN heterostructure on sapphire. With further efforts in reducing dislocation density, the AlN/sapphire template is expected to be used to demonstrate low-threshold DUV lasers.

As lasing requires population inversion and a net positive gain, it is crucial that a laser structure with a relatively low dislocation density is developed on sapphire. Assuming the laser structure is fully strained to the AlN template layer, the dislocation density of the AlN template layer largely determines that of the laser structure. Therefore it is crucial to obtain AlN layers on sapphire with relatively low dislocation density. Previously, AlN/sapphire templates with a relatively low dislocation densities had been achieved by a few groups by using complex techniques with high growth temperatures of over 1200 ^{o}C, which however, cannot be applied to industrial settings because most of the large-scale

MOCVD systems cannot reach such high temperatures. The third (Chapter 5) and fourth (Chapter 6) studies were conducted to address this issue.

In the third study (Chapter 5), temperature dependence of crystalline quality of AlN layers at 1050-1250 ^{o}C with a fine increment step of 18 ^{o}C was studied. The AlN layers were grown on (0001) sapphire substrates by MOCVD and characterized by XRD ω-scans and atomic force microscopy (AFM). At 1050-1068 ^{o}C, the templates exhibited poor quality with surface pits and higher XRD (002) and (102) full-width at half maximum (FWHM) because of insufficient Al atom mobility. At 1086 ^{o}C, the surface became smooth suggesting sufficient Al atom mobility. Above 1086 ^{o}C, the (102) FWHM and thus edge dislocation density increased with temperatures which may be attributed to the shorter growth mode transition from three-dimension (3D) to two-dimension (2D). Above 1212 ^{o}C, surface macro-steps were formed due to the longer diffusion length of Al atoms than the expected step terrace width. The edge dislocation density increased rapidly above 1212 ^{o}C, indicating this temperature may be a threshold above which the impact of the transition from 3D to 2D is more significant. The (002) FWHM and thus screw dislocation density were insensitive to the temperature change. This study suggests that high-quality AlN/sapphire templates may be potentially achieved at temperatures as low as around 1100 ^{o}C which is accessible by most of the III-nitride MOCVD systems.

The fourth study (Chapter 6) is a natural transition of the second study (Chapter 4). In this study, I developed a three-step method to grow high-quality planar AlN layers on sapphire substrates at relatively low temperatures by MOCVD without the use of high temperature of over 1130 ^{o}C, epitaxial lateral overgrowth (ELO) or pulse atomic layer epitaxy (PALE) methods. The three-layer AlN structure comprised a 15-nm thick buffer

layer, a 50-nm thick intermediate layer, and a 3.4-μm thick AlN layer grown at 930, 1130, and 1100 ^{o}C sequentially on the (0001) sapphire substrate. The resulting AlN layer had smooth surfaces with well-defined terraces and low root-mean-square (RMS) roughness of 0.50 and 0.07 nm for 20×20 and 1×1 μm^2 AFM scans. Band-edge emission was observed at 208 nm by RT photoluminescence (PL) measurements. The total threading dislocation density was 2.5×10^9 /cm^2 determined by transmission electron microscopy (TEM), which is comparable to those of some AlN layers recently grown at significantly higher temperatures. Growth evolution was studied and correlated to the TEM results. The residual impurity concentrations were comparable to those of AlN layers grown at higher temperatures, i.e., 1200-1600˚C. This study demonstrates the high quality AlN layers on sapphire substrates can be grown at achievable temperatures for most of the modern MOCVD systems.

As mentioned earlier, surface superluminescence was demonstrated by optically pumping AlGaN heterostructures grown on the relatively poor quality AlN layers on sapphire in the second study (Chapter 4). In the fifth study (Chapter 7), the use of high quality AlN layers on sapphire developed in the fourth study (Chapter 6) help demonstrate optically-pumped DUV lasing with low threshold from AlGaN heterostructures. The epitaxial layers were grown pseudomorphically by MOCVD on (0001) sapphire substrates. Stimulated emission was observed at wavelengths of 256 and 249 nm with thresholds of 61 and 95 kW/cm^2 at RT, respectively. The thresholds are comparable to the reported state-of-the-art AlGaN MQW DUV lasers grown on bulk AlN substrates emitting at 266 nm. These low thresholds are attributed to the optimization of active region and waveguide layer as well as the use of high-quality AlN/sapphire templates. The stimulated emission

above threshold was dominated by TE polarization. This work demonstrates the potential candidacy of sapphire substrates for DUV diode lasers.

The six study (Chapter 8) is an extension of the fifth study (Chapter 7) into a shorter wavelength region with a different optical polarization property. In this study, I demonstrated transverse-magnetic (TM) dominant DUV stimulated emission from optically-pumped AlGaN MQW lasers grown pseudomorphically on an AlN/sapphire template by means of PL at RT. The TM-dominant stimulated emission was observed at wavelengths of 239, 242, and 243 nm with low thresholds of 280, 250, and 290 kW/cm^2, respectively. In particular, the lasing wavelength of 239 nm is shorter compared to other reports for AlGaN lasers grown on foreign substrates including sapphire and SiC. The peak wavelength difference between the TE-polarized emission and TM-polarized emission was approximately zero for the lasers in this study, indicating the crossover of crystal-field split-off hole (CH) and heavy-hole (HH) valence bands. The rapid variation of polarization between TE- and TM-dominance versus the change in lasing wavelength from 243 to 249 nm can be attributed to a dramatic change in the TE-to-TM gain coefficient ratio for the sapphire-based DUV lasers in the vicinity of TE-TM switch.

While the previous studies are applicable to both edge-emitting and vertical cavity surface-emitting lasers (VCSELs), the seventh study (Chapter 9) mainly concerns VCSEL. As compared with DUV edge-emitting lasers, development of DUV VCSELs has stalled. This is largely due to lack of III-nitrides for DUV distributed Bragg reflectors (DBRs). This study aimed to grow single-phase wurtzite BAlN materials with high-B content by MOCVD. Such materials are expected to be optically transparent, and have large refractive index contrast and close lattice with high-Al AlGaN materials. MOCVD was used to grow

50-nm thick BAlN layers on 3-μm AlN template layers on (0001) sapphire substrates at various growth conditions. Single-phase wurtzite crystallinity with B contents up to 10% was demonstrated.

1 INTRODUCTION TO III-NITRIDES AND GROWTH PROCESS

Binary, ternary and quaternary alloys of III-nitride compound semiconductors (III-nitrides) $In_xAl_yGa_{1-x-y}N$ have attracted numerous interests from academic and industrial communities in recent decades. Because of the direct bandgap at gamma point of Brillouin zone (BZ), they are recognized as the most promising semiconductor family for fabricating efficient, reliable and compact optical devices including light-emitting diodes (LEDs) and laser diodes (LDs) in the deep ultraviolet (DUV) to infrared (IR) spectral range of about 210-1770 nm. In addition, because of large bandgap, the III-nitrides have high breakdown voltages, high electron mobility and saturation velocity, which are ideal for high-power and high-temperature microwave applications such as heterojuction bipolar transistors and high-electron-mobility transistors. Moreover, the larger band gap means that the performance of GaN transistors can sustain at higher temperatures than silicon transistors.

The successful development of near UV to green III-nitride LEDs and LDs in the spectral range of ~ 400-530 nm in the last three decades has already led to revolutionary progress in the applications such as lighting, electronic display, and optical data storage. However, relatively low performance of III-nitride LEDs and LDs in the UV spectral range of shorter than 400 nm especially DUV range of 210-280 nm still hinders the progress in the applications including germicidal disinfection, bio-sensing, non-line-of-sight communication, and ultra-high density optical storage.

1.1 Basic III-nitride properties

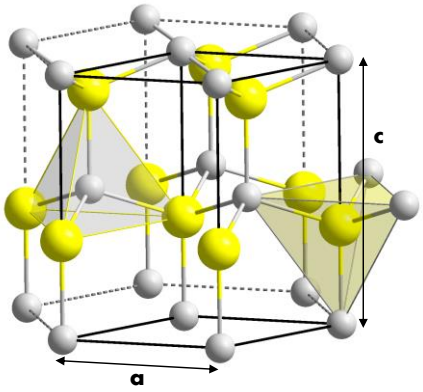

Figure 1. An exemplary crystal structure of wurtzite III-nitrides where the yellow and grey dots represent group-III and nitrogen atoms, respectively.

III-nitrides can have crystalline structures of the wurtzite (WZ), zinc blende (ZB), and rock salt [1]. The ZB structure is meta-stable can merely be stable for the thin films grown on {011} planes of cubic substrates such as Si, SiC, MgO, and GaAs, wherein the topological compatibility compensates the intrinsic tendency to form the WZ structure. The rock salt structure is only existent at high pressures. Therefore, the most common III-nitrides have a WZ structure because thermodynamic stability of the WZ structure is higher than that of the ZB or rock salt structures and the WZ structure is stable under ambient conditions.

Figure 1 shows an exemplary crystal structure of the WZ III-nitrides [2]. The WZ structure for III-nitrides is one member of the hexagonal crystal system and comprises tetrahedrally coordinated group-III and nitrogen atoms. As the WZ structure has a hexagonal unit cell, there are two lattice constants, *a* in the basal plane and *c* in the perpendicular direction to the basal plane. The experimental lattice constants of binary III-nitrides and common substrates are summarized in Table 1 [3].

Table 1. Lattice constants, thermal expansion coefficients (TEC), and thermal conductivity of GaN and AlN and common substrates.

Material	*a* (Å)	*c* (Å)	TEC (*a*, 10^{-6}/K)	TEC (*c*, 10^{-6}/K)	Thermal Conductivity (W/cm-K)
Wurtzite GaN	3.189	5.185	5.59	3.17	1.3
Wurtzite AlN	3.112	4.982	4.20	5.30	2.0
6H-SiC	3.080	15.120	4.20	4.68	4.9
α-A_2O_3	4.758	12.990	7.50	8.50	0.5
Si	5.430	NA	3.59	NA	1.5

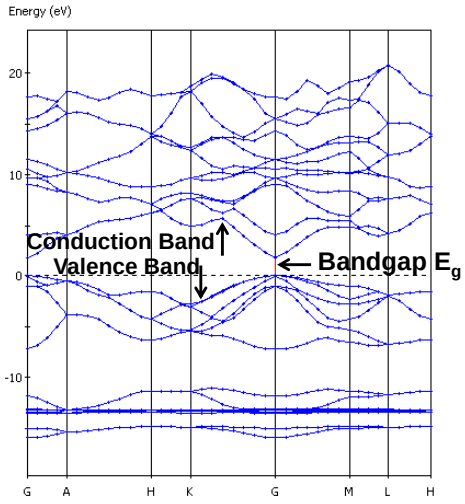

Figure 2. Band structure of wurtzite III-nitrides calculated by first principle methods showing a direct bandgap E_g at gamma point (k = 0).

The property of WZ III-nitrides that leads to most interest in their application in optical devices is the direct and variable bandgap at the gamma point of BZ between the bottom of conduction band and top of valence band, as shown in Figure 2. The direct bandgap allows an electron in the conduction band and a hole in the valence band to combine to emit a photon, in which the bandgap energy E_g determines wavelength λ of the photon according to the formula:

$$\lambda = \frac{h \cdot c}{E_g}, \tag{1.1.1}$$

where h and c are Planck constant and speed of light, respectively.

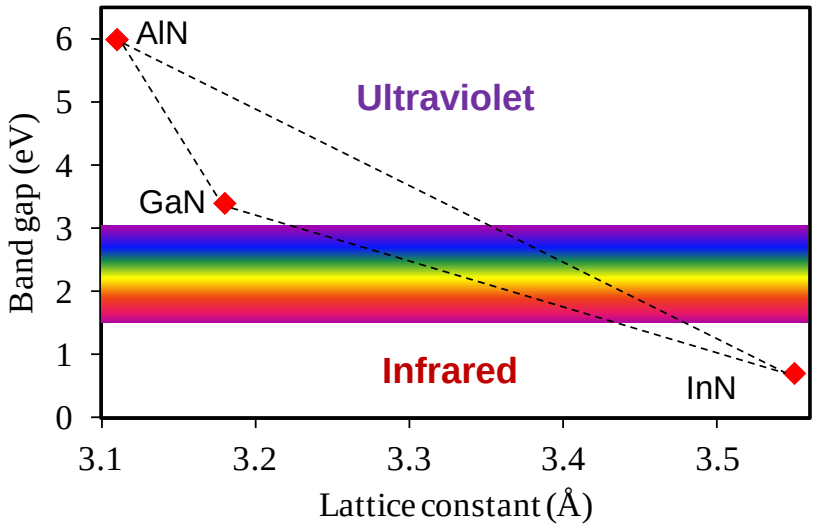

Figure 3. Bandgap energy of wurtzite III-nitrides as a function of material composition and in-plane lattice constant.

Because the binary wurtzite AlN, GaN and InN have bandgap energies of 6.2 eV, 3.4 eV, and 0.7 eV, the photon wavelengths of corresponding bandgap transition are 200 nm, 365 nm and 1771 nm, respectively, covering a wide range of spectrum from ultraviolet (UV) to infrared as shown in Figure 3. Moreover, the bandgap energy E_g of wurtzite III-nitrides can be engineered by changing material composition of ternary or quaternary alloys. Although it is still challenging to estimate bandgap energy E_g of the quaternary alloys $Al_xIn_yGa_{1-x-y}N$, the bandgap energy E_g of the ternary alloys $Al_xGa_{1-x}N$ or $In_xGa_{1-x}N$ can be estimated by the bandgap energy of binaries and formula based on Vegard's law:

$$E_{g,Al_xGa_{1-x}N}(x) = x \cdot E_{g,AlN} + (1-x) \cdot E_{g,GaN} + bx(1-x), \tag{1.1.2}$$

where b is the bowing parameter specific to each compound and determined experimentally. Similarly, the in-plane lattice constants a of the ternary alloys $Al_xGa_{1-x}N$ or $In_xGa_{1-x}N$ can be estimated by:

$$a_{Al_xGa_{1-x}N}(x) = x \cdot a_{AlN} + (1-x) \cdot a_{GaN} + bx(1-x). \tag{1.1.3}$$

1.2 Metalorganic chemical vapor deposition (MOCVD) process

MOCVD, also known as metalorganic vapor phase epitaxy (MOVPE) or organometallic vapor phase epitaxy (OMVPE) is a crystal deposition method invented by Manasevit in 1968 [4]. As compared to another common deposition method, molecular beam epitaxy (MBE) which grows the crystal by physical deposition in vacuum, MOCVD grows the crystal by chemical reaction in a non-vacuum environment. Because of its capability of growing high-quality crystal and reaching fast growth rate, MOCVD has been widely used to produce III-nitride materials and devices including laser diodes, solar cells, and LEDs.

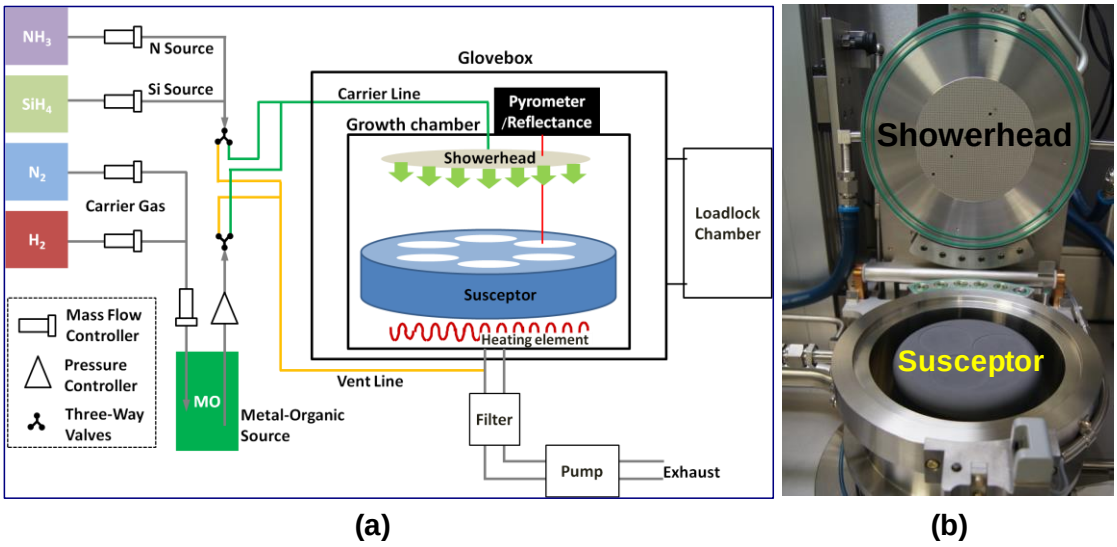

Figure 4. (a) Schematic diagram of a close-coupled showerhead MOCVD system and (b) a photo of the MOCVD growth chamber.

As shown in Figure 4(a), an AIXTRION SE 3×2" MOCVD system with a close coupled showerhead (CCS) has been used. The system mainly comprises a precursor storage system, a computerized gas circuit system, a growth chamber, and an exhaust system. During normal operation, the growth chamber shown in Figure 4(b) is isolated

from atmosphere by a N_2 glove box. The SiC-coated graphite susceptor and wafers are transferred from the atmosphere to the glove box through the loadlock chamber.

As the name suggests, MOCVD utilizes metalorganic (MO) materials with high purity to grow crystal. In my studies, there are seven MO bubblers connected to the MOCVD system. Each bubbler is kept in a Lauda RM6 water bath system such that the bubbler temperature is kept constant, which is critical to maintain the bubbler vapor pressure and thus the corresponding molar flow rate. The seven MO bubblers include two Trimethylgallium (TMG), two Trimethylaluminum (TMA), one Trimethylindium (TMI), one Triethylborane (TEB), and one Biscyclopentadienyl magnesium (Cp_2Mg) bubblers. The TMG, TMA, TMI and TEB bubblers provide group-III precursors. The Cp_2Mg bubbler provides Mg acceptors to dope the III-nitrides into p-type. The two TMG bubblers and two TMA bubblers are configured with different maximum flow rates to accommodate different ranges of different growth rates. As shown in Figure 4(a), ammonia (NH_3) is the nitrogen precursor and SiH_4 is used to n-dope the III-nitrides, both of which reside in independent gas cylinders stored in vented gas cabinets.

The chemical reaction between group-III precursors and NH_3 to form III-nitrides can be described as followed exemplarily by formation of binary III-nitrides:

$$Al(CH_3)_3(g) + NH_3(g) \rightarrow AlN(s) + 3CH_4(g), \quad (1.2.1)$$

$$Ga(CH_3)_3(g) + NH_3(g) \rightarrow GaN(s) + 3CH_4(g), \quad (1.2.2)$$

and

$$In(CH_3)_3(g) + NH_3(g) \rightarrow InN(s) + 3CH_4(g). \quad (1.2.3)$$

The formations of ternary and quaternary III-nitrides are similar. To grow the III-nitrides, the heated precursor molecules thermochemically decompose into respectively atoms in the absence of oxygen, or pyrolysis. The pyrolysis leaves the atoms diffusing on

the substrate surface. The atoms finally bond to the substrate which forms a new crystalline layer. Because of MOCVD is typically conducted at relatively high temperatures, it is a mass transport limited rather than reaction rate limited process. Thus the deposition rate is mainly determined by molar flow rates of precursors. In addition, the mobility of atoms depends on surface temperature of substrate as well as chamber pressure.

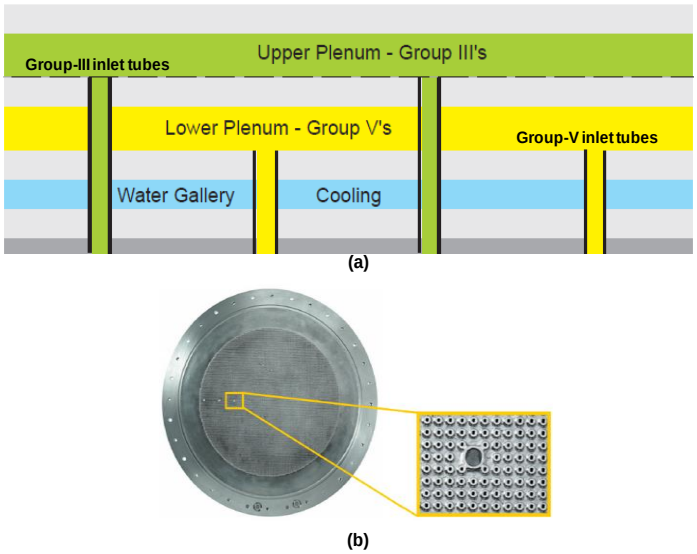

Figure 5. (a) Cross-sectional schematics of showerhead, and (b) showerhead with detailed view showing dense and small inlet tubes.

During the growth, the group-III precursor mixes with non-volatile carrier gas N_2 and/or H_2 in the bubbler. Then the mixture gas flows into the upper plenum locating in the showerhead. From the upper plenum, the mixture gas flows into the growth chamber via group-III inlet tubes, as shown in Figure 5(a)-(c) [5]. The density of tubes is 100 tubes/inch^2 with a tube inner diameter of 0.6 mm. On the other hand, Cp_2Mg, NH_3, SiH_4, and carrier gas flow into the lower plenum and then get into the chamber via group-V inlet tubes. The intermixing of precursors within close proximity to the substrates configured in the showerhead, also known as closed-coupled showerhead (CCS) results in that the decomposed atoms diffuse very quickly through the gas phase onto the wafer surface and

thereby lead to uniform deposition. The use of CCS avoids the necessity of high speed susceptor rotation speed of over 500 rpm in the vertical MOCVD system. For instance, a rotation speed as low as 10 rpm can also lead to high uniformity in this MOCVD system. As the precursors and gaseous reaction byproducts leave the susceptor edge, they are exhausted out from the bottom of growth chamber and pass through a filter outside the growth chamber by an Ebara pump and move into a scrubber.

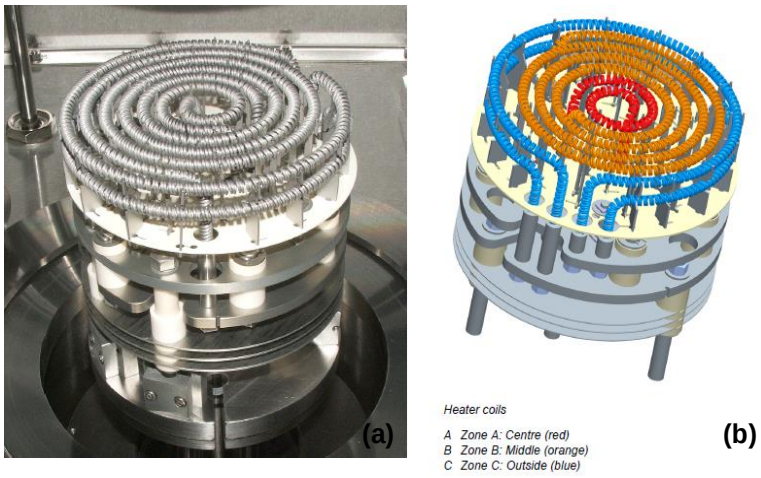

Figure 6. (a) Photo and (b) schematics of the three-zone heater.

In addition, a three-zone heater consisting of three sets of coils made of unencapsulated Tungsten rhenium allows for control of temperature gradients within the chamber to further control uniformity, as show in Figure 6(a)-(b) [5]. Each zone corresponds to one set of coil supplied by one independent power supply. The power supplies are configured such that the surface temperature of substrates on the susceptors can reach up to 1300 ^{o}C.

As mentioned above, it is important to maintain MO bubbler temperatures $T_{bubbler}$ (^{o}C) to achieve consistent molar flow rates (μmol/min), because the partial vapor pressure P_{MO} (mbar) of MO precursor is determined according to the formula:

$$P_{MO}(mbar) = 10^{a-\frac{b}{T_{bubbler}+27415}} \cdot 1.33, \tag{1.2.4}$$

where a and b are coefficients uniquely specific for each MO precursor. The number of 1.33 is used to convert the pressure unit from Torr to mbar. The number of 274.15 is used to convert the bubbler temperature from Celsius to Kelvin. In addition, the molar flow rate F_{molar} is related to the vapor pressure based on the formula:

$$F_{molar} = \frac{P_{MO}}{R \cdot T} \cdot \frac{F_{vol}}{P_{total}}, \tag{1.2.5}$$

where R and T are the ideal gas constant and MO line temperature which can be assumed to be room temperature of 300 K. F_{vol} is the volume flow rate (sccm) of the MO precursor and P_{total} is the total pressure of bubbler. To further calculate the molar flow rate F_{molar}, the ideal gas equation is used:

$$P_{MO}V = nRT. \tag{1.2.6}$$

Since one mol of MO precursor gas has a volume of 22.4×10^3 cm^3, Equation (1.6) can be written as:

$$RT = P_{MO} \cdot 22.4\times10^3 cm^3 \cdot \frac{1}{1mol}. \tag{1.2.7}$$

Thus Equation (1.2.5) becomes:

$$F_{molar} = \frac{1mol}{22.4\times10^3 cm^3} \cdot \frac{P_{MO}}{P_{total}} \cdot F_{vol}. \tag{1.2.8}$$

Table 2. Molar flow rates of the group-III MO precursors.

MO source	a	b, K	Bubbler temperature °C	Partial vapor pressure mbar	Total pressure mbar	MO volume flow rate sccm	Molar flow rate μmol/min
TMG_1	8.07	1703	20	253.68	1900	200	1192
TMG_2	8.07	1703	17	221.12	1300	100	759
TMA_1	8.22	2134	17	10.33	1300	100	35
TMA_1	8.22	2134	18.7	11.40	1300	100	39
TMA_2	8.22	2134	17	10.33	1300	500	177
TMI	10.52	3014	0	0.45	2000	500	5
TEB	7.41	1544	1	83.63	1300	100	287

Table 2 summarizes the maximum molar flow rates of the MO precursors based on the maximum MO volume flow rate of each bubbler for the current MOCVD system. Take the TMA_1 bubbler as an example as shown in the shaded cells, a bubbler temperature variation of 10% from 17 C to 18.7 C leads to about 10% change in the molar flow rate from 35.46 to 39.11 μmol/min due to the increased partial vapor pressure. Thus the bubbler temperature has to be stable for consistent growth rates. To vary the molar flow rate, the volume flow rate (1st choice), total pressure (2nd choice), and bubbler temperature (3rd choice) can be changed. The volume flow rates of precursors are controlled by computerized gas circuit system consisting of mass flow controller, pressure controller, and manual or automatic switching valves.

2 III-NITRIDE ULTRAVIOLET LASER

2.1 Introduction to laser

The term "laser" was firstly used as an acronym for "light amplification by stimulated emission of radiation". What differs laser from the other light sources is that it emits coherent light. Being coherent includes both spatial coherence and temporal coherence. The spatial coherence enables a narrow and thus high energy density laser beam over a great distance. The temporal coherence allows for a very narrow spectrum, leading to monochromatic or short-pulsed laser. These unique properties result in a wide range of applications including optical pumping, optical data storage, lighting, weapon, biochemical detection, barcode scanners, communication, surgery, welding, and etc.

Structurally a laser comprises an optical cavity or resonator which consists of a pair of mirrors on either end of a gain media. With exception of extremely high gain lasers such as the nitrogen laser, it is common for a commercial laser wherein one mirror is a high reflector with a reflectivity close to 100%, while the other mirror is a partially reflective output coupler that allows a portion of the laser beam to extract from the optical cavity. The gain medium is the place where stimulated emission happens and is amplified. Depending on the gain medium, types of the lasers can include semiconductor, fiber, gas, solid-state, dye, free-electron and photonic crystal lasers.

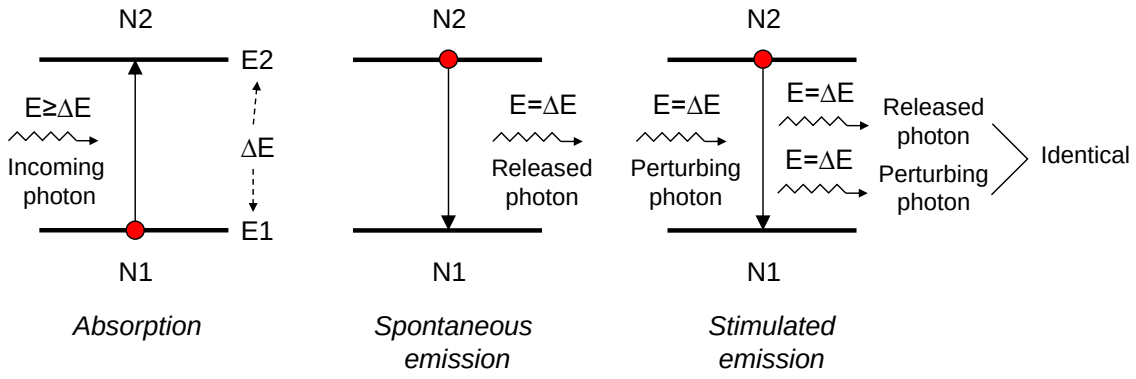

Figure 7. Schematics of processes of (a) absorption, (b) spontaneous emission, and (c) stimulated emission processes.

The stimulated emission can be understood by examining Figure 7. According to quantum mechanics, energy levels of electrons of atoms within the gain medium are discrete. When applying or 'pumping' energy to the gain medium, atoms get 'excited' by absorbing the energy. As a result, electrons of the atoms move from a 'ground' energy level E1 to an 'excited' energy level E2. After a period of time, the excited electrons relaxes to the ground energy level. In this process, photons may be released whose energy equals to the difference between the excited and ground energy levels ΔE. Without external perturbation, the phase and direction of the photons emitted by the electron relaxation of different atoms would be random. This process is called spontaneous emission where the light is not coherent.

However, if the electron at the excited energy level relaxes to the ground energy level under the perturbation of an incoming photon with energy equal to the energy level difference and an external electromagnetic field at a frequency, a second photon may be released without absorbing the incoming photon. This second photon has the same frequency, phase and direction as the incoming photon. The incoming photon may be formed within the gain medium by the spontaneous emission process. Therefore coherent

light is formed. This process of generating a photon with the same properties under the perturbation of an incoming photon is called stimulated emission. In the case of semiconductor laser, the excited and ground energy levels represent conduction and valence bands.

The requirement of lasing is very demanding. Observation of natural lasing on the earth has not been reported yet. This is because two limitations can easily prevent lasing or amplification of stimulated emission:

a) At a low pumping level, a majority of atoms in the gain medium are not excited. This leaves more electrons on the ground level than the excited level. Thus before an incoming photon stimulates an excited electron, it is likely that this photon gets absorbed and thus lasing is not possible. Therefore a high pumping level is needed to create the 'population inversion' where the excited electrons outnumber the ground-state electrons.

The population inversion can be modelled mathematically by considering Fermi-Dirac distribution of electrons and holes in non-equilibrium. Assuming a plurality of photons move within the gain medium with a density of N_{photon} and individual photon energy equal to or larger than the difference between the ground and excited levels, the absorption and thus stimulated emission may happen.

For absorption, the number of electrons moving to the exited level should be proportional to the number of electrons on the ground level and equal to the number of electrons the ground level loses. Therefore the absorption rate is:

$$\frac{\partial N_2}{\partial t} = -\frac{\partial N_1}{\partial t} = -B_{12} N_{photon} N_1, \tag{2.1.1}$$

where B_{12} is a proportionality constant associated with the absorption known as Einstein *B* coefficient.

For stimulated emission, the number of electrons relaxing to the ground level should be proportional to the number of electrons on the excited level and equal to the number of electrons the excited level loses. Therefore the stimulated emission rate is:

$$\frac{\partial N_1}{\partial t} = -\frac{\partial N_2}{\partial t} = -B_{21} N_{photon} N_2, \tag{2.1.2}$$

where B_{21} is a proportionality constant associated with the stimulated emission. Einstein has shown that the two coefficients must be the same, i.e.:

$$B_{12} = B_{21} = B. \tag{2.1.3}$$

Therefore, the net stimulated emission rate is:

$$\frac{\partial N_2}{\partial t} - \frac{\partial N_1}{\partial t} = B N_{photon}(N_2 - N_1). \tag{2.1.4}$$

To ensure the net simulated emission rate is positive, there must be more electrons in the excited than ground level, i. e. population inversion:

$$N_2 > N_1.$$

b) After stimulated emission happens, the light bounces back and forth within the gain medium because of the mirrors. It is important to maintain and amplify intensity of stimulated emission during this process. However, scattering and re-absorption in the gain medium as well as leakage through the mirrors and non-gain-medium regions lead to losses that weaken the intensity. Therefore materials and structures of gain medium and mirrors must be selected correctly to ensure a net positive gain to amplify the stimulated emission. Under a net positive gain and population inversion, the stimulated emission is amplified and a laser beam is formed.

2.2 Ultraviolet laser

Ultraviolet (UV) light has wavelengths shorter than 400 nm. Conventionally, UV light include UV-A (320-400 nm), UV-B (290-320 nm), UV-C or deep-UV (DUV) (100-290 nm), and extreme-UV (10-100 nm) spectral ranges.

UV light has numerous applications compared with visible light. UV light has shorter wavelengths. This allows more precise focusing and engineering of finer structures, as exemplified by its application in fabrication of sub-micrometer features in semiconductor chips. Photons of UV light have higher energies than bandgap energies of many materials. As a result, UV light can be strongly absorbed by many materials, which leads to changes of material structures. This property has been applied for laser processing, lighting, spectroscopy and disinfection. In addition, natural DUV light has little presence on the earth surface because of strong absorption by ozone in the atmosphere. This leads to a nearly noiseless environment for an extremely sensitive UV communication receiver such as a photon-counting device like a photomultiplier tube (PMT). This advantage, together with strong scattering of DUV light in the atmosphere, provides potential for forming non-line-of-sight (NLOS) optical communication links.

UV light can be generated by a variety of light sources. The most common source of incoherent UV light is the gas-discharge lamp. Common gases used in the lamps include mercury, excimer, and Argon. Coherent UV light is typically generated by gas and solid-state lasers as well as frequency conversion of longer-wavelength lasers.

2.3 III-nitride deep ultraviolet laser diode

Comparing with the conventional UV light sources mentioned above, III-nitride semiconductor light-emitting diodes (LEDs) and laser diodes (LDs) are potentially

compact, more reliable, more efficient and have a longer lifetime. Not only can these superior properties improve performance of current applications greatly, but also they can stimulate novel applications that were not possible before. Therefore UV LEDs and LDs have attracted numerous attention in the research and industrial communities. Although DUV LEDs have been realized and electrically-pumped UV nanowire random lasers have been demonstrated at 262-340 nm [6,7], the shortest wavelength of UV quantum-well (QW) LDs is limited at ~340 nm [8]. This prohibits applications of LDs in the DUV range. This dissertation focuses on realization of DUV LDs. Two types of DUV LDs are of most interest in this dissertation.

a) Edge-emitting DUV LD

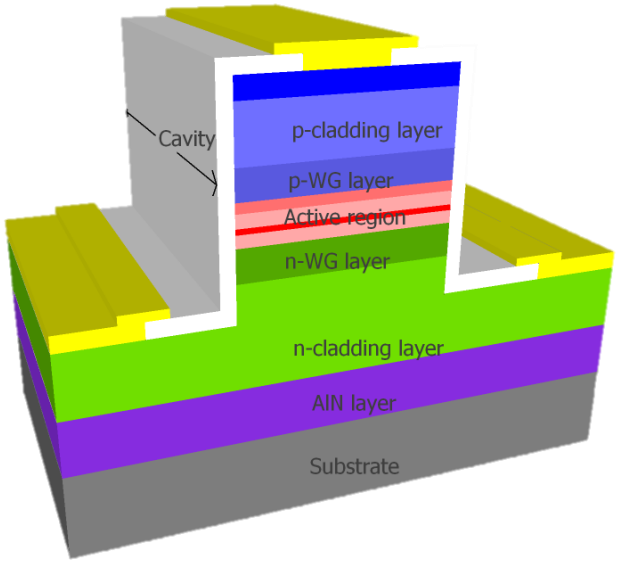

Figure 8. A schematic structure of an edge-emitting DUV LD.

Figure 8 shows a simplified structure of an edge-emitting DUV LD. The structure starts with growth of an AlN layer serving as a 'template' layer on suitable substrates such as AlN, SiC and sapphire. Then n-type cladding and waveguide (WG) layers are deposited on the AlN layer. Afterwards, an active region comprising a plurality of quantum wells and barriers are grown, followed by growth of an electron-blocking layer (EBL). The growth

is concluded by WG and p-type cladding layers and a thin but heavily doped p-type contact layer. Subsequent to the growth, microfabrication tools are used for mesa etching, deposition of metal contacts, cleaving and facet coating. The two WG layers aim to confine optical modes at the active region, which is the gain medium, to obtain a net positive gain. The LD is pumped electrically. At a low pumping level, DUV light is generated via spontaneous emission and bounces back and forth by the mirrors. Once the pumping is beyond laser threshold, population inversion is achieved and thus the LD starts to lase horizontally through the front mirror.

b) Vertical-cavity surface-emitting lasers (VCSELs) LD

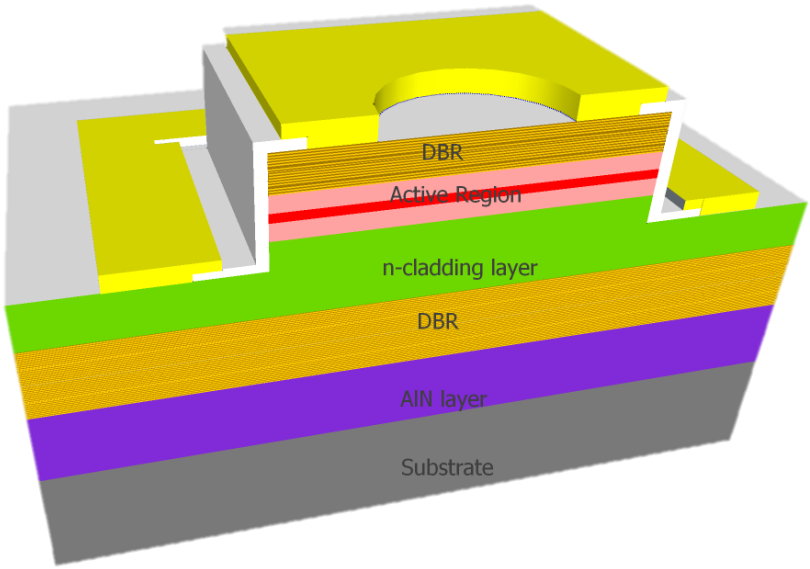

Figure 9. A schematic structure of a VCSEL LD

The VCSEL is similar to the edge-emitting LD in many ways. It also includes a p-i-n heterostructure where the active region is responsible for emitting the light. The biggest difference between the edge-emitting LD and VCSEL LD is that the VCSEL LD has a monolithic cavity sandwiched by one pair of distributed Bragg reflectors (DBRs), as shown in Figure 9. The cavity is perpendicular to the device surface instead of being parallel for the edge-emitting LD. Because of this unique configuration, there are a few benefits of

VCSEL over the edge-emitting LD. For example, the VCSEL can be tested after growth without cleaving the wafer as for the edge-emitting LD. Therefore it can greatly reduce time and cost of identifying problems and improving manufacturing yield. Another beneficial feature is that VCSEL does not have cleaved facets. The lack of such facets avoids possible optical damage by high-energy laser beams because the emitting facet scales with device power preventing overshooting of optical power density, which improves device lifetime.

2.4 Scope of dissertation

In general, it is extremely challenging to realize the DUV LDs because a few major issues are present. First, high-Al III-nitrides grown heteroepitaxially on inexpensive foreign substrates such as sapphire still possess a high density of dislocations. The dislocations act as non-radiative recombination centers that reduce quantum efficiency and increase lasing threshold, which prevents lasing from even optical pumping experiments. AlN substrates may be used to alleviate this issue, but the high cost and strong DUV absorption hinder practical production. Second, it is very difficult to achieve good p-type doping in high-Al III-nitrides to inject enough holes in the active region, because these materials have a high activation energy for mostly used p-type dopants Mg acceptor. For III-nitride VCSEL LDs, although they have been realized in the visible spectrum by employing dielectric stacks for one or both DBRs [9,10], it is preferred that both DBRs be consisted of in-situ grown III-nitrides to reduce complexity and time of device fabrication.

The works leading to this dissertation have aimed to address some of the challenging issues above. First, high temperature growth was to grow AlGaN heterostructures on sapphire and AlN substrates, which led to low-threshold DUV lasing

on AlN and DUV surface superluminescence on sapphire substrates, respectively (Chapters 4 & 5). Second, material quality of high-Al III-nitrides needs to be improved greatly on sapphire substrates under practical conditions (Chapters 4 & 5). Third, optically-pumped DUV lasers on sapphire would be demonstrated because of improved material quality and deliberate design of the laser structure, and optical polarization characteristics of lasing will also be studied (Chapters 6 & 7). Last but not least, growth of novel BAlN materials would be investigated to provide suitable index contrast with high-Al III-nitrides to form DBRs (Chapter 8).

3 LOW-THRESHOLD DEEP-UV LASING FROM ALGAN HETEROSTRUCTURES GROWN ON ALN SUBSTRATES

3.1 Introduction

Deep-ultraviolet (DUV) emitters with wavelengths shorter than 280 nm have numerous applications such as optical storage, disinfection and biochemical identification. However, most of the commercially available DUV emitters including mercury lamps, quadrupled Nd:YAG lasers and excimer lasers have limitations in many applications due to their large footprint, poor reliability and/or toxicity. Recently, III-nitride semiconductor light emitters have drawn great attention, as the direct bandgap covers the entire DUV range which can lead to efficient, compact and reliable DUV emitters. The quality of III-nitride material, especially for $Al_xGa_{1-x}N$ ($x > 0.50$) materials with bandgap from 4.4 to 6.0 eV, is the key to high performance DUV emitters. Because of large lattice mismatch, the growth of high-Al AlGaN and AlN layers on commercially viable sapphire substrates lead to high dislocation density and thus low quantum efficiency.

Recently, low-threshold optically-pumped DUV lasers comprising AlGaN multiple quantum wells (MQWs) grown on bulk AlN substrates have been demonstrated [11-13]. The bulk AlN substrates were employed in these studies to minimize the lattice mismatch and thermal expansion between the substrate and epitaxial layer, thus leading to low dislocation density.

Growths at temperatures higher than 1200ºC were shown to improve material quality of AlN on foreign substrates significantly in the metalorganic chemical vapour deposition (MOCVD) process due to the enhancement of surface mobility of Al atoms [14].

However, there is a lack of studies on growth of AlGaN heterostructures at high temperature for DUV lasers.

In this study, we present growth of the AlGaN heterostructure on (0001) a bulk AlN substrate ("wafer") grown at a high temperature of 1250 ^{o}C. Atomic force microscopy (AFM), X-ray diffraction (XRD) and power-dependent photoluminescence (PL) measurements were carried to investigate the material quality and MQW structure. After the growth, the wafer was fabricated into a Fabry-Perot laser cavity. Lasing at 266.0 nm with threshold of 124 kW/cm^2 on the laser cavity were demonstrated in an edge-emission configuration.

3.2 Experiment

The AlGaN heterostructure was epitaxially grown in an AIXTRON 3×2" MOCVD reactor with a close-coupled showerhead. The diameter of bulk AlN substrates is 1 cm. Prior to the growth, the native oxide layer on the surface of AlN substrate was removed by an etching process in a 3:1 H_2SO_4:H_3PO_4 solution at 90 ^{o}C to remove the native surface oxide. The epitaxial structure grown in this study were optimized for optical pumping experiments in pursuit of low-threshold optically pumped lasers, which is a critical step stone for the development of an electrically-driven diode laser.

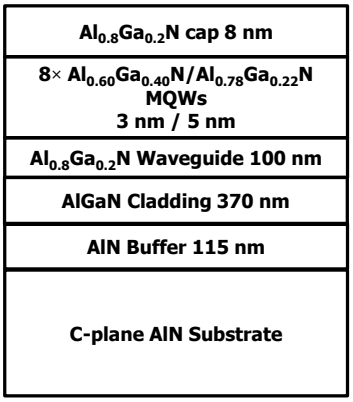

Figure 10. Cross-sectional schematics of the AlGaN heterostructure grown on the bulk AlN substrate.

The cross-sectional view of the layer structure grown on the AlN substrates is shown in Figure 10. A 115-nm high temperature AlN buffer layer was grown at 1300°C on the AlN substrate, followed by AlGaN cladding and $Al_{0.8}Ga_{0.2}N$ waveguide layers grown at 1250 °C. An active region comprising eight periods of 2-nm $Al_{0.60}Ga_{0.40}N$ quantum wells and 5-nm $Al_{0.78}Ga_{0.22}N$ quantum barriers was grown directly on the waveguide layer at 1250°C. To further enhance the Al-atom mobility, low V/III ratios were individually optimized for the high-temperature AlN buffer layer (~20) and AlGaN MQW structure (50-100), which was found to promote two-dimensional growth and smooth surface formation.

To obtain high-quality AlGaN MQWs, both active regions on the sapphire and AlN substrate were grown using intentional interruption between switching the growth conditions of QW and QB. As the NH_3 flow rate was different between growing the QW and QB due to different V/III ratios, it was found that the NH_3 ramping time between the growths of QW and QB is influential on the luminescence characteristics. The zero or shorter ramping time can lead to a transient in the NH_3 flow rate, which resulted in uncontrollable inhomogeneity of material compositions and thus large full-width-at-half-maximum (FWHM) of the emission spectrum. On the other hand, longer ramping times caused a larger surface roughness due to the AlGaN decomposition at the high growth temperature. In addition, we have found that the deposition/decomposition rates of the given compositions of AlGaN material is very sensitive to the temperature around 1250°C. Thus the emission wavelength shift can occur with an unstable growth temperature. Eventually, a ramping time of 2.5 s from well to barrier and barrier to well growth was found to be optimal. The whole structure on the AlN substrate is finished with a thin cap layer of $Al_{0.78}Ga_{0.22}N$ for surface passivation. It is noted that an increased thickness of cap

layer could increase the transverse optical confinement of the entire active region. However, a thicker cap layer leads to higher absorption loss of excitation power of in-house 193-nm excimer laser, limiting the cap layer to be thin.

3.3 Result and discussion

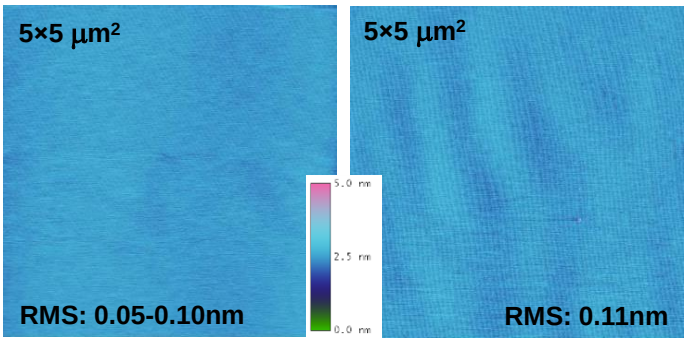

Figure 11. The 5×5 μm^2 atomic force microscopy image of the (a) AlGaN heterostructures grown on the AlN substrate and (b) the AlN substrate before growth.

As shown in Figure 11(a), the room-mean-square (RMS) roughness of wafer is 0.11 nm, respectively. Terraced step flow is preserved on the wafer, which is a characteristic of two-dimensional epitaxial growth. Considering that prior to growth, the AlN substrate possessed an RMS roughness of 0.05-0.10 nm (Figure 11(b)), the growth of the MQW structures indicates a slight surface roughening while maintaining a low defect density thanks to the higher atom mobility at high temperature.

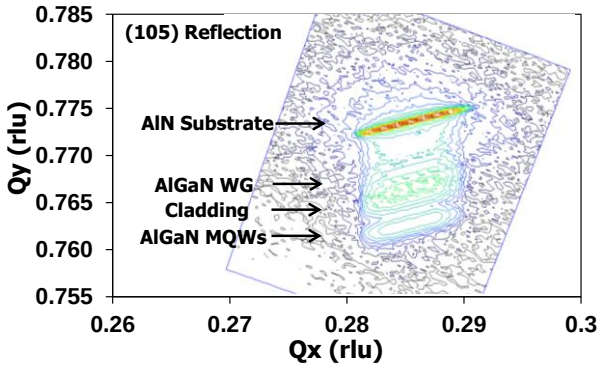

Figure 12. XRD RSM of the epitaxial structure on the AlN substrate demonstrating pseudomorphic growth.

Asymmetric (105) reciprocal space mapping (RSM) of the wafer by high-resolution triple-axis XRD was conducted. As shown in Figure 12, the entire structure in Figure 10 is pseudomorphically deposited on the AlN substrate. To study the lasing characteristics of the wafer, the wafer was thinned to 80 μm by lapping the AlN substrate and a laser bar was formed using cleaved *m*-plane facets with a 1.05-mm long resonant Fabry-Perot cavity. The laser bar was optically pumped by the 193-nm excimer laser in the edge-emission configuration at RT where the detailed experimental setup can be found in Chapter 7.

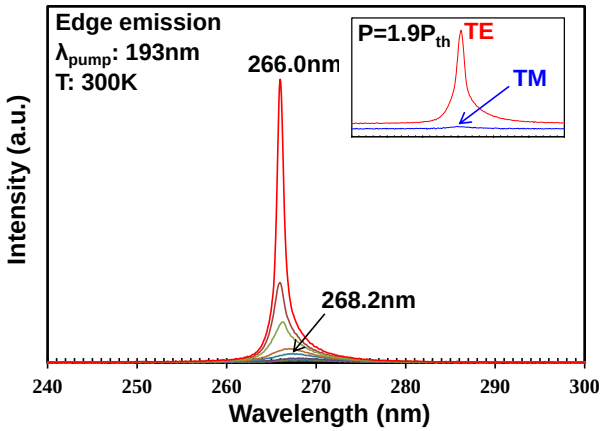

Figure 13. Laser emission spectra of AlGaN MQW on the AlN substrate with pump power densities below and above threshold at room-temperature. The inset shows TE and TM-modes emission spectra for the same laser bar operating above threshold at room-temperature.

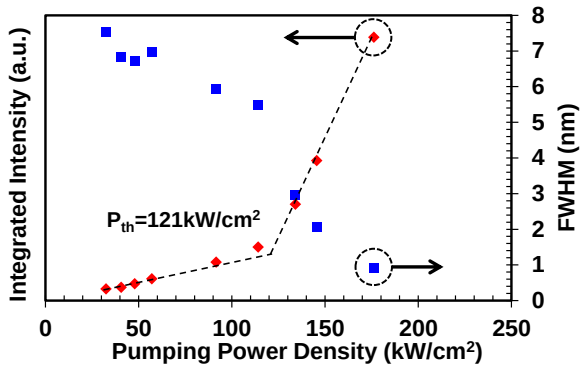

Figure 14. Integrated spectral intensity and FWHM of the laser emission spectra of AlGaN MQW on the AlN substrate as a function of the optical pump power density at room-temperature.

Laser emission spectra with different pumping power densities are shown in Figure 13. The peak wavelength of spontaneous emission was 268.2 nm with FWHM of 7.52 nm at the minimum measured pumping power density of 35 kW/cm^2, while the peak wavelength of laser emission was 266.0 nm with FWHM reducing to 0.91 nm at the maximum measured pumping power density of 192 kW/cm^2. The laser emission band is located on the high-energy slope of the spontaneous emission spectrum. Localized states and screening of the built-in electric field have been attributed to the blue shift of the laser emission band [15]. As shown in Figure 14, the pumping power density dependent spectral integrated intensity demonstrates a distinct lasing threshold at the pumping power density of 124 kW/cm^2. Beyond the threshold the laser emission output increases linearly with the pumping power density. The threshold is similar to the threshold of 126 kW/cm^2 at peak wavelength of 267 nm reported in the recent study, which utilized slightly different approach to estimate the lasing threshold [11]. The threshold could be further reduced by growing a thicker cap layer to increase the optical confinement within the active region and/or using excitation source with longer wavelength to reduce absorption in the non-QW layer.

In addition, the polarization of laser emission was determined at pumping power density 1.9 times higher than the threshold. As shown in the inset of Figure 13, the laser emission is transverse-electric (TE) (perpendicular to *c*-axis) dominant with the degree of polarization, defined as $(I_{TE} - I_{TM})/(I_{TE} + I_{TM})$ equals 0.91, which is desired for edge-emitting lasers due to less penetration of beam profile into lossy regions vertically as compared to transverse magnetic (TM) polarization (parallel to *c*-axis). This observation is consistent with the previous experimental and theoretical studies and suggests dominance

of topmost valence band transition based on heavy holes (TE polarization) over split-off holes (TM polarization) with the given or similar growth conditions in the reported wavelength range [11,13,16].

3.4 Conclusion

In summary, the AlGaN heterostructure has been grown on an AlN substrate at a high temperature of 1250 ^{o}C. Lasing at 266.0 nm was demonstrated with a low threshold of 124 kW/cm^2 from AlGaN MQWs on the AlN substrate at RT. The threshold can be further reduced by employing thicker cap layer and/or excitation source with longer wavelength. These results demonstrate viability of AlN substrates and high temperature growth for high-quality active region for future development of DUV laser diodes.

4 DEEP-UV SURFACE SUPERLIMINESCENCE FROM ALGAN HETEROSTRUCTURES GROWN ON SAPPHIRE SUBSTRATE

4.1 Introduction

As stated in the last chapter, low-threshold optically-pumped DUV lasers comprising AlGaN MQWs grown on bulk AlN substrates have been demonstrated [11-13]. The bulk AlN substrates were employed in these studies to minimize the lattice mismatch and thermal expansion between the substrate and epitaxial layer, thus leading to low dislocation density. But due to the low availability, smaller area and high cost of bulk AlN substrates, it is desirable to grow DUV lasers on vastly more available and low-cost foreign substrates like sapphire substrates. However, due to the high dislocation density within the heteroepitaxial $Al_xGa_{1-x}N$ layers grown on sapphire substrates, stimulated or superluminescent emission below 280 nm at room temperature (RT) remains difficult to achieve [15,17].

In this study, we present growth details of AlGaN heterostructure on the (0001) sapphire substrate ("wafer") grown at a high temperature of 1250 ^{o}C. The use of high temperature aimed to improve material quality of high-Al AlGaN in the MOCVD process due to the enhancement of surface mobility of Al atoms [18]. Atomic force microscopy (AFM), scanning transmission electron microscopy (STEM), and power-dependent photoluminescence (PL) measurements were carried to investigate the material quality and MQW structure. Superluminescence at 259.7 nm on the wafer was demonstrated in a surface-emission configuration, respectively.

4.2 Experiment

The AlGaN heterostructure was epitaxially grown in an AIXTRON 3×2" MOCVD reactor with a close-coupled showerhead. The diameter of sapphire substrate is 2 inch. The epitaxial structures grown in this study were optimized for optical pumping experiments in pursuit of low-threshold optically pumped lasers, which is a critical step stone for the development of an electrically-driven diode laser.

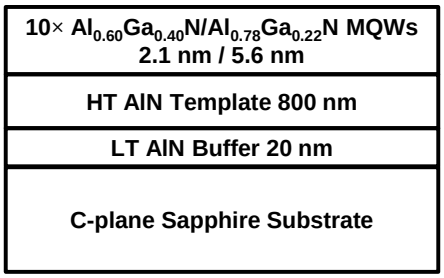

Figure 15. Cross-sectional schematics of the AlGaN heterostructure grown on the sapphire substrate.

Cross-sectional view of the layer structure grown on the sapphire substrate is shown in Figure 15. Referring to the layer structure on sapphire substrate as shown in Figure 15, before the AlGaN MQW structure was deposited on the sapphire substrate, a 20-nm thick low-temperature AlN buffer layer was grown at 960 ^{o}C followed by an 800-nm high-temperature AlN template layer grown at 1300 ^{o}C. (002) and (102) FWHMs of X-ray diffraction (XRD) ω-scan of the template layer are 580 and 1400 arcsec, respectively. Thus the dislocation density is estimated to be low 10^{10} cm^{-2}. The MQW structure comprises ten periods of 2.1-nm $Al_{0.60}Ga_{0.40}N$ quantum wells and 5.6-nm $Al_{0.78}Ga_{0.22}N$ quantum barriers grown at 1250 ^{o}C. To further enhance the Al-atom mobility, low V/III ratios were individually optimized for the high-temperature AlN template layer (~30) and AlGaN MQW structure (50-100), which was found to promote two-dimensional growth and smooth surface formation.

To obtain high-quality AlGaN MQWs, the MQW structure was grown using intentional interruption between switching the growth conditions of QW and QB. As the NH_3 flow rate was different between growing the QW and QB due to different V/III ratios, it was found that the NH_3 ramping time between the growths of QW and QB is influential on the luminescence characteristics. The zero or shorter ramping time can lead to a transient in the NH_3 flow rate, which resulted in uncontrollable inhomogeneity of material compositions and thus large full-width-at-half-maximum (FWHM) of the emission spectrum. On the other hand, longer ramping times caused a larger surface roughness due to the AlGaN decomposition at the high growth temperature. In addition, we have found that the deposition/decomposition rates of the given compositions of AlGaN material is very sensitive to the temperature around 1250 ^oC. Thus the layer thickness and emission wavelength shift can occur with an unstable growth temperature. Eventually, a ramping time of 2.5 s from well to barrier and barrier to well growth was found to be optimal, which is similar to the observation in the last chapter.

4.3 Result and discussion

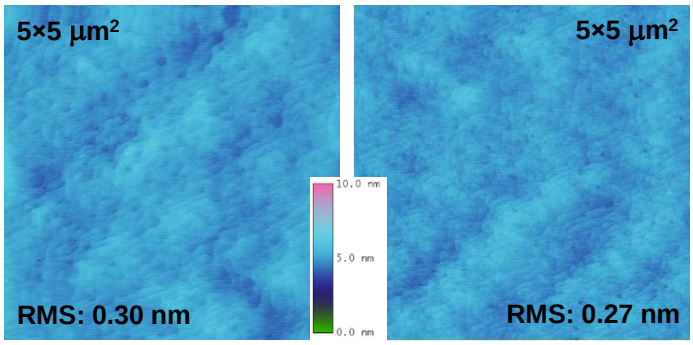

Figure 16. 5×5 μm^2 AFM images of the AlGaN heterostructure grown on the a) sapphire substrate and b) AlN template layer prior to the growth of AlGaN heterostructure.

As shown in Figure 16(a), the room-mean-square (RMS) roughness of wafer is 0.30 nm. Considering that prior to growth, the AlN template layer possessed RMS roughness of

0.27 nm, the growth of the MQW structures indicates a slight surface roughening attributed to the higher atom mobility at high temperature.

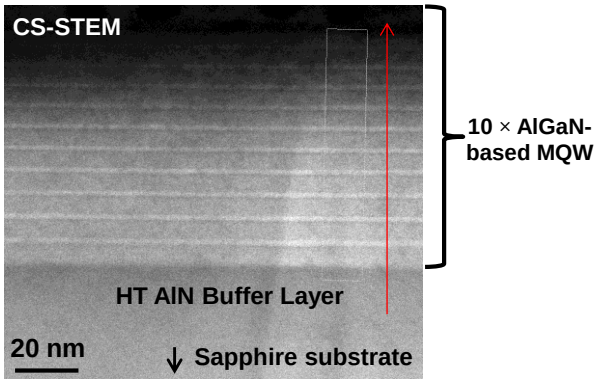

Figure 17. The cross-sectional STEM image of the AlGaN MQW structure grown on the sapphire substrate.

Cross-sectional STEM analysis was conducted on the active region of the wafer with zone axis <11-20> and **g** = 0, as shown in Figure 17. Sharp and smooth QW/QB interfaces have been observed and all the ten periods of MQWs are present, indicating excellent material and structural quality of the active region.

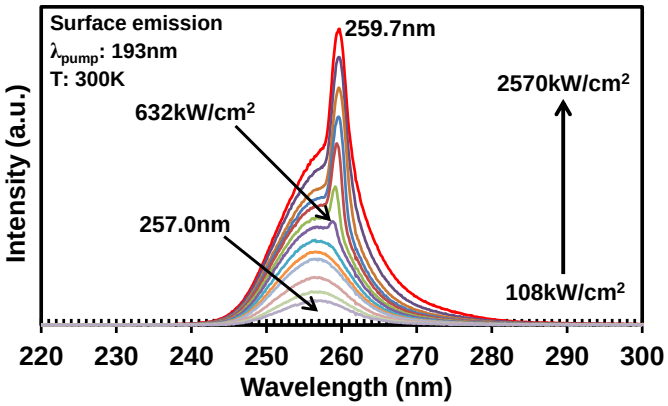

Figure 18. Superluminescence and spontaneous emission spectra of the AlGaN MQW grown on the sapphire substrate as a function of the optical pumping power density at RT.

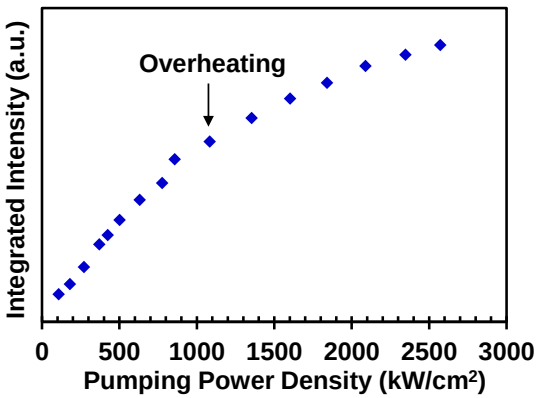

Figure 19. Integrated spectral intensity (linear scale) of superluminescence and spontaneous emission of the AlGaN MQW grown on the sapphire substrate as a function of the optical pumping power density at RT.

Following the growths, photoluminescence measurements were carried to characterize the wafer by a 193-nm ArF excimer laser in the surface-emission configuration at RT. The technical details of optical pumping system is presented in Chapter 7. The pumping power density was increased from 108 to 2570 kW/cm^2. As shown in Figure 18, a spontaneous emission spectrum with a peak wavelength at 257 nm is overlapped with a superluminescence emission spectrum with a peak wavelength at 259.7 nm. The superluminescence becomes observable at a pumping density of 501 kW/cm^2. The linewidth of the superluminescence emission is 2 nm at power density of 2570 kW/cm^2, while the FWHM of the spontaneous emission is 10.6 nm at power density of 108 kW/cm^2. It is noted that the spontaneous emission and superluminescence are not from a fabricated laser cavity. Rather, it is obtained by optically pumping the 2-inch wafer vertically. The emission is collected by an optical fiber at about 60 degrees and 30 degrees with respect to the wafer surface and laser beam, respectively. Due to the lack of a laser cavity and thus coherent light emission, there is no abrupt increase in the light output vs. pump intensity (L_{out}–L_{in} curve) as shown in Figure 19. It is important to note that the sapphire substrate had significantly lower thermal conductivity of ~ 35 W/(m·K) than ~ 285 W/(m·K) of the

AlN layer. Thus overheating could occur beyond certain critical excitation power density. The overheating reduced internal quantum efficiency (IQE) of the active region that made the L_{out}–L_{in} curve roll over at higher pumping densities due to the minimal in heat dissipation for the MQW grown on the sapphire substrate. Previously, the overheating was observed in the DUV MQW lasers grown on the AlN substrates photo-pumped at excitation power density over 3 MW/cm^2 at RT [12]. In this study, we observed that the overheating could happen around 1100 kW/cm^2. To our knowledge, this represents the superluminescence with the shortest wavelength from AlGaN MQWs grown on sapphire substrates reported to date. Since superluminescence is the spontaneous emission amplified by stimulated emission in the gain medium, this study demonstrates the excellent candidacy of AlGaN MQWs grown at higher temperature for lasing in DUV. Further efforts are being carried to achieve surface lasing in the vicinity of this wavelength on sapphire substrate.

4.4 Conclusion

In summary, the AlGaN heterostructure has been grown on the sapphire substrate at 1250 ^{o}C. The details of growth have been discussed. Superluminescence at 259.7 nm was achieved at RT from optically-pumped AlGaN MQWs on the sapphire substrate, representing superluminescence with the shortest wavelength from AlGaN MQWs on sapphire substrates reported to date. The MQW active region was found to possess high structural quality. These results demonstrate viability of sapphire substrates and high temperature growth for high-quality active region for future development of DUV VCSELs.

5 TEMPERATURE DEPENDENCE OF CRYSTALLINE QUALITY OF ALN LAYER GROWN ON SAPPHIRE SUBSTRATE BY MOCVD

5.1 Introduction

Deep-ultraviolet (DUV) emitters based on III-nitrides including light-emitting diodes (LEDs) and laser diodes (LDs) can be applied to important areas such as disinfection, digital data storage, bio-agent detection, and wireless communication. As mentioned earlier, the bandgap of III-nitrides need to be larger than 4.4 eV to emit light in the DUV range. As shown in Figure 3 above, there are potentially three candidates. They are ternaries InAlN and AlGaN, and quaternary InAlGaN. However, the MOCVD growth of III-nitrides comprising both Al and In is still very challenging due to incompatibility of growth temperatures [19]. Thus AlGaN has been the primary material for high-performance III-nitride DUV emitters. Since the bandgap energy of AlN is the highest among the III-nitrides, AlN is transparent to DUV emission from AlGaN. In addition, AlN has a close lattice constant with AlGaN as shown in Figure 3. Therefore AlN is ideal for being a 'template' layer on which AlGaN layers are grown.

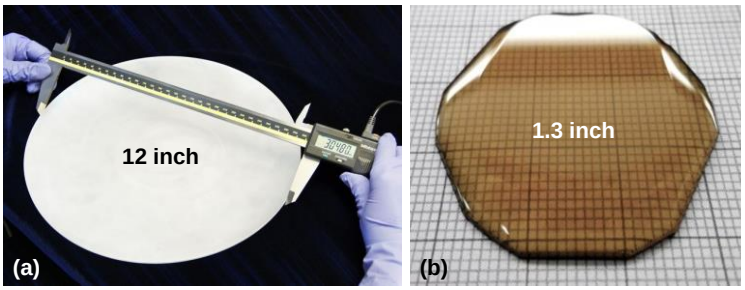

Figure 20. The state-of-the-art (a) sapphire substrate and (b) AlN substrate in terms of lateral dimension.

Although bulk AlN substrates fabricated by the sublimation-recondensation process (physical vapor transport growth) at temperatures over 2000 °C are ideal for the

growth of DUV emitters due to low dislocation density of less than 10^5 /cm^{-2} as well as reduced lattice and thermal expansion mismatch with high-Al content III-nitrides, the application is constrained by limited supply, high cost, DUV absorption, and small substrate size. As shown in Figure 20(a)-(b), the diameter of state-of-the-art sapphire substrate is nearly an order of magnitude larger than that of AlN substrate, leading to usable surface area difference of about 100 times [20,21]. In addition, the yellowish color of AlN substrate in Figure 20(b) is associated with carbon impurity that leads to strong absorption in the DUV spectrum as shown in Figure 21 [22].

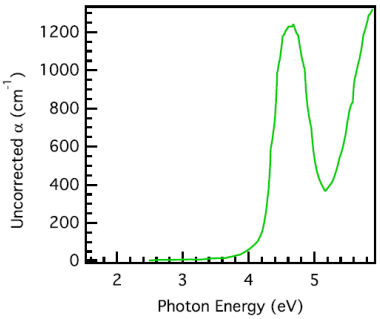

Figure 21. Absorption spectrum for a bulk AlN substrate, showing strong absorption at photon energy above 4 eV or wavelengths below 300 nm due to carbon impurities.

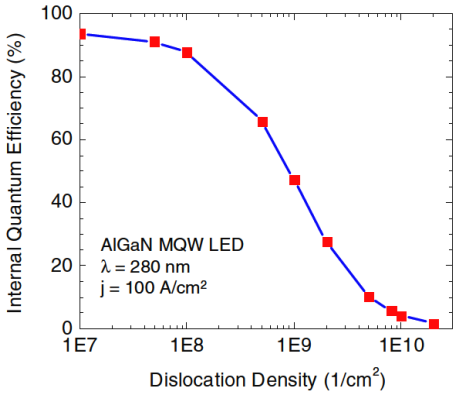

Figure 22. Simulated internal quantum efficiency (IQE) versus the dislocation density for UV LEDs emitting at 280 nm.

Therefore commercialization of the III-nitride DUV emitters still largely relies on the use of AlN templates grown on the vastly-available, low-cost, DUV-transparent, and

larger foreign substrates especially (0001) sapphire substrates. However, the large lattice and thermal expansion mismatch between AlN and sapphire leads to high dislocation density. As performance of III-nitride DUV emitters is very sensitive to the dislocation-related non-radiative recombination centers [23,24] as exemplarily shown in Figure 22, it is crucial to reduce the dislocation density of AlN templates for the devices grown and fabricated thereon.

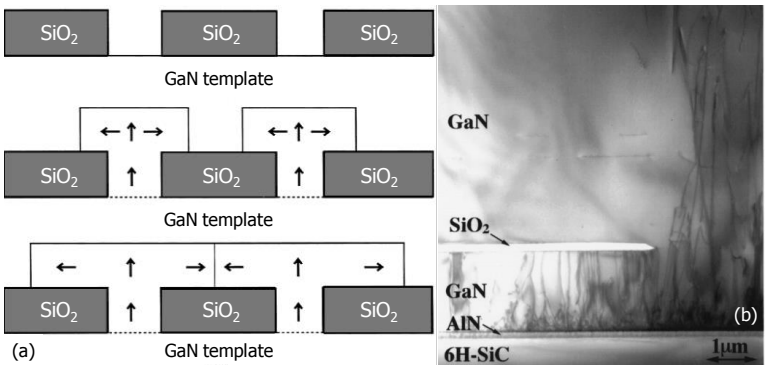

Figure 23. (a) Schematic process flow and (b) cross-sectional TEM image of an overgrown GaN on the SiO_2 mask.

One of the common approaches to reducing the dislocation density is the epitaxial lateral overgrowth (ELO), or lateral epitaxial overgrowth (LEO) where AlN layers are re-grown on patterned seeding AlN templates [25-28]. This approach was first used to grow new microelectronic devices with better performance in Si [29] GaAs [30] and InP [31] semiconductor materials in the 1980s. Since the late 1990s, the ELO was introduced to the growth of GaN on foreign substrates to reduce the dislocation density [32]. As shown in Figure 23(a), the GaN ELO starts with deposition of dielectric SiO_2 or Si_3N_4 mask layers on the GaN template. Then GaN can be grown from the mask-free GaN region. Because of high lateral growth rate of GaN, the ELO occurs over the SiO_2 mask layer under selected growth conditions [33]. As shown in Figure 23(b), the GaN layer over the mask layer, or

overgrown GaN layers had significantly lower dislocation density by a few orders of magnitude than that of the GaN layer grown from the mask-free GaN region [32].

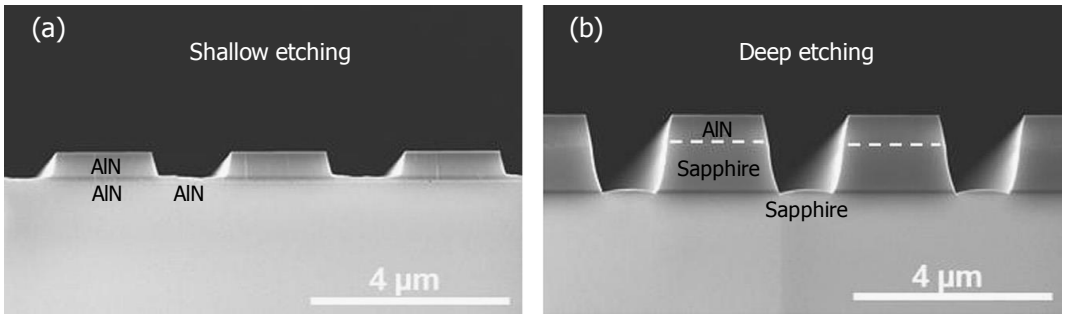

Figure 24. Cross-sectional views of the etching profiles for (a) shallowly etched and deeply etched (b) AlN/sapphire templates prior to the AlN ELO.

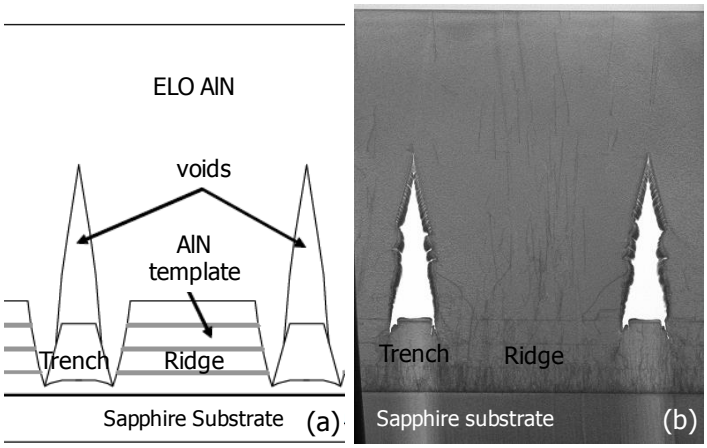

Figure 25. Cross-sectional schematic illustration and TEM image of an ELO AlN template.

In spite of success of the GaN ELO, the AlN ELO is more challenging due to low lateral growth rate of AlN layers. This means that it is more difficult to achieve the AlN coalescence or overgrowth over the dielectric mask layers. As a result, most of the successful AlN ELO studies have not used the dielectric mask layers to define the ELO region. Instead, the AlN ELO has been initiated by selectively etching the AlN templates into trench-patterned AlN templates. Depending on the depth of etching and thickness of the planar AlN template, the surface material of trenches can be either AlN, sapphire, SiC or other materials suitable for direct growth of AlN, as shown in Figure 24(a)-(b) [25].

Then an AlN layer, often thicker than 10 μm, is grown on both trenches and ridges. Because of the slower lateral growth rate than vertical growth rate of AlN, the AlN ELO often leaves air voids over the trenches, as shown in Figure 25(a)-(b) [26]. Similar to the GaN ELO, the region where lateral growth is more prominent, i. e. above the trenches, shows considerably lower dislocation density than that above the ridges. The lowest reported dislocation density of ELO AlN/sapphire template is 4×10^7 /cm^2, which is nearly two-order-of-magnitude lower than the planar AlN/sapphire in the same study [26].

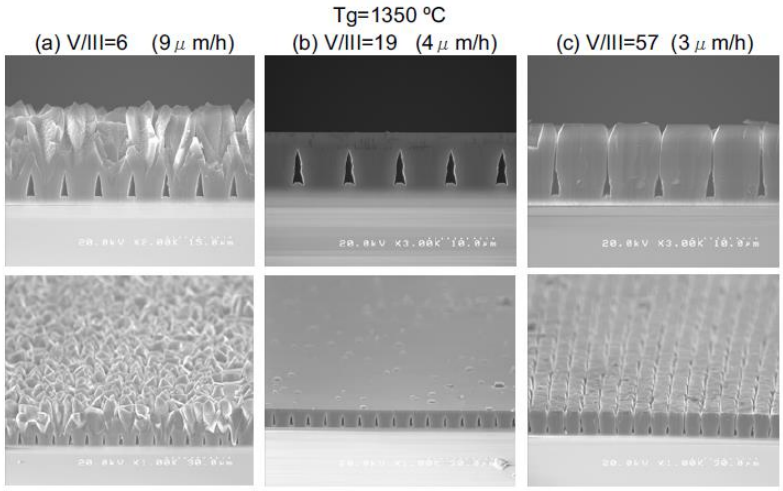

Figure 26. (a)-(c) SEM images of uneven surface of ELO-AlN templates on sapphire substrates under different growth conditions.

However, because the ELO approach involves cleanroom fabrication like etching as well as a regrowth process of a thick, often more than 10-μm thick layer to coalesce and form a flat layer over the patterned templates, it is associated with much more additional cost and processing time, uneven surface, and growth complexity. As shown in Figure 26(a)-(c), uneven surface is formed because of imperfect growth conditions for coalescence [26], which is very unfavorable for device growth and fabrication thereon.

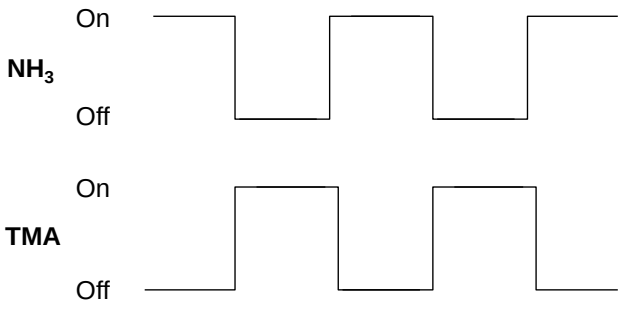

Figure 27. An exemplary gas flow sequence during the growth of AlN layer by MOCVD.

Another common approach, the pulse atomic layer epitaxy (PALE), focuses on alleviating low Al atomic mobility on the epitaxial surface. The N and/or Al sources are supplied in a pulse mode to allow Al atoms additional time to mobilize on the epitaxial surface [24,34,35], as shown exemplarily in Figure 27 wherein NH_3 and TMA supplies are pulsed alternatively during the growth of AlN template. In some studies, the ELO and PALE were both employed to accelerate the coalescence over the patterned templates [26,28].

In addition to the ELO and PALE, the high temperature growth above 1200 ^oC has been employed independently or jointly with the ELO and/or PALE to achieve low dislocation density and smooth surface morphology by metalorganic chemical vapor deposition (MOCVD), in that the mobility of Al atoms on the epitaxial surface is enhanced at high temperature [14,36-42]. Despite evidences of lowering the dislocation density considerably, the reported lowest dislocation density of planar AlN/sapphire templates grown at high temperatures is low 10^9 /cm^2 [23,40], which is still considerably higher than the ELO AlN/sapphire templates as discussed above. In the meantime, there are some concerns regarding the high temperature growth. On one hand, it requires a special reactor configuration such as higher capacity power supply and water cooling, which adds cost and complexity. On the other hand, the high temperature growth may also requires thermal

resistant coating for the wafer susceptor and special parts such as the quartz-free J-liner that are thermally stable and thus don't release impurity atoms [36]. It can also cause considerable thermal stress and cracks due to the large thermal expansion mismatch between AlN and sapphire [43]. Besides, the serious wafer bowing of AlN templates at high temperature can also deteriorate wafer uniformity in terms of the template thickness and the composition of layers grown heteroepitaxially on the template [44,45]. To overcome these issues, there have been some attempts to grow an AlN layer on sapphire [46] and SiC [47] substrates below 1200 ^{o}C. However, surface of these AlN templates was found to possess a high density of point defects. In other words, there have been very few successful studies of growing high-quality planar AlN templates on the sapphire substrates below 1200 ^{o}C to our knowledge. In addition, temperature-dependent experiments were carried out previously to grow the AlN templates at 1100-1500 ^{o}C [14,42,46]. However, the studies were performed with a large increment step of 100 ^{o}C. Hence it was not possible to find out variation of crystalline quality within a smaller range of temperature and thus potential optimum temperatures therein.

In this work, we carried out a temperature-dependent experiment to investigate the temperature influence on the crystalline quality of two-layer AlN templates. The template temperatures T_t ranged from 1050 to 1250 ^{o}C with a fine increment step of around 18 ^{o}C. The goal was to identify trends of crystalline quality variation and a proper temperature range which could lead to sufficient Al mobility for the growth of high quality AlN/sapphire templates. Details of growth process and characterization are presented hereafter. Neither the ELO nor PALE approach was used in this study. The AlN crystalline

quality was characterized by X-ray diffraction (XRD) and atomic force microscopy (AFM).

5.2 Experiment

To investigate the temperature dependence of the AlN template quality, twelve crack-free AlN templates with a simple two-layer structure were grown by MOCVD at various template temperatures T_t on two-inch diameter (0001) sapphire substrates with an offcut angle of 0.2° toward the *a*-plane. This offcut angle is expected to lead to an atomic step terrace width of ~89 nm. The MOCVD system used in this study was an AIXTRON 3×2" close-coupled-showerhead (CCS) system. The emissivity-corrected surface temperature was measured by a dual-wavelength multiple-point pyrometric profiling system. Trimethylaluminum (TMA) and ammonia (NH_3) were used as precursors and hydrogen (H_2) as carrier gas. Prior to the AlN growth, the susceptor and sapphire substrates were baked at 1100 °C for five minutes in a H_2 ambient. A dose of 0.57 µmol of TMA was deposited at 930 °C after the bake to pre-condition the sapphire surface for Al-polar AlN layers [48].

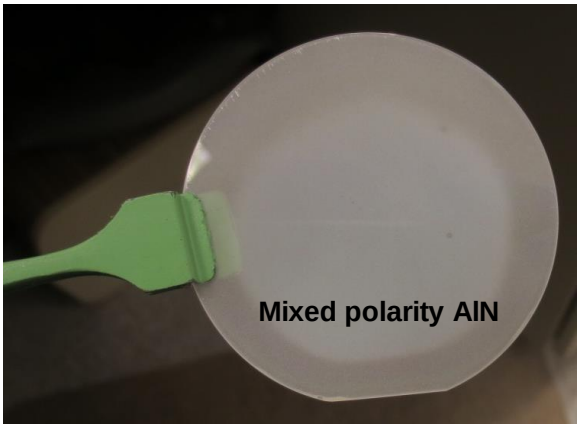

Figure 28. Photograph of the AlN/sapphire template grown by the AIXTRON 3×2" CCS MOCVD system with insufficient dose of TMA pre-conditioning showing rough and hazy surface because of mixed polarity.

It is noted that the dose of TMA can vary depending on the reactor design. For instance, our similar 6×2" CCS MOCVD system does not need any TMA pre-conditioning to grow Al-polar AlN layers on the sapphire substrate. The lack of a requirement for TMA pre-conditioning was also observed by Reentila, et al., using an 11×2" planetary MOCVD system [37]. However, with insufficient TMA pre-conditioning in our 3×2" CCS MOCVD reactor, the surface of the AlN/sapphire template becomes rough and hazy, which is attributed to the mixed polarity AlN [48,49], as exemplarily exhibited in Figure 28.

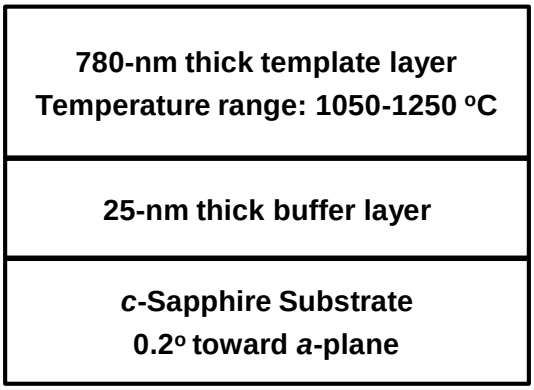

Figure 29. Cross-sectional schematic diagram of the two-layer AlN templates structures grown on the (0001) sapphire substrates with different template layer temperatures T_t at 1050-1250 °C.

As shown in Figure 29, the AlN template structure comprised two layers: (1) a 25-nm thick AlN buffer layer grown on the sapphire substrate at 930 °C after the TMA pre-conditioning, and (2) subsequently a 780-nm thick AlN template layer grown at one constant template temperature T_t within the range of 1050-1250 °C with an increment step of around 18 °C and a V/III ratio of 77. Except the template temperature T_t, the other growth parameters were kept the same for all of these twelve samples. The total flow rate of precursors and carrier gas was kept constant at 20 slm. The reactor pressure was set at 85 mbar or 64 Torr during the growth of AlN layers. Despite the difference in temperatures,

the growth rate of AlN template layer for all the samples measured by the *in-situ* reflectance was around 1.76 µm/h.

5.3 Result and discussion

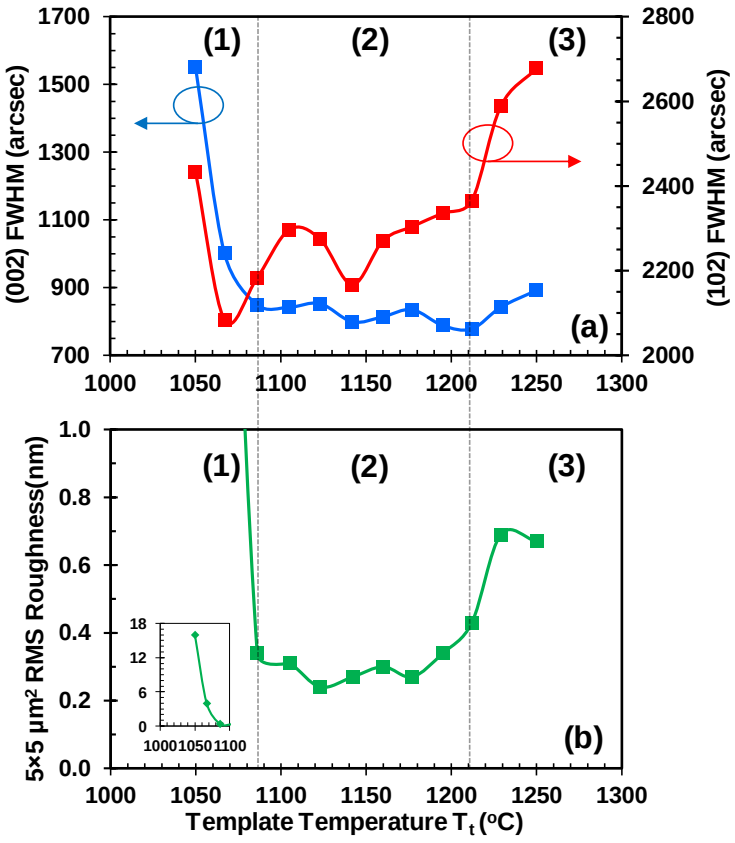

Figure 30. (a) FWHM's of XRD (002) and (102) ω-scans, and (b) 5×5 µm^2 RMS roughness extracted from Figure 31 of the two-layer AlN/sapphire templates as a function of temperatures T_t.

The template temperature T_t dependence of the structural quality of the AlN templates were studied partially in terms of full-width at half maximum (FWHM) of XRD symmetric (002) and asymmetric (102) ω-scans as shown in Figure 30(a). The FWHM's of symmetric (002) ω-scan and asymmetric (102) ω-scans correspond to and are proportional to the screw dislocation density and the edge dislocation density, respectively. The screw dislocation and edge dislocation originate from the stacking faults tilting and

twisting grain boundaries, respectively. In addition, Figure 30(b) shows the 5×5 μm^2 RMS surface roughness as a function of the template temperature T_t, which was extracted from the AFM images of Figure 31(a)-(l). The horizontal temperature coordinates of Figure 30 (a)-(b) were aligned vertically. A close examination of Figure 30(a)-(b) reveals different trends of the template temperature T_t dependence of structural and morphological quality in three temperature ranges, as segregated by the dash line and summarized in Table 3.

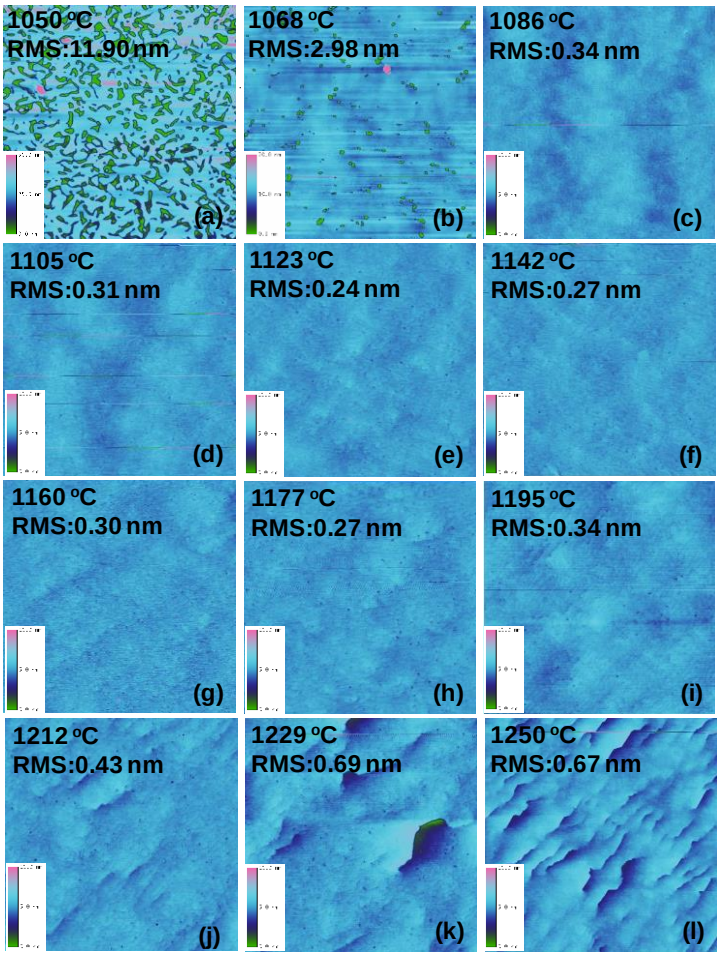

Figure 31. (a)-(l) 5×5 μm^2 AFM images of the AlN templates at different template layer temperatures T_t at 1050-1250 °C. The RMS roughness for each sample is included.

In the first template temperature T_t range of 1050-1086 °C, the (102) FWHM and especially (002) FWHM at the lower temperature of 1050 °C were significantly higher than

those at higher temperatures of 1068 and 1086 ^{o}C, indicating poor crystalline quality with high density of dislocations. As shown in Figure 31(a), large and deep pits were found on the surface, leading to high RMS roughness and suggesting incomplete coalescence of initial AlN three-dimensional (3D) islands at 1050 ^{o}C attributed to low Al atom mobility. As the template temperature T_t increased to 1068 ^{o}C, a steep decrease of the (002) FWHM, (102) FWHM, and RMS roughness was observed, indicating a dramatic improvement of crystalline quality because of the enhanced Al atom mobility. This was also reflected by the significant reduction of surface pit density shown in Figure 31(b)-(c), as compared with Figure 31(a).

In the second template temperature T_t range of 1086-1212 ^{o}C, the (002) FWHM stayed relatively constant, indicating the density of screw dislocation and thus the tilting of grain boundaries were not sensitive to the temperature change in this range. On the other hand, the (102) FWHM rose slowly with elevated temperatures, suggesting a gradual increase of the density of twisting boundaries. The surface was very smooth as shown in Figure 31(c)-(i) with RMS roughness between 0.24 nm to 0.34 nm. This suggests that the Al atom mobility was sufficient at template temperatures T_t as low as 1086 ^{o}C that had been largely considered to be a relatively low temperature for AlN growth by MOCVD previously.

In the third template temperature T_t range of 1212-1250 ^{o}C, the (002) FWHM still stayed relatively constant. But the (102) FWHM increased rapidly with higher template temperatures T_t, suggesting a template temperature T_t of 1212 ^{o}C may be a threshold, beyond which the formation of edge dislocations was accelerated. This implied that the tilting of grain boundary was insensitive to the temperature changes in the template

temperature T_t range of 1086-1250 ^oC, while the twisting became rapidly severe above 1212 ^oC. Meanwhile, the surface roughness increased due to the gradual formation of periodic macro-steps from 1212 ^oC as shown in Figure 31(j)-(l). Such surface morphology is undesirable for the fabrication of high-quality heterostructures [50]. A similar surface morphology was also observed by a recent study by Li, et al., who reported growing the AlN template layer at 1250^o C [49]. The formation of macro-steps can be attributed to a thermodynamic process wherein the mobility of Al atoms was high enough that the diffusion length of Al atoms was longer than the atomic step terrace width at high temperature [51]. Although the formation of macro-steps appeared simultaneously with the accelerated increase of edge dislocation density, Shen, et al., have shown that the macro-steps can lead to dislocation bending and thus reduction of the dislocation density in GaN and AlN templates grown on sapphire substrates [52,53]. This means that the macro-steps should not be the cause of increased edge dislocation density.

In the growth of AlN templates on sapphire substrates, Okada, et al., have shown that the edge dislocation density was annihilated in the transition from three-dimensional (3D) island growth to two-dimensional (2D) growth and a slower transition leads to more efficient annihilation of threading dislocation originated from buffer layers [39]. In this work, the 3D-island growth dominated in the buffer layer at 930 ^oC and the template layer grown at or above 1050 ^oC provided 2D growth. At lower template temperatures T_t, the Al atom mobility was smaller leading to a slower transition from 3D to 2D growth. The slower transition thus enhanced the bending and annihilation of edge threading dislocation. At higher template temperatures T_t, the transition from 3D to 2D growth was shorter, leading to higher edge dislocation density.

Table 3. Trends of template temperature T_t dependence of FWHMs of XRD (002) and (102) ω-scans as well as 5×5 μm^2 RMS roughness of the two-layer AlN templates at 1050-1250 ^{o}C.

T_t Range ^{o}C	(002) FWHM	(102) FWHM	5×5 μm^2 RMS roughness
(1) 1050-1086	Decrease	Decrease	Decrease
(2) 1086-1212	Constant	Constant	Constant
(3) 1212-1250	Constant	Increase fast	Increase fast

Given these results and discussions, it is evident that the higher temperature growth does not necessarily lead to higher-quality AlN/sapphire templates as a result of the increased edge dislocation density and surface roughness. It is important to note that this conclusion is different from some previous studies, where the high-temperature growth yielded better crystalline quality than the lower-temperature growth [14,42,46]. The discrepancy may result from different growth conditions including the use of PALE, temperature range, growth rate, V/III ratio, reactor condition, and layer structure. However, herein the AlN templates with a simple two-layer structure already shows relatively low surface roughness without the use of PALE which indicates adequate Al atom mobility can be obtained at temperatures as low as 1086 ^{o}C. Hence with further optimizations, high-quality planar AlN/sapphire templates may be potentially obtained at such reduced temperatures which are reachable by most of the III-nitride MOCVD reactors.

5.4 Conclusion

The dependence on template temperatures T_t of crystalline quality of two-layer planar AlN/sapphire templates grown by MOCVD was studied with a fine increment step of around 18 ^{o}C at 1050-1250 ^{o}C. Below 1068 ^{o}C, the templates showed poor crystalline quality with large and dense pits and high XRD (002) and (102) FWHM's, which were caused by incomplete coalescence of 3D AlN islands as a result of the low Al atom

mobility. The template surface became pit-free and smooth at 1086 ^{o}C, indicating sufficient Al atom mobility. Above 1086 ^{o}C, the edge dislocation density increased with temperatures, which may be attributed to the shorter 3D to 2D growth mode transition. Above 1212 ^{o}C, surface macro-steps were formed due to longer diffusion length of Al atoms than the expected step terrace width. In addition, the edge dislocation density increased quickly which may be caused by an enhanced effect of the shorter 3D to 2D growth transition. The screw dislocation density was insensitive to the temperature change. This study suggests that high temperature growth does not necessarily lead to high-quality AlN/sapphire templates, which however can be potentially achieved at reduced temperatures of around 1086 ^{o}C with further optimization, a temperature range accessible by most of the modern III-nitride MOCVD systems.

6 GROWTH OF HIGH QUALITY ALN TEMPLATE ON SAPPHIRE SUBSTRATE AT PRACTICAL MOCVD TEMPERATURES

6.1 Introduction

As mentioned in the beginning of last chapter (5.1 Introduction), III-nitride deep-ultraviolet (DUV) emitters including light-emitting diodes (LEDs) and laser diodes (LDs) have numerous important applications. Comprehensive considerations of cost, throughput, and DUV absorption indicates that the AlN template on sapphire substrate is currently the ideal platform to grow high Al-content AlGaN layers for DUV emitters over the AlN and SiC substrates. To achieve the high quality AlN template grown heteroepitaxially on sapphire, various approaches like epitaxial lateral overgrowth (ELO), pulse atomic layer epitaxy (PALE), and high growth temperature of over 1200 ^{o}C have often been used collectively in the prior arts. However, they suffer from issues including complexity, transferability and high cost. In particular, a large portion of research-scale and most of the production-scale MOCVD systems cannot exceed growth temperatures over 1150 ^{o}C.

To address these issues, there have been some attempts to grow AlN layers on sapphire [46] and SiC [47] substrates below 1200 ^{o}C. However, the surface of these AlN layers was found to suffer from a high density of defects. In addition, there have been few successful studies of growing high-quality planar AlN layers on the sapphire substrates below 1200 ^{o}C. The detailed temperature dependence study as shown in the last chapter indicated that the Al atom mobility was adequate to achieve coalesced and smooth surface at temperatures as low as 1086 ^{o}C without the use of ELO or PALE. Hence the planar AlN layers with high quality may be obtainable at such temperatures that are practical for most of the MOCVD systems.

In this work, we developed a simple recipe to grow high-quality AlN layers at relatively-low growth temperatures up to 1130 ^{o}C, which are accessible for most of the modern III-nitride MOCVD systems. Details of the growth process and characterization are presented hereafter. Neither the ELO nor PALE process was used in this study. The crystalline quality of AlN layers was assessed by scanning electron microscopy (SEM), atomic force microscopy (AFM), X-ray diffraction (XRD), photoluminescence (PL), cathodoluminescence (CL), transmission electron microscopy (TEM), and secondary ion mass spectroscopy (SIMS).

6.2 Experiment

The AlN heteroepitaxial structure comprised three layers grown under different conditions. The MOCVD system we used was an AIXTRON 3×2" close-coupled-showerhead (CCS) system. The emissivity-corrected surface temperature was measured by a dual-wavelength multiple-point pyrometric profiling system. Trimethylaluminum (TMA) and ammonia (NH_3) were used as precursors and hydrogen (H_2) as carrier gas. The total flow rates of precursors and carrier gas were kept constant at 20 slm. Prior to the AlN growth, the susceptor and sapphire substrates were baked at 1100 ^{o}C for five minutes in a H_2 ambient. A dose of 0.57 μmol of TMA was deposited at 930 ^{o}C after the bake to pre-condition the sapphire surface for growing Al-polar AlN layers [48].

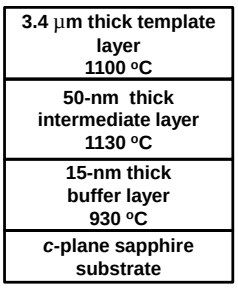

Figure 32. Cross-sectional schematic diagram of the three-layer AlN/sapphire structure with corresponding growth temperatures.

As shown in Figure 32, the growth started with a 15-nm thick AlN buffer layer grown at 930 ºC with a V/III ratio of 1500 on a 2-inch diameter (0001) sapphire substrate with an offcut angle of 0.2˚ toward *m*-plane. Afterwards, a 50-nm thick AlN intermediate layer was deposited at 1130 ºC with a V/III ratio of 74 for a short growth period of 100 s. The importance of the AlN intermediate layer is discussed in Section 3. The growth was concluded by depositing a 3.4-µm thick AlN template layer grown at 1100 ºC at a V/III ratio of 66. The reactor pressure was set at 85 mbar (64 Torr) during the growth of the AlN layers. The growth rate of the template layer was 2.30 µm/h or 0.64 nm/s, which is considered to be relatively fast for AlN growth by MOCVD. Based on the supplying molar flow of TMA and growth rate, the growth efficiency of the AlN template layer was calculated to be 2134 µm/mol, or 36% of the injected TMA was effectively incorporated to grow the AlN template layer. This growth efficiency was thus similar to that of a previous study using an extremely low V/III ratio of 10 to grow AlN layers efficiently [54].

6.3 Result and discussion

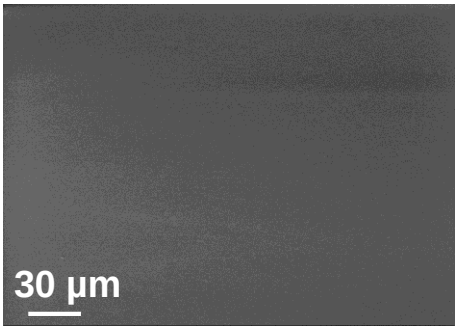

Figure 33. Oblique-view SEM image for surface morphology of the three-layer AlN/sapphire structure.

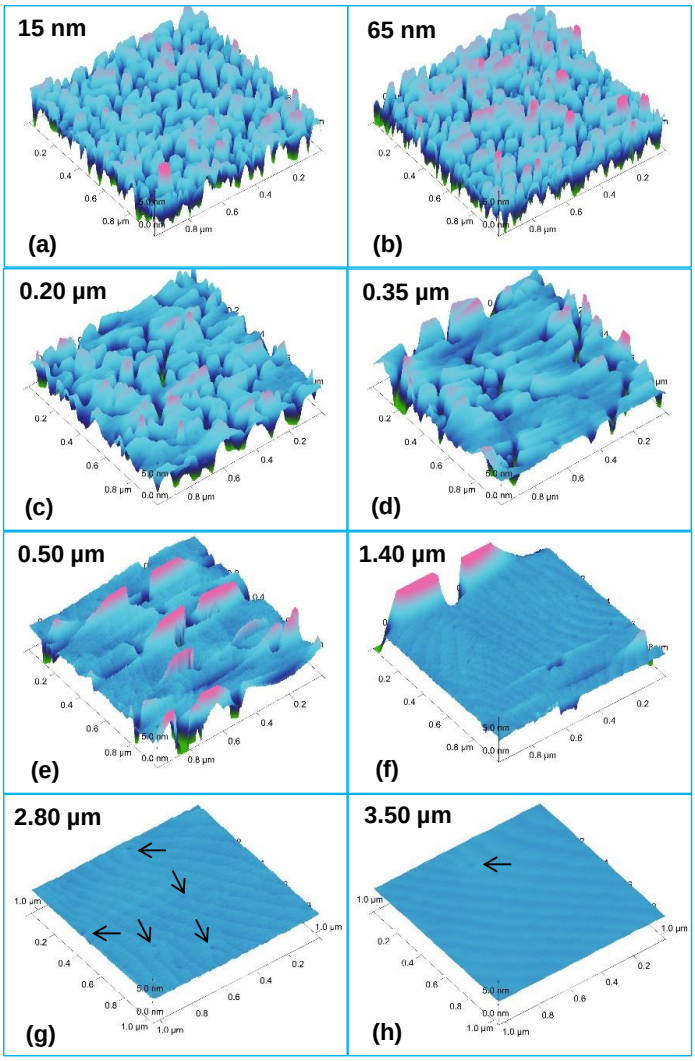

Figure 34. (a)-(h) 1×1 μm^2 AFM images showing surface morphology evolution of the three-layer AlN/sapphire structure as a function of total AlN layer thickness shown on the upper left cover of each figure. (h) corresponds to the complete sample structure with the RMS roughness was 0.07 nm.

The SEM image in Figure 33 exhibits surface morphology of the AlN/sapphire structure. Neither pits nor hillocks were visible, indicating a smooth surface because of good coalescence and two-dimensional (2D) growth even at relatively low growth temperatures. To investigate the evolution of the surface morphology, the growth was interrupted at different stages and the surface morphology was observed by AFM as shown in Figure 34(a)-(h). Each figure corresponds to a sample grown independently on a sapphire substrate to avoid defect formation from a regrown surface, and contamination

induced during the measurement. As shown in Figure 34(a), three-dimensional (3D) growth dominated in the lower-temperature buffer layer with lateral island dimensions of around 100 nm. With further growth of the 50-nm AlN intermediate layer at 1130 ºC, the surface morphology started to shift from 3D to 2D, as shown in Figure 34(b). By switching to the growth of the final AlN template layer at 1100 ºC, the transition from 3D to 2D growth modes continued and the surface began to planarize as shown in Figure 34(c)-(f). Surface pits caused by uncoalesced islands were still seen at a total thickness of 1.40 μm where atomic steps started to become visible. However, the pit density in Figure 34(f) was significantly reduced compared to those in Figure 34(a)-(e), indicating proximity to the complete coalescence. With a thicker AlN template layer, the surface pits disappeared at a total thickness of 2.80 μm as shown in Figure 34(g). In Figure 34(g), some threading dislocations appearing as surface point defects marked by arrows were visible at the coalescence points as step terminations. In Figure 34(h) shows the surface of the complete AlN/sapphire structure, and well-defined steps and terraces are observed, indicating an Al-polar surface with dominant 2D step-flow growth. The height difference between terraces was in the range of 0.20-0.30 nm corresponding to one monolayer of (0001) AlN ($c/2$ = ~ 0.25 nm). Root-mean-square (RMS) roughness was 0.07 nm, which is comparable with that of some polished bulk AlN substrates [55]. Thus the heteroepitaxial growth of AlN/sapphire at temperatures ~1100 ºC can provide smooth surfaces for the subsequent deposition of III-nitride layers on top. In addition, the threading dislocation density of the surface was greatly reduced as compared to Figure 34(g), suggesting that the threading dislocations continued bend with an increased layer thickness after the surface was fully coalesced.

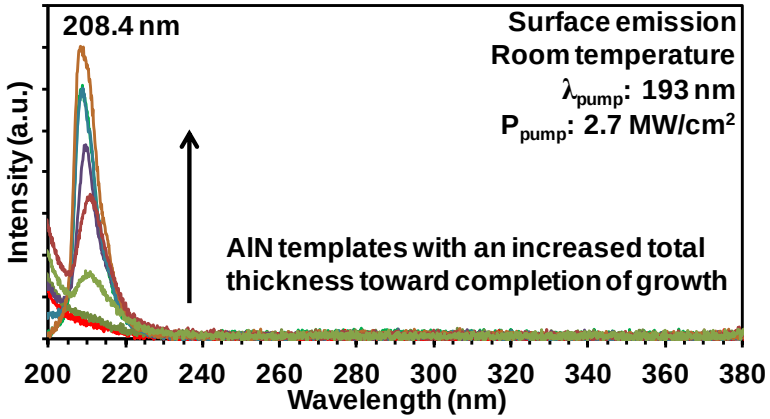

Figure 35. Room-temperature PL spectra of the AlN/sapphire structure with different total layer thicknesses toward growth completion, corresponding to Figure 34(a)-(h). The spectral curves of the 1.40 µm and 2.80 µm thick AlN samples overlap each other, which may be due to similar radiative efficiency.

Table 4. FWHMs of XRD (002) and (102) ω-scans as well as PL characteristics of the three-layer AlN/sapphire structure as a function of total thickness through the growth evolution.

Total Thickness µm	Corresponding AFM figure	(002) FWHM arcsec	(102) FWHM arcsec	PL Peak λ nm	PL FWHM nm
0.015	Figure 3(a)	3107	4266	NA	NA
0.065	Figure 3(b)	2581	3899	NA	NA
0.20	Figure 3(c)	1908	2783	210.9	12.0
0.35	Figure 3(d)	1548	1987	210.9	9.6
0.50	Figure 3(e)	1138	1670	209.7	6.2
1.40	Figure 3(f)	601	914	208.9	6.2
2.80	Figure 3(g)	349	659	208.9	5.9
3.50	Figure 3(h)	280	480	208.4	6.9

Room-temperature PL and XRD were used to characterize the samples presented in Figure 34(a)-(h), as shown in Figure 35 and Table 4. The top-surface-emitted PL spectra were obtained via optically pumping the samples by a pulsed ArF excimer laser (λ = 193 nm) with a pumping power density of 2.7 MW/cm^2. Details of the optical pumping experiment setup can be found in Chapter 6. In Figure 35, high-energy spectral tails at $\lambda <$ 205 nm were from the unabsorbed pumping laser emission. As shown in Figure 35, no

considerable emission was seen for the samples with total thicknesses of 15 and 65 nm corresponding to the completion of buffer and intermediate layers with broad (002) and (102) FWHMs shown in Table 4, indicating very low radiative efficiency. The band-edge emission began to be seen at 210.9 nm from the sample with a total thickness of 200 nm and reduced (002) and (102) FWHMs of 1908 and 2783 arcsec. The PL emission intensity generally increased with the thickness and smaller (002) and (102) FWHMs, which implied enhanced radiative efficiency due to reduced dislocation densities. Despite different thicknesses, the spectral curves of the 1.40 μm- and 2.80 μm-thick AlN samples overlap each other, which may be due to similar radiative efficiency. The smallest (002) and (102) The XRD FWHMs were 280 and 480 arcsec, suggesting relatively low mosaicity and dislocation density. The spectral FWHM decreased to as narrow as 5.9 nm for a total AlN thickness of 2.80 μm. It increased to 6.9 nm probably caused by a secondary bound-exciton peak [40] for the AlN/sapphire structure with a total thickness of 3.50 μm. In addition, a blueshift in peak wavelength with increased peak intensity was observed with the shortest peak wavelength of 208.4 nm for the complete structure, which can be attributed to the increased compressive strain with larger thicknesses [56]. There was no considerable deep level emission up to 380 nm, indicating low density of deep-level recombination centers.

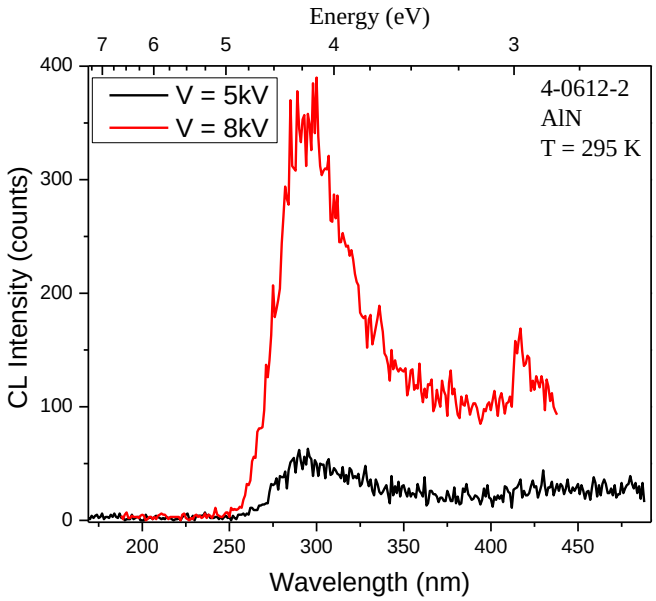

Figure 36. CL spectra with different e-beam energies of the AlN template.

The deep-level recombination centers were further investigated by the CL experiments. Electron beams (e-beams) with different acceleration voltages of 5 and 8 kV were pumped on the surface of 3.50-μm thick AlN template, with estimated penetration depths along *c*-axis of 356 and 780 nm, respectively [57]. A concave mirror is place above the sample to collect emitted light and reflect them to the monochromator which is then connected to a photomultiplier tubes (PMT). In comparison, the penetration depth of excitation laser beam of PL measurement is estimated to be 100 nm. In addition, the individual electron energy is a few orders of magnitude higher than that of the excited photon energy, which can be used to excite band-edge transitions and deep-level recombination centers. Thus CL provides more insights with regards to the deep-level recombination centers below the topmost portion of the AlN layer. As shown in Figure 36, weak emission peaked at around 300 nm (4.1 eV) with a long tail extending towards longer wavelengths is observed at the lower acceleration voltage of 5 kV. At the higher voltage of 8 kV, the emission intensity is significantly enhanced while a similar spectral shape is

retained. This indicates that the density of deep-level centers increases rapidly at a large depth of the AlN layer. It is important to note that the band-edge emission is absent from the CL spectra. This is because most of the band-edge emission of AlN, if any, is dominantly TM-polarized, which emits towards direction perpendicular to the *c*-axis [58]. Thus the concave mirror will not be able to collect the emission since the mirror is above the sample. The polarization of emission from AlGaN materials will be discussed in detail in Chapter 7.

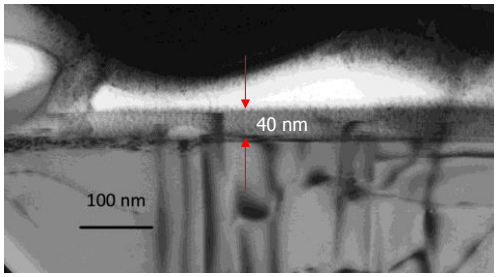

Figure 37. Cross-sectional TEM image showing thickness of the measured AlN/sapphire template.

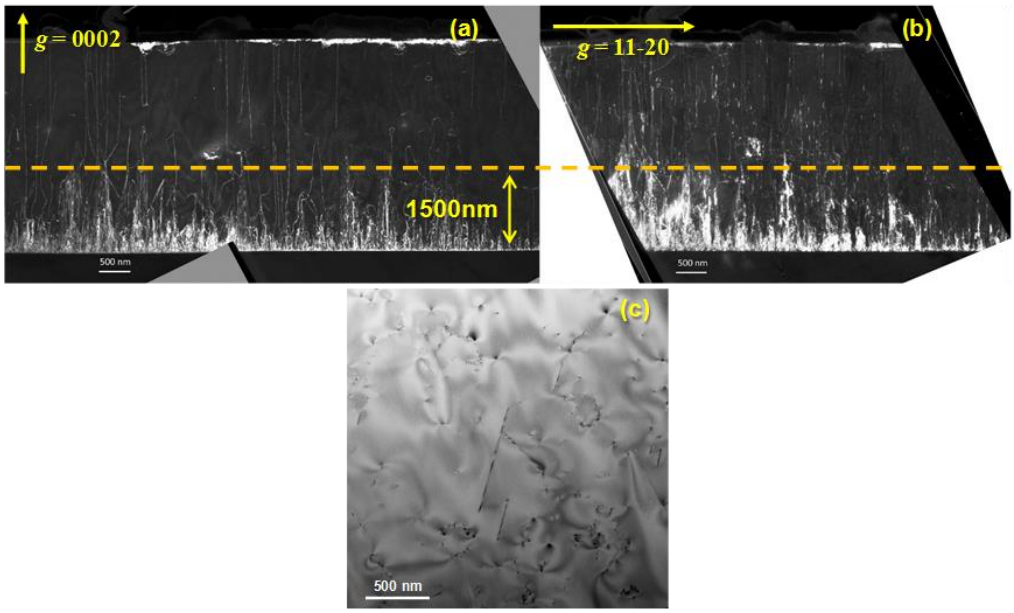

Figure 38. Dark-field cross-sectional TEM images with (a) $\boldsymbol{g}$ = 0002 and (b) $\boldsymbol{g}$ = 11-20, wherein the yellow dash line shows approximately where most of the dislocations were annihilated, and (c) Plan-view TEM image of the three-layer AlN/sapphire structure.

To determine the dislocation density of the AlN three-layer AlN/sapphire structure, TEM samples for cross-sectional and plan-view imaging were prepared by mechanical wedge-polishing techniques, followed by Ar ion milling at 3.5 keV. The resulting thickness of TEM sample is 40 nm, as shown in Figure 37. The microstructure of the AlN heteroepitaxial layer was studied using a JEOL 4000EX TEM operating at 400 kV. Figure 38(a)-(b) show dark-field cross-sectional TEM images under the two-beam condition with $\boldsymbol{g}$ = 0002 and $\boldsymbol{g}$ = 11-20, respectively. The plan-view image was taken under diffraction condition $\boldsymbol{g}$ = 11-20. The sample was intentionally titled away from the zone axis to project the threading dislocations as segments in the image. Since the dislocations seen in Figure 38(a) were also visible in Figure 38(b), it suggested that there was no pure screw dislocation, and thus those observed in Figure 38(a) were of mixed type instead. The densities of mixed and edge dislocations near the epitaxial surface as analysed from Figure 38(a)-(b), were 1.0×10^9 /cm^2 and 1.5×10^9 /cm^2, respectively. Hence the total dislocation density was ~2.5×10^9 /cm^2, which agrees well with the plan-view TEM experiment as shown in Figure 38(c). Thus the total dislocation density is comparable to those of some recent studies where the AlN layers were grown on sapphire substrates at temperatures above 1300 ^{o}C by taking into account the thickness differences [24,38,41].

The cross-sectional TEM images in Figure 38(a)-(b) were further compared with TEM analysis results in the previous studies regarding the growth of high-quality AlN layers on sapphire substrates [37-39,41]. In those studies where temperatures higher than 1300 ^{o}C were employed, most of the dislocations were annihilated at a thickness of less than 500 nm from the AlN/sapphire interface. However, as shown in Figure 38(a)-(b), most of the dislocations were gradually removed and finally annihilated at larger thicknesses of

1000-1500 nm from the AlN/sapphire interface as marked by the yellow dashed line. This thickness range thus agrees with Figure 34(f), where the surface was close to full coalescence at a thickness of ~1.40 µm. Okada *et al.*, have shown that the slower annihilation of dislocations led to a reduction in the biaxial strain, dislocation density and cracks [39], which can be used to explain the relatively low dislocation density obtained in this study, in addition to the reduced thermal stress at lower temperatures [59]. Therefore the slower annihilation of dislocations was caused by a long transition from 3D to 2D growth modes due to a lower Al-atom mobility as compared to the ones at higher temperatures.

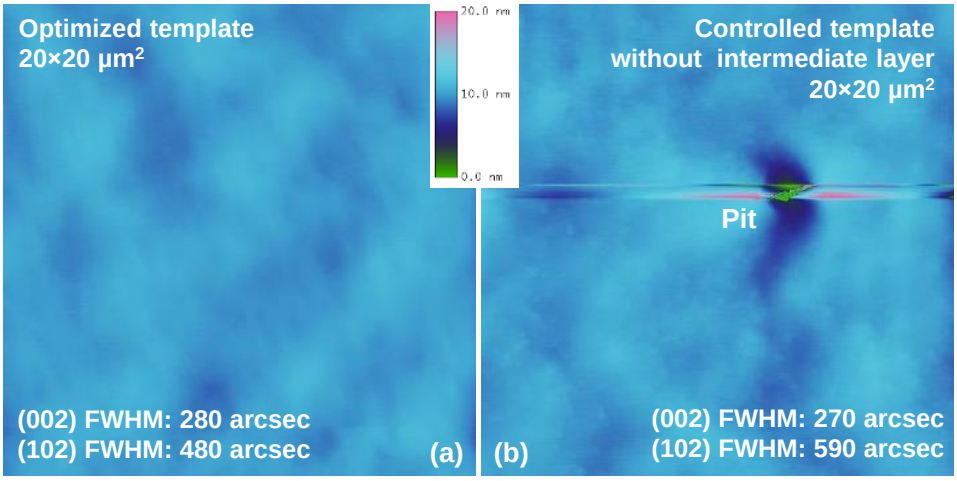

Figure 39. 20×20 µm² AFM images of the (a) three-layer AlN/sapphire structure and (b) two-layer AlN/sapphire structure which excluded the intermediate layer. FWHMs of XRD (002) and (102) ω-scans are included for comparison.

Although the interface between the AlN intermediate and buffer layers was hardly distinct in the cross-sectional TEM images as shown in Figure 38(a)-(b), the importance of 50-nm thick AlN intermediate layer was shown by growing a two-layer AlN/sapphire structure which excluded the intermediate layer. Otherwise the growth conditions and layer structure of the two-layer AlN/sapphire structure were the same as those of the three-layer

AlN/sapphire structure. The 20×20 μm^2 AFM images in Figure 39(a)-(b) show surface morphology of the three-layer and two-layer AlN/sapphire structures. The XRD (002) and (102) FWHMs are also included for comparison. Without the AlN intermediate layer, uncoalesced surface pits with an average density of ~3.75×10^5 cm^{-2} a lateral dimension of a few micrometers can be seen on the surface of controlled three-layer AlN/sapphire structure, whereas the surface of three-layer AlN/sapphire structure was pit-free. The (002) FWHMs of both AlN/sapphire structure were similar. However, the (102) FWHM of two-layer AlN/sapphire structure was considerably larger than that of the three-layer AlN/sapphire structure. This implies that the higher Al mobility at 1130 ^oC accelerated 2D growth and thus coalescence of AlN 3D islands, which help annihilate the edge dislocations and thereby reduced the (102) FWHM.

Table 5. Concentrations of residual impurities including C, H, O, and Si in the AlN template layer analyzed by SIMS. NA stands for that the data is non-available.

Reference	Growth Temperature ^oC	C atoms/cm^3	H atoms/cm^3	O atoms/cm^3	Si atoms/cm^3
This work	1100	8×10^{17}	4×10^{17}	1×10^{18}	2×10^{16}
Ref. 17	1600	4×10^{16}	7×10^{17}	1×10^{18}	2×10^{18}
Ref. 10	1500	NA	NA	5×10^{17}	1×10^{17}
Ref. 10	1400-1300	NA	NA	$1\text{-}10\times10^{19}$	NA
Ref. 28	1300	1×10^{17}	9×10^{17}	9×10^{17}	NA
Ref. 21	1300-1200	2×10^{18}	2×10^{18}	7×10^{17}	NA
Ref. 21	1100	2×10^{18}	4×10^{18}	1×10^{19}	NA
Ref. 17	1100	3×10^{17}	2×10^{19}	8×10^{19}	3×10^{18}

The residual impurity concentrations of carbon (C), hydrogen (H), oxygen (O), and silicon (Si) in the three-layer AlN/sapphire structure were analyzed by SIMS. The result is presented in Table 5 where some previously reported AlN/sapphire data is included for comparison [14,36,46,60]. The C, H, O, and Si concentrations were 8×10^{17}, 4×10^{17}, 1×10^{18},

and 2×10^{16} atoms/cm^3, which are comparable with those of the AlN layers grown at significantly higher temperatures. However, it is noted that the impurity concentrations were found to decrease considerably with higher temperatures in a number of previous studies [14,36,46]. Although the decreased impurity concentrations can be caused by an increased evaporation or sublimation rate of impurities from the AlN layers at higher temperatures, the impurity desorption from chamber parts may be enhanced at higher temperatures in the meantime. These two processes can mutually compensate each other. Thus the impurity concentration should depend on factors including the chamber part composition and temperature. For instance, the AlN growth study carried by Brunner, et al., was done in an oxygen-free reactor environment which avoided O impurity desorption from the chamber parts [36], where the reduction of O impurity with higher temperatures was likely due to the increased evaporation or sublimation of impurities from the AlN layers. In this study, the chamber contained a quartz liner surrounding the susceptor, which can introduce O impurities at higher temperatures. This can explain the comparable oxygen impurity concentrations of the AlN layers grown at 1100 ^{o}C and 1300 ^{o}C in the same growth chamber between this study and our previous study [60], respectively, as shown in Table 5.

In separate studies which will be presented in the next two chapters, AlGaN multiple-quantum-well (MQW) laser heterostructures for optical pumping experiments were grown on the AlN/sapphire templates developed in this study. State-of-the-art lasing operations were demonstrated, which demonstrates the application potential of these three-layer AlN/sapphire structure grown at practical temperatures.

6.4 Conclusion

Three-layer planar heteroepitaxial AlN layers which comprised a 15-nm thick buffer layer, a 50-nm thick intermediate layer, and a 3.4-μm thick template layer were grown at relatively low temperatures of 930, 1130, and 1100 ^{o}C, respectively on (0001) sapphire substrates. The importance of the thin intermediate layer was shown by a controlled experiment where the intermediate layer grown at 1130 ^{o}C was found to promote 2D growth to prevent surface pits from uncoalesced islands and reduce edge dislocations. The total dislocation density of template layer near the surface was 2.5×10^{9} /cm^{2} determined by TEM, which is comparable to some recently reported planar AlN layers grown on sapphire substrates at temperatures above 1300 ^{o}C. In addition, the 20×20 and 1×1 μm^{2} AFM scans show low RMS roughness values of 0.50 nm and 0.07 nm with step terraces, respectively. The relatively low dislocation density and smooth surfaces were attributed to low thermal stress and decreased biaxial strain because of slower dislocation annihilation. The PL measurements exhibited strong and narrow band-edge emission from the surface. The impurity concentrations were relatively low and comparable to those of the AlN layers grown at higher temperatures believed to be due in part to a reduced impurity desorption from the chamber parts at relatively low growth temperatures. Because the highest growth temperature was 1130 ^{o}C for a relatively short period of time and the sample comprised a simple three-layer structure without the use of PALE or ELO, the growth condition of this study is transferrable to most of the modern MOCVD systems.

7. DEMONSTRATION OF LOW-THRESHOLD DEEP ULTRAVIOLET LASING FROM ALGAN HETEROSTRUCTURE GROWN ON SAPPHIRE SUBSTRATE

7.1 Introduction

Deep-ultraviolet (DUV) emitters with wavelengths shorter than 280 nm have numerous applications such as high-density optical storage, disinfection, and biochemical identification. However, most of the commercially available DUV emitters including mercury lamps, quadrupled Nd:YAG lasers, and excimer lasers have limitations in many applications due to their large footprint, poor reliability or toxicity. Recently, the III-N semiconductor-based UV light emitters have drawn great attention, as the AlInGaN direct bandgap covers the entire DUV range (200-280 nm) which can lead to efficient, compact, and reliable DUV emitters.

The material quality of III-N semiconductors, especially for $Al_xGa_{1-x}N$ ($x > 0.50$) materials with bandgap energies from 4.4 to 6.0 eV, is the key to the development of high-performance DUV emitters. However, it has been shown that generally there is a degradation of the structural quality of heteroepitaxial $Al_xGa_{1-x}N$ ($x > 0.50$) materials with increasing Al molar fraction [61]. This has a negative impact on the performance of DUV emitters since the quantum efficiency is more sensitive to the dislocation-related non-radiative recombination centers than for InGaN-based visible emitters [62,63]. Although AlGaN electrically-driven DUV light-emitting diodes (LEDs) have been realized on foreign substrates such as sapphire [64], the high-dislocation density within the heteroepitaxial $Al_xGa_{1-x}N$ layers grown on foreign substrates makes the low-threshold

DUV lasing below 280 nm by optical pumping or electrical pumping difficult to achieve [8,15,17,65,66]as the defects are more detrimental to performance of lasers.

Recently, low-threshold optically-pumped DUV lasers containing AlGaN multiple-quantum wells (MQWs) have been demonstrated by homoepitaxial growth on (0001) bulk AlN substrates [11-13 ,67-69]. Bulk AlN substrates were used in these studies due to their low-dislocation density and reduction of the lattice mismatch and thermal expansion difference between the AlN substrate and Al-rich AlGaN epitaxial layers, thus leading to high-quality active regions with relatively low-dislocation density. However, because of limited availability, smaller area, impurity absorption, and high cost of the bulk AlN substrates today, it is much more desirable to grow DUV lasers on the vastly more available and lower-cost sapphire substrates.

In this work, we report optically-pumped AlGaN MQW DUV lasers grown on (0001) sapphire substrates by metalorganic chemical vapor deposition (MOCVD). Lasing at 249 nm ("the 249-nm laser") and 256 nm ("the 256-nm laser") with low pumping-power thresholds were demonstrated in an edge-emission configuration at room temperature (RT). Atomic-force microscopy (AFM), X-ray diffraction (XRD), and power-dependent photoluminescence (PL) and cathodoluminescence (CL) measurements were carried out to investigate crystalline quality of the lasers and stimulated emission characteristics.

7.2 Experiment

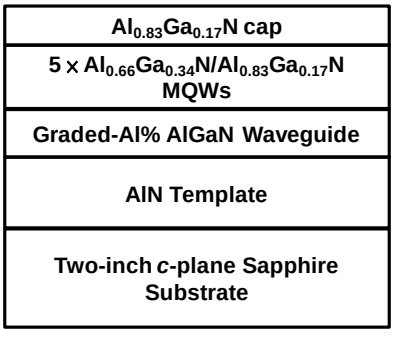

Figure 40. Cross-sectional schematic diagram of the DUV AlGaN MQW laser structure grown on a (0001) sapphire substrate.

The entire epitaxial AlGaN MQW laser structure was grown on 2-inch diameter (0001) sapphire substrates in a 3×2" AIXTRON low-pressure MOCVD reactor with a close-coupled showerhead configuration. As shown in the cross-sectional schematic diagram in Figure 40, the structure firstly comprises an AlN template layer deposited directly on the sapphire substrate with a thickness of 3.5 μm estimated by *in-situ* reflectance monitoring. To achieve lasing from the MQW active region grown on sapphire substrates, the use of an AlN/sapphire template with relatively low threading dislocation density (TDD) was necessary to reduce the dislocation density in the active region and thus improve gain therein. In this work, the TDD of the template layer was 2.5×10^9 /cm^2 as determined by cross-sectional transmission-electron microscopy (TEM). This level of TDD was shown to lead to an estimated internal quantum efficiency (IQE) of ~40-60% for the AlGaN MQWs emitting at ~250 nm by Ban, et al., and thus can enable lasing [63]. The root-mean-square (RMS) surface roughness of the AlN template is less than 0.10 nm and 0.12 nm, respectively, as determined by 1×1 μm^2 and 5×5 μm^2 AFM measurements, which are comparable to bulk AlN substrates [70]. Thus the AlN template layer used herein provided a smooth surface for subsequent growth of AlGaN laser structures.

Subsequently, a 90-nm $Al_xGa_{1-x}N$ grading waveguide layer, five periods of 1.2-nm-$Al_{0.66}Ga_{0.34}N$ / 4.9-nm-$Al_{0.83}Ga_{0.17}N$ MQWs designed for laser emission at around 250-255 nm and a thin $Al_{0.83}Ga_{0.17}N$ cap layer for surface passivation and carrier confinement were grown on the AlN template layer sequentially. The composition and thickness of these AlGaN layers were optimized experimentally to improve gain and enhance optical

confinement in the active region and thus reduce threshold. In the future, detailed waveguide modeling will be carried out to further optimize the structure.

7.3 Result and discussion

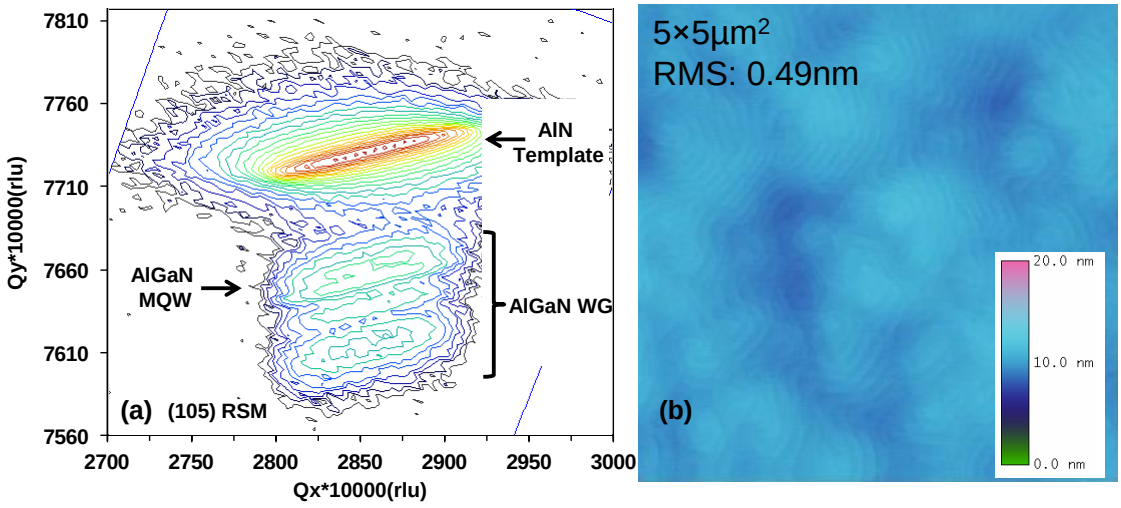

Figure 41. (a) XRD (105) RSM of the laser structure on a (0001) sapphire substrate demonstrating pseudomorphic growth, and (b) 5×5 μm^2 AFM image of surface of the laser structure.

As shown in the asymmetric (105) reciprocal space mapping (RSM) by XRD in Figure 41(a), all the epitaxial layers were pseudomorphically grown and thus fully strained, which retained the quality of the AlN template layer. The 5×5 μm^2 AFM image of Figure 41(b) shows the surface of a MQW laser wafer where terraced step flows were observed, indicating two-dimensional epitaxial growth. The RMS roughness is 0.49 nm.

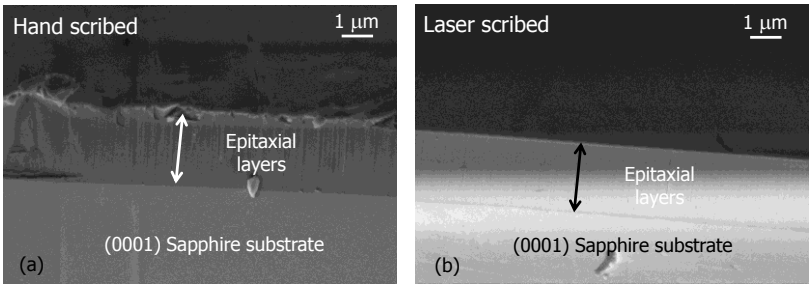

Figure 42. SEM images of (a) hand-scribed and (b) laser-scribed facets, showing the laser-scribed facet is smooth and uniform.

Subsequent to the growth, the wafer was cleaved into Fabry-Perot laser bars with assisted by laser [71] or hand scribing from the back side of the 430 μm-thick sapphire substrates. The widths (cavity lengths) and lengths of the laser bars are 0.6-2.0 mm and equal or more than 10 mm, respectively. The laser scribing was shown to lead to a smoother and more uniform facet than the hand scribing, as shown in Figure 42(a)-(b). The smoother facet leads to higher gain and thus narrower FWHMs, higher slope efficiency, and higher degree of polarization, which will be shown later in this chapter. No high-reflection (HR) coating was applied to facets of the bars as was done in one of our previous studies [72]. Thus the reflectivity of facet is estimated to be ~0.2 by considering the refractive indices of AlGaN MQWs around 250 nm.

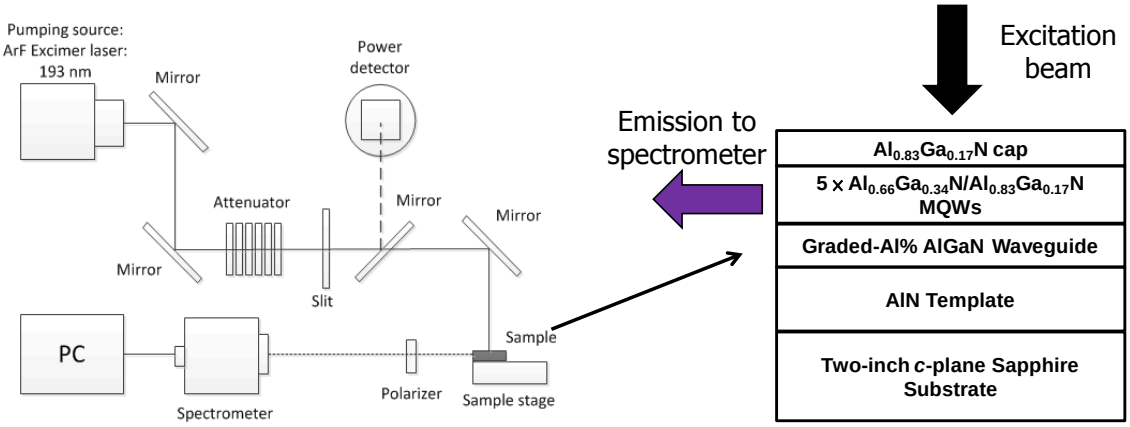

Figure 43. Schematic diagram of laser measurement system.

The laser bar was optically pumped at RT by a Coherent COMPexPro 110-F excimer laser system with a pulse width of 20 ns and frequency of 10 Hz. The laser cavity is filled by excimer mixture containing 0.17% F_2, 5.33% Ar, 16.50% He, and 78% Ne to emit the laser beam at 193 nm, which provides larger excitation photon energy than the highest bandgap of III-nitrides. As shown in Figure 43, the excitation beam emitted from the laser system is firstly deflected by two mirrors. Then the beam passes through an optical

attenuator comprising a plurality of double-side polished sapphire substrates. The number of sapphire substrates was varied during the measurement to provide different excitation densities on the laser bar. The initial excitation beam size (V×H) is 24×10 mm, which is much larger than the laser bar. For the excimer laser, the beam profile is nearly flat-hat in the vertical and horizontal directions. Yet to ensure an excitation laser beam with a uniform wavefront intensity, a rectangular slit with a fixed vertical length of 12.7 mm and an adjustable horizontal width of 0-5 mm is used to utilize the central part of excitation beam. A mirror is used after the slit to deflect the excitation beam to a power meter to measure power density. During the excitation on a laser bar, this mirror is flipped down. Finally, a mirror above the laser bar deflects the beam towards epitaxial surface of the laser bar. The excitation stripe with a dimension of 12.7 × 0-5 mm^2 was perpendicular to the cleaved facets of the laser bars.

As the photons of excitation beam carry a larger energy than bandgaps of the AlGaN heterostructure, they are heavily absorbed and the estimated absorption length is around 100 nm. Upon absorption, electrons and holes are excited in the conduction and valence bands of the heterostructure. Those excited carriers then undergo energy and momentum relaxation towards the bandgap minimum, where they recombine into photons in the form of spontaneous or stimulated emission. The photons emitting from the horizontal laser cavity is then collected by a CCD spectrometer with a resolution of 0.02 nm. An α-BBO polarizer with extinction ratio of 100000:1 can be optionally placed between the laser bar and the spectrometer to measure optical polarization of the emission.

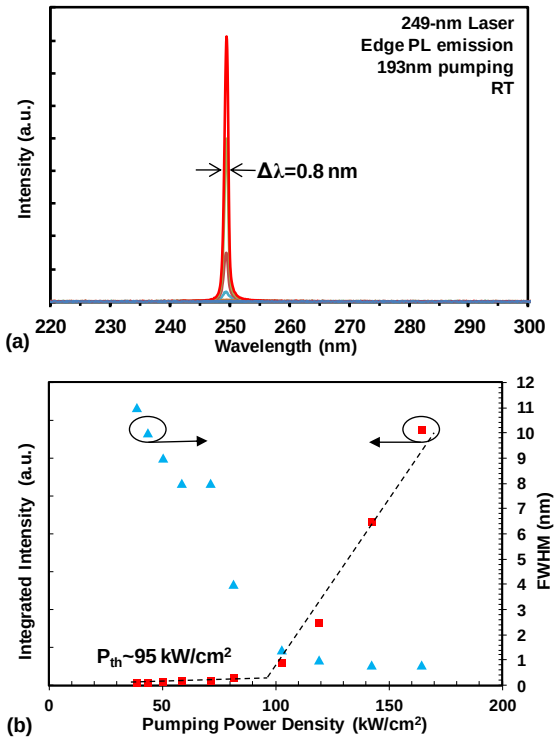

Figure 44. (a) Laser emission spectra and (b) spectral integrated intensity and spectral linewidth versus pumping power densities of the 249-nm laser.

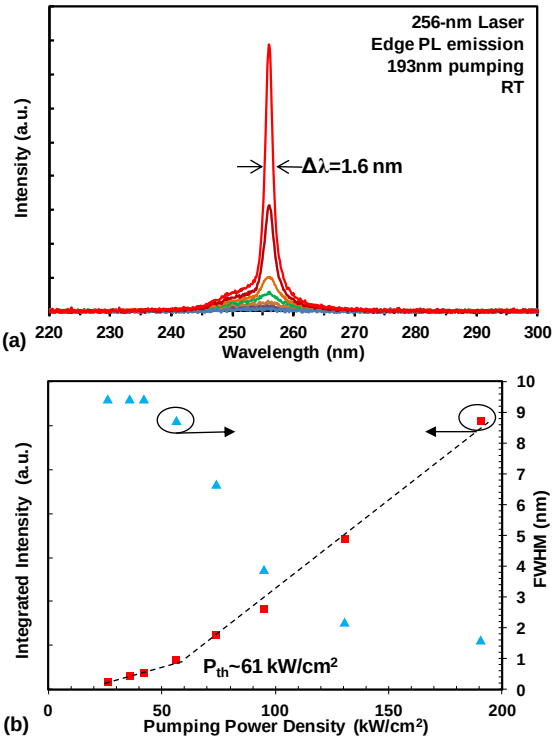

Figure 45. (a) Laser emission spectra and (b) spectral integrated intensity and spectral linewidth versus pumping power densities of the 256-nm laser.

The RT PL spectra of the 249-nm laser and 256-nm laser with pumping power densities below and above the lasing threshold are shown in Figure 44(a) and Figure 45(a), respectively. The 249-nm laser and 256-nm laser were scribed by laser and hand, respectively. The difference of the emission wavelengths of 7 nm between the two lasers is due to normal shift of sample condition between two-inch wafers grown in this MOCVD reactor. The cavity lengths of the 249-nm laser and 256-nm laser are 1.20 mm and 1.17 mm, respectively. In Figure 44(b) and Figure 45(b), the spectral integrated intensities as a function of the pumping power density of the 249-nm laser and the 256-nm laser demonstrate threshold pumping power densities of 95 kW/cm^2 and 61 kW/cm^2, respectively. As also shown in Figure 44(b) and Figure 45(b), spectral linewidth of the 249-nm laser and the 256-nm laser gradually reduces with increasing pumping power density and reaches 0.8 and 1.6 nm at the maximum measured pumping-power density, indicating stimulated emission. The higher slope efficiency and smaller linewidth of the 249-nm laser than those of the 256-nm laser probably result from a smoother and more uniform facet because of the laser scribing. The thresholds are more than an-order-of-magnitude lower than the previously-reported optically-pumped AlGaN MQW DUV laser grown on foreign 4H-SiC substrates [65]. In addition, the thresholds are comparable with the reported state-of-the-art optically-pumped AlGaN MQW DUV lasers grown on bulk AlN substrates lasing at 266 nm with a threshold of 41 kW/cm^2 [73].

It is difficult to explain this comparability without knowing details such as structure, growth conditions, and pumping conditions of Ref. [73]. The AlN substrate possesses much lower TDD than the AlN/sapphire templates used in this study and thus

could potentially lead to a high IQE and an even lower threshold. However, the following studies may shed some light on explaining the comparability of thresholds.

Preliminary results from temperature-dependent PL studies of AlGaN MQWs with different structures grown on the AlN/sapphire templates used in this study show IQE values are in the range of 30% to 56% at 300K at a power density of 134kW/cm^2. A recent study by Martens, et al., have shown that the same AlGaN DUV MQW structure grown on an AlN/sapphire template (TDD ~ 5×10^8 /cm^2) had a higher IQE (20%-30%) than the IQE (10-20%) of that grown on a bulk AlN substrate (TDD ~ 10^4 /cm^2), which was attributed to lateral inhomogeneities and filamenting for AlGaN DUV MQW structure grown on bulk AlN substrates [74]. In addition, Bryan et al., have shown that an unoptimized growth condition of the AlGaN DUV MQW on the AlN substrate can lower the IQE significantly [75]. Moreover, Collazo et al., have shown that bulk AlN substrate can have a high absorption coefficient of $\alpha > 350$ cm^{-1} in the DUV range because of carbon impurities [22] and Xie, et al., show that there was considerable light leakage towards the substrate for the low-threshold optically-pumped DUV MQW laser grown on the AlN substrate because of imperfect optical confinement [68]. Thus the severe absorption could limit the performance of AlGaN DUV MQW laser grown on currently available AlN substrates. These studies indicate that the AlGaN MQW DUV lasers on bulk AlN substrates may exhibit much lower thresholds than the current reported values with further optimized growth condition and reduced absorption in the DUV spectrum.

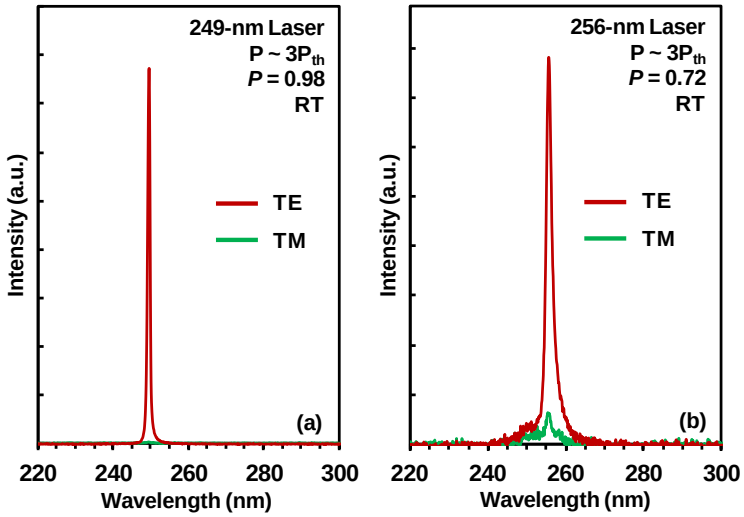

Figure 46. Laser emission spectra of the TE mode and TM mode of the (a) 249-nm laser and (b) 256-nm laser operating above threshold at RT.

Optical polarization of the stimulated emission was measured at RT. Figure 46(a)-(b) shows the transverse electric (TE) and transverse magnetic (TM) emission spectra of the 249-nm laser and 256-nm laser operating at pumping power densities about three times of the respective thresholds. For the 249-nm laser and 256-nm laser, the stimulated emission is strongly TE-polarized with the degree of polarization (P), defined as $P = (I_{TE} - I_{TM}) / (I_{TE} + I_{TM})$, equal to 0.98 and 0.72, respectively. This result indicates the dominant band transition was between the conduction band and heavy hole band for the AlGaN MQW DUV lasers grown on the sapphire substrate emitting at 249 nm and 256 nm, thanks to the pseudomorphic growth and thus strong compressive strain in the MQWs [76]. The result is similar to the stimulated emission polarization measured from the AlGaN MQW DUV lasers grown on AlN substrates at similar emission wavelengths [71].

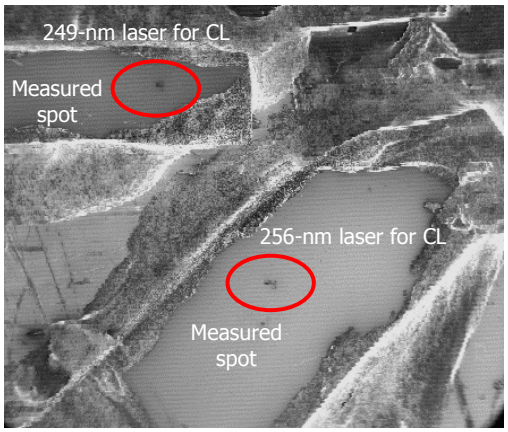

Figure 47. The SEM image showing experimental setup of CL measurement of the laser bars.

CL measurement was conducted at RT on two other laser bars lasing at 249 and 256 nm fabricated from the same wafer. They are referred as “249-nm laser for CL” and “256-nm laser for CL” for distinction from the previous “249-nm laser” and “256-nm laser”. In this experiment, the excitation source is an e-beam targeting the epitaxial surface with a dimension of about 10 nm. Because of the high energy nature and existing carbon contamination in the chamber, the e-beam left dents on the epitaxial surface as highlighted by the red circles in Figure 47. A concave mirror is place above the sample to collect emitted light and reflect them to the monochromator which is connected to a photomultiplier tubes (PMT).

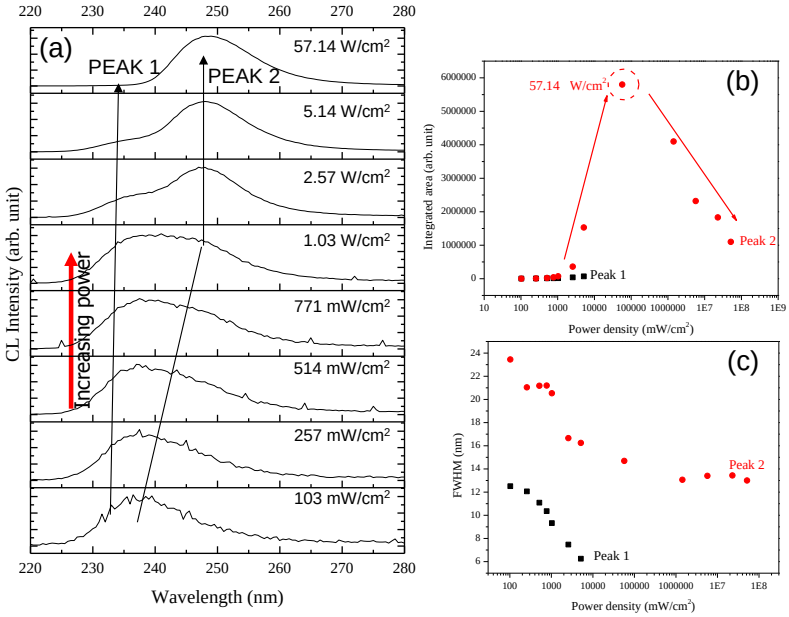

Figure 48. (a) CL spectra, (b) integrated intensity and (c) FWHMs as a function of e-beam excitation densities of the 249-nm laser for CL.

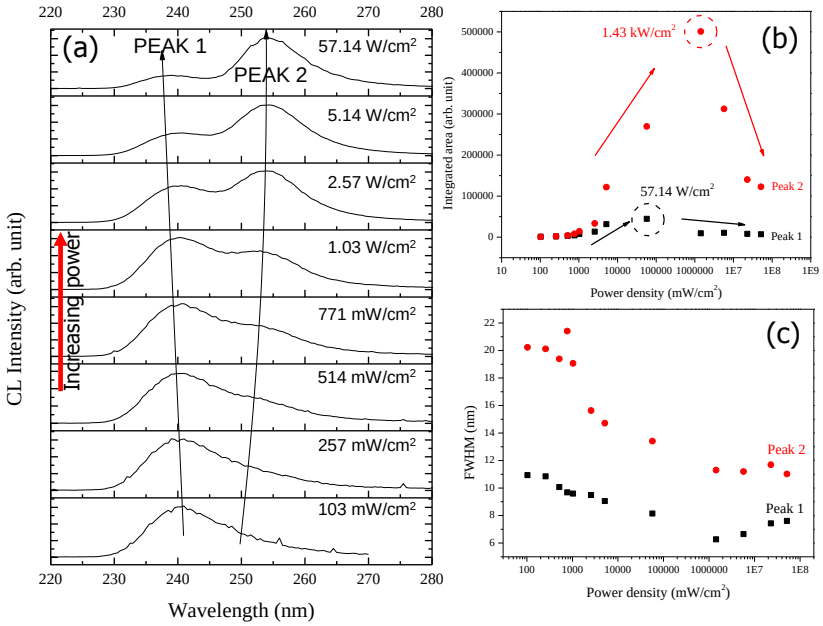

Figure 49. (a) CL spectra, (b) integrated intensity and (c) FWHMs as a function of e-beam excitation densities of the 256-nm laser for CL.

Figure 48(a)-(c) and Figure 49(a)-(c) exhibit CL spectra, integrated intensity and FWHMs as a function of pumping densities. For either sample, a spontaneous emission peak is observed at a shorter wavelength at a low excitation density. As the excitation density increases, a second peak emerges at a longer wavelength. It is related to optical amplification by the vertical cavity between the AlN/sapphire interface and AlGaN cap layer as shown by Figure 48(b) and Figure 49(b), where the integrated intensity of the second peak increases superlinearly as a function of the pumping densities. Though FWHM of the second peak decreases considerably with increased intensity, it is still much larger than that of stimulated emission. This may be attributed to the undesired optical cavity where the AlN/sapphire interview is rough and probably absorbing due to high density of dislocations. Nevertheless, the optical amplification indicates excellent material and structural quality, which is consistent with the optical pumping experiment.

7.4 Conclusion

In summary, we have achieved room-temperature stimulated emission and laser operation from AlGaN MQW DUV heterostructures grown on (0001) sapphire substrates at 249 nm with a threshold of 61 kW/cm^2 and at 256 nm with a threshold of 95 kW/cm^2. The use of relatively low-dislocation-density AlN template layers and the optimization of the growth conditions for the waveguide layer and active region are the keys to enabling low-threshold laser action. The laser emission is dominated by TE-polarized emission, which is comparable to the lasers grown on bulk AlN substrates at similar wavelengths. CL experiment shows strong optical amplification. The results demonstrate excellent candidacy of sapphire substrates for the development of high-performance III-N DUV laser diodes.

8. TRANSVERSE-MAGNETIC DEEP ULTRAVIOLET LASING FROM ALGAN HETEROSTRUCTURES ON SAPPHIRE

8.1 Introduction

The developments of III-nitride deep-ultraviolet (DUV) laser diodes (LDs) and light-emitting diodes (LEDs) have attracted considerable interest for a number of applications such as high-density optical storage and disinfection. Recently, low-threshold optically-pumped DUV lasers containing AlGaN multiple-quantum wells (MQWs) have been demonstrated by employing bulk AlN substrates [11,13,67-69,72,73]. Bulk AlN substrates were utilized because of their low dislocation density as well as reduction of lattice and thermal mismatch between the substrate and Al-rich AlGaN layers, resulting in a low-dislocation density in the MQW active region and thus enhanced gain. However, because of the shortcomings of currently available AlN substrates such as small area, strong DUV absorption, and high cost, it is more desirable to grow the DUV lasers on larger and lower-cost foreign substrates like sapphire that have been widely used to grow smaller-bandgap III-nitride materials. Recently, we have demonstrated optically-pumped AlGaN MQW DUV lasers grown on (0001) sapphire substrates with very low thresholds at 249 nm and 256 nm, indicating that sapphire can be a useful substrate for DUV LDs [77]. The details of this study can be found in the last chapter.

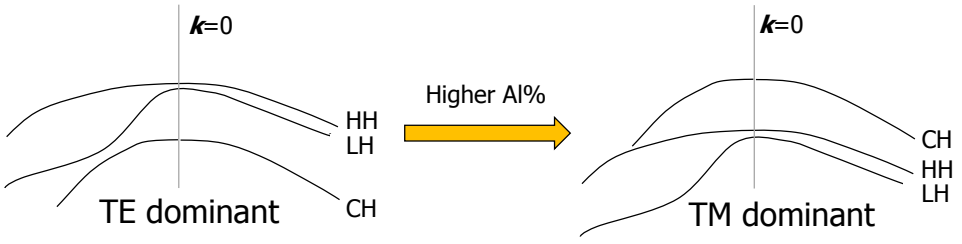

Figure 50. Schematics of topmost valence bands of AlGaN related to polarization switch of band-edge emission.

One interesting property of AlGaN luminescence is the optical polarization determined by transitions between the conduction band and topmost valence band. As shown in Figure 50, When the topmost valence band is the heavy hole (HH) band, the dominant band transition is between the conduction band and HH band which leads to transverse-electric (TE) ($E_{TE} \perp c$-axis) dominant emission. With an increased Al composition and thus a shorter emission wavelength, the split-off hole (CH) band moves closer to the conduction band relative to the HH band, which triggers the switch from TE- to transverse-magnetic (TM)-polarized ($E_{TM} \parallel c$-axis) emission when the CH band crosses over the HH band and thus becomes the topmost band [78,79]. The optical polarization can have a considerable impact on the performance of DUV LEDs and LDs. For top- or bottom-emitting LEDs grown on the (0001) substrates, TM polarization can be detrimental for light extraction efficiency because the TM-polarized light is unlikely to emit from the surface that is parallel to the (0001) because of $E_{TM} \parallel c$-axis [79]. For edge-emitting LDs, TE polarization is also desirable as TE-polarized light does not penetrate as deeply into the smaller-bandgap *p*-type region as for TM-polarized light.

Previously, the above-threshold optical polarization of stimulated emission from optically-pumped AlGaN DUV lasers grown on AlN substrates emitting at 243-281 nm has been reported [11,13,67-69,72,73]. These studies show that TE-polarized stimulated emission was dominant in this wavelength range. For optically-pumped AlGaN DUV lasers grown on (0001) sapphire substrates, TE polarized emission dominated at $\lambda \geq 249$ nm [74,77,80]. Hence there has been no observation of dominant TM-polarized stimulated emission for AlGaN DUV lasers grown on AlN or sapphire substrates to date. There was one report of the optical polarization of stimulated emission from an optically-pumped

AlGaN DUV laser grown on a (0001) SiC substrate, showing TM-dominance at 240.8 nm [79]. However, no TE-dominant lasing has been reported for III-nitride structures on SiC substrates. Therefore, there is a lack of experimental observation of TE-TM switching of stimulated emission from lasers grown on any substrate and thus the valence band crossover for AlGaN DUV lasers, which is important for design of a laser structure with TM-dominant stimulated emission at shorter wavelengths.

In this study, TM-dominant DUV stimulated emission from AlGaN MQW lasers grown on sapphire was demonstrated due to lasing at short wavelengths of 239-243 nm. Optical polarization was analyzed and compared with previous reports. X-ray diffraction (XRD), scanning transmission electron microscopy (STEM), and RT power-dependent photoluminescence (PL) experiments were conducted to characterize the material structure and emission.

8.2 Experiment

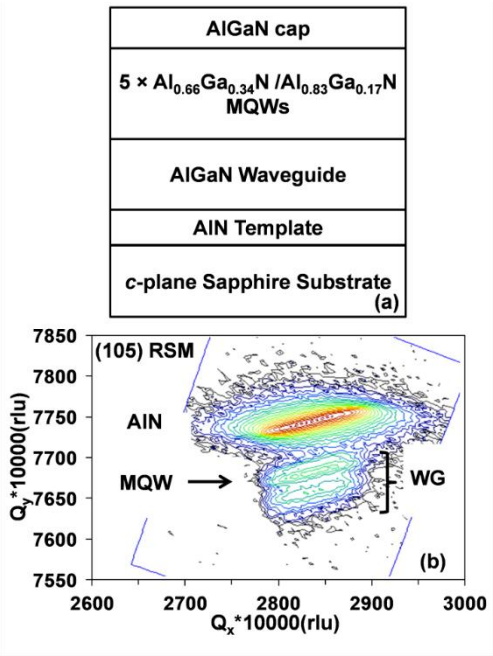

Figure 51. (a) Cross-sectional schematic diagram and (b) XRD (105) RSM of the AlGaN MQW laser structure grown on a (0001) AlN/sapphire template.

As shown schematically in Figure 51(a), the AlGaN DUV laser structure was grown on a two-inch diameter (0001*)* AlN/sapphire template in an AIXTRON 3×2" close-coupled showerhead metalorganic chemical vapor deposition (MOCVD) reactor. The AlN/sapphire template similar to this used in our previous studies for the growth of low-threshold DUV AlGaN lasers emitting at 249 and 256 nm at RT[59,77,81] was utilized in this work. A graded AlGaN waveguide layer was grown on the AlN template, followed by five periods of 1.0-nm-$Al_{0.66}Ga_{0.34}N$ / 4.1-nm-$Al_{0.83}Ga_{0.17}N$ multiple quantum wells (MQWs).

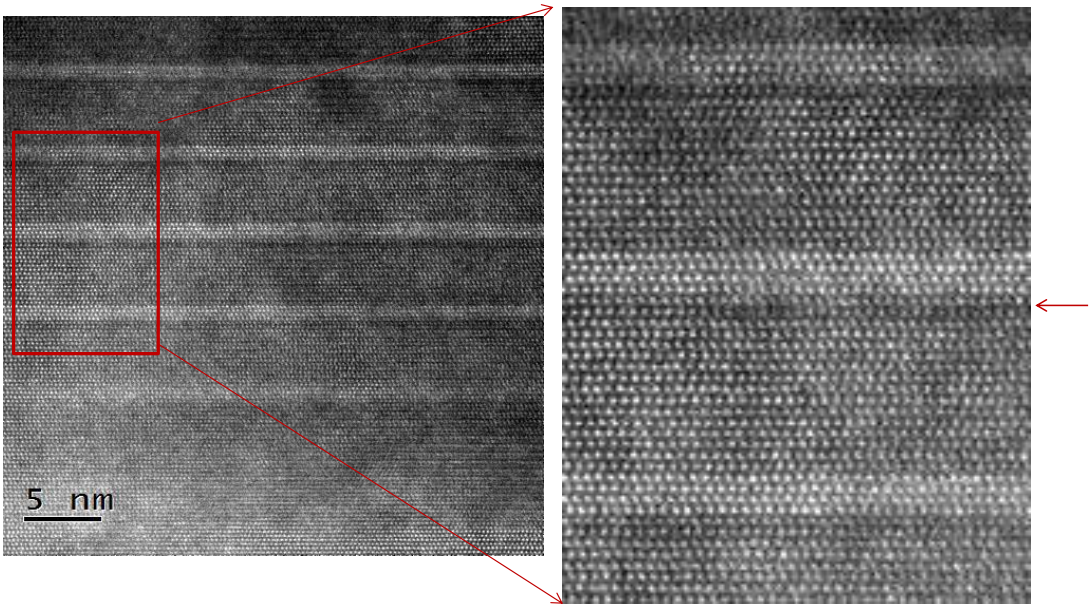

Figure 52. Cross-sectional STEM HAADF images of the MQW active region.

The thicknesses of quantum well and barrier were determined by the high-resolution cross-sectional STEM experiment, as shown in Figure 52. AlGaN instead of AlN was used for the quantum barrier (QB) as the larger bandgap of AlN QB layers can impede carrier transport in an electrically-driven device and the AlGaN QB layers can contribute to better optical confinement in the MQWs because of higher refractive index than that of AlN.

However, it is noted that there is a darker monolayer below each QW as highlighted by the arrow. These are Al-rich monolayers because Al is a lighter element than Ga and thus less scattered and contrasted in the HAADF image. We believe that the primary cause for the Al rich layers is thermal evaporation of Ga in an AlGaN layer. In an MOCVD process at high temperature (>1100C), both growth and desorption processes coexist. As one TMG and TMA source were used and the flow rates were different for QW and QB, the growth switch between QW and QB needed the TMG flow rate to be changed. During this change, there is neither TMG nor TMA injecting onto the wafer surface. Thereby desorption process dominated and took away some Ga in the AlGaN layer, leading to an Al-rich layer. In comparison, Al is more resistant to the thermal desorption because of stronger covalent bond. On one hand, the existence of the Al-rich monolayers may degrade performance of optically-pumped as they reduces overage refractive index of the active region and thus optical confinement. On the other hand, they may increase junction resistance for electrically-pumped lasers despite the small thickness. The Al-rich monolayers may be eliminated by employing two TMG and TMA sources and instantaneous source switching.

The growth was concluded with a thin $Al_{0.83}Ga_{0.17}N$ cap layer for surface passivation. As shown in Figure 51(b), the asymmetric (105) reciprocal space map (RSM) measurements by XRD indicated the AlGaN layers were pseudomorphically grown on the AlN template layer. Thus the structure retained a similar quality and in-plane lattice constant as that of the AlN template layer.

Subsequently, the wafer was cleaved into Fabry-Perot laser bars by mechanical hand scribing from back side of the wafer. No DUV high-reflection coatings were deposited

onto the cavity facets. A pulsed ArF excimer laser (λ = 193 nm) was used to excite the laser bars at room temperature (RT). The excitation laser beam with a controlled degree of attenuation passed through a rectangular aperture with a defined area, and then excited the epitaxial surface of the laser bars uniformly. The in-plane light emission was collected from the laser cavity facet by an optical fiber placed near the facet. The measurements of optical polarization were performed by employing an alpha-BaB_2O_4 (BBO) polarizer. More details of the experimental setup can be found in Chapter 7.

8.3 Result and discussion

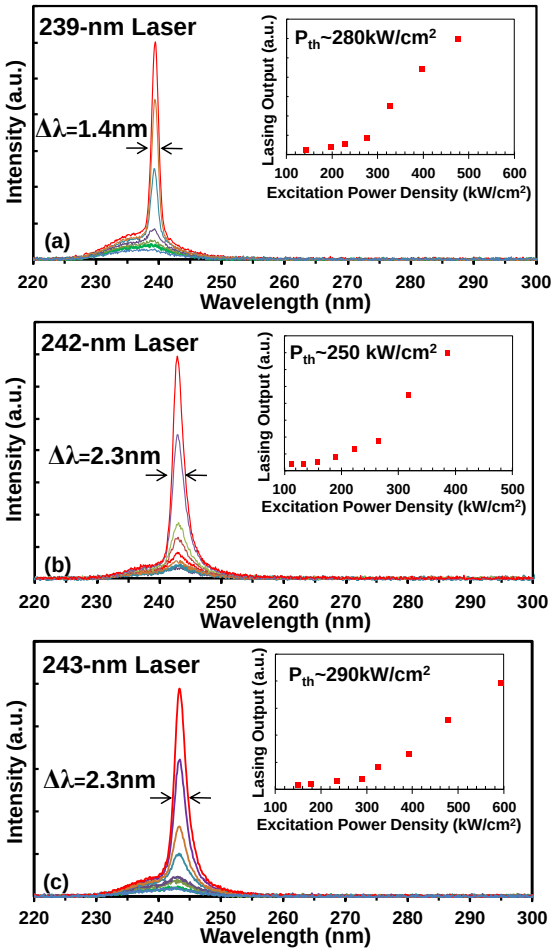

Figure 53. Emission spectra of the (a) 239-nm, (b) 242-nm, and (c) 243-nm lasers by power-dependent PL at RT. The insets show the respective light output intensity of stimulated emission as a function of excitation power density.

Figure 53(a)-(c) show PL spectra of the lasers emitting at 239, 242, and 243 nm under different excitation power densities, respectively. Cavity lengths of the 239-nm, 242-nm, and 243-nm lasers are 1.1, 2.2, and 1.8 mm, respectively. The small wavelength variation of ~4 nm in the emission wavelengths of these lasers are due to lateral wafer inhomogeneities, which can include variation of strain state, composition, layer thickness, and carrier density [16,76,82-84]. As the excitation power density increased, the spectral linewidth narrowed significantly and reached FWHM values of 1.4-2.3 nm at respective maximum excitation power density, which indicated stimulated emission [13,69]. The laser thresholds were estimated to be 280, 250, and 290 kW/cm^2 for the 239-nm, 242-nm, and 243-nm lasers, respectively. These thresholds are lower than those of the reported lasers at similar wavelengths grown on bulk AlN substrates [13,67]. Some possible reasons for lower thresholds were discussed previously, which include impurity absorption within AlN substrate and different designs of laser structures [77]. The stimulated emission peak at 239 nm is the shortest RT lasing wavelength yet reported for AlGaN DUV lasers grown on foreign substrates including sapphire and SiC [74,77,80]. In addition, we have not observed a clear trend where the thresholds are strongly correlated to the cavity length. The small variation of thresholds can be affected by the on-wafer variations of dislocation density, thickness, composition, and strain as well as facet condition.

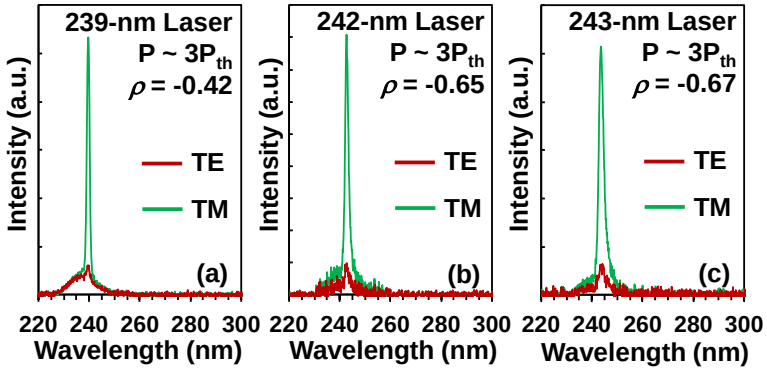

Figure 54. TE- and TM-polarized spectra of the (a) 239-nm, (b) 242-nm, and (c) 243-nm lasers above respective threshold, showing TM-dominant stimulated emission.

Figure 54(a)-(c) show spectra of TE- and TM-polarized laser emission from the 239-nm, 242-nm, and 243-nm lasers operating at about three times as high as their respective threshold (P_{th}). Spectra of the 239-nm, 242-nm, and 243-nm lasers were dominated by TM-polarized stimulated emission accompanied by weak TE-polarized spontaneous emission. This observation of TM-dominant stimulated emission from DUV lasers grown on sapphire substrates is attributed to the short lasing wavelengths of these samples in this study. The polarization degree, defined as $\rho = (I_{TE} - I_{TM}) / (I_{TE} + I_{TM})$, was calculated wherein I_{TE} and I_{TM} represent the integrated spectral intensity of TE- and TM-polarized emission, respectively. The ρ values were -0.40, -0.65, and -0.67 for the 239-nm, 242-nm, and 243-nm lasers, respectively. These results suggest that the dominant interband transition took place between the conduction band and CH valence band for lasing wavelengths equal to or shorter than 243 nm.

Previously, the peak wavelength difference of TE- and TM-polarized emission above threshold was measured to be 1.6 nm ($\lambda_{TE} > \lambda_{TM}$) for the AlGaN MQW laser grown on a bulk AlN substrate which exhibited TE-dominant lasing at 243.5 nm, suggesting an energy separation of ~ 34 meV between the HH and CH bands [13]. However, as shown in

Figure 54(a)-(c), the peak wavelength difference of the TE- and TM-polarized emission above threshold was negligible for all the lasers grown on sapphire. This indicates that the energy separation between the HH and CH bands was minimal. In other words, the HH band and the CH band crossed over for the laser structure employed in this work.

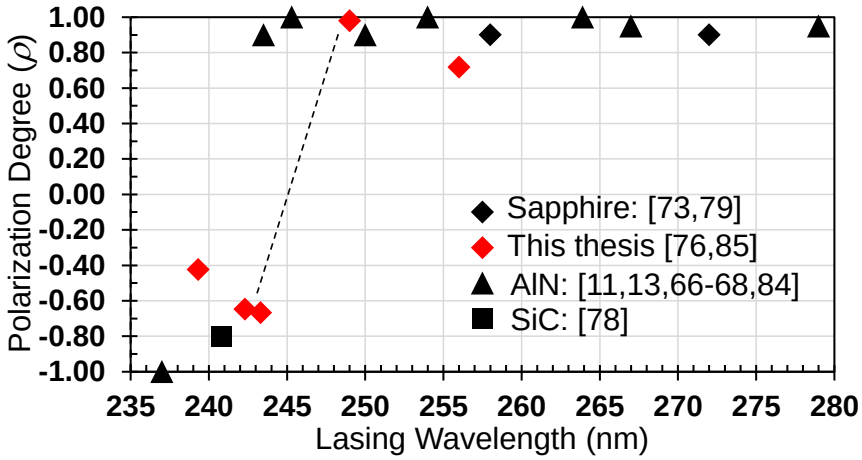

Figure 55. Summary of the reported above-threshold polarization degree (ρ) of DUV lasers grown on AlN, sapphire, and SiC substrates.

Figure 55 summarizes the reported above-threshold polarization degree, ρ, of DUV lasers grown on AlN [11,13,67-69,85], sapphire [74,77,80,86], and SiC [79] substrates. The polarization of laser grown on the SiC substrate was TM-dominant at 240.8 nm. The polarization of lasers grown on AlN substrates was TE-dominant at $\lambda \geq 243.5$ nm and TM-dominant at 237 nm. For the lasers grown on sapphire substrates, the polarization was TE-dominant at $\lambda \geq 249$ nm. Based on this study, the TM-polarized emission dominated the lasing spectra at $\lambda \leq 243$ nm for the lasers grown on sapphire substrates. Thus both TE- and TM-dominant DUV stimulated emission from lasers grown on sapphire has been demonstrated. As indicated by the dashed line in Figure 55, the rapid variation between TE- and TM-dominance with respect to the change in lasing wavelength from 243 to 249 nm is distinct from the previous studies, wherein the spontaneous emission from AlGaN

structures made a similar extent of polarization switch at a considerably longer wavelength span [78,87,88]. This can be attributed to the dramatic change in the ratio of TE-to-TM gain coefficients for the DUV AlGaN MQW lasers in the vicinity of TE-TM switch [82].

8.4 Conclusion

In summary, TM-dominant DUV stimulated emission from optically-pumped AlGaN MQW lasers grown by MOCVD on sapphire substrates were demonstrated at RT. TM-dominant stimulated emission was observed at 239, 242, and 243 nm with low thresholds of less than 300 kW/cm^2. There was no peak wavelength difference of the TE- and TM-polarized emission, indicating crossover of the CH and HH bands in the AlGaN MQWs. The rapid change of polarization between TE- and TM-dominance versus the change in lasing wavelength from 243 to 249 nm suggests a large variation of the ratio of TE-to-TM gain coefficients for the DUV AlGaN MQW lasers near TE-TM switch. Hence this work also provides insights for the design of DUV lasers operating near the TE-TM switch.

9 SINGLE-PHASE WURTZITE BALN LAYER FOR ULTRAVIOLET VERTICAL CAVITY SURFACE EMITTING LASER

9.1 Introduction

Deep ultraviolet (DUV) sources with wavelengths < 280 nm have numerous applications e.g., disinfection and biochemical identification. However, most of the current DUV emitters have limitations in some applications due to a large footprint, fragility and toxicity. III-nitride light emitters are of interest for many UV applications, because the direct bandgap covers a wide DUV range which can lead to compact DUV emitters. However, many important problems remain unsolved. For instance, though relatively low-threshold optically-pumped edge-emitting DUV lasers have been realized on sapphire and AlN substrates [13,77,86], low-threshold DUV vertical-cavity surface-emitting lasers (VCSELs) by either optical pumping or pumping have not yet been demonstrated.

One of the challenges to achieving DUV VCSELs is a lack of high-quality III-nitride distributed Bragg reflectors (DBRs) in the DUV spectrum. The AlGaN material system is a potential candidate for the DBR. However, competing factors such as limited change of refractive index as a function of material composition and transparency with an increased Ga content require a high number of periods for high reflectivity. In addition, the limited index contrast leads to smaller reflector bandwidths. On the other hand, the BAlN material system is a promising alternative candidate. It has a similar bandgap as AlN regardless of B content, thereby being transparent to the DUV emission. Additionally, it was shown that wurtzite BAlN layers with a mere B content of 1% reduced the refractive index at 250 nm by 17%, as compared to AlN [89]. Therefore higher B-content and high-quality wurtzite BAlN layers are expected to create a larger contrast with AlN layers, which

is ideal for wider stopbands and smaller numbers of pairs for high-reflectivity DBRs in the DUV range.

The B content of single-phase high-quality wurtzite BAlN grown by epitaxial growth processes was previously limited to 1-2% [89,90,91]. For instance, Akasaka reported the use of MOCVD in a flow-modulated epitaxy (FME) mode to grow BAlN but achieved a B content of 1.5% [91]. Recently, various efforts have been made to increase the B content in BAlN. For instance, Li obtained a B content of 12% using FME-MOCVD and growing BAlN layers at a low temperature of 650 ^{o}C followed by annealing at 1020 ^{o}C [92]. However, the related x-ray diffraction (XRD) peak intensity was weak and surface roughness was high because of an extremely small critical thickness of formation of cubic crystallinity and columnar poly-crystallinity as a result of the low temperature growth and high B/group-III flow ratio of 39%.

9.2 Experiment

In this work, FME-MOCVD was used to grow ~50-nm thick BAlN layers on 3-μm AlN template layers on (0001) sapphire substrates at relatively high temperatures with the goal of achieving high B-content single-phase wurtzite BAlN layers. The thickness of 50 nm is similar to that of an individual layer of the DBR designed around 300 nm, assuming the index of this layer is ~2. At a shorter wavelength of interest, a thinner than 50-nm BAlN layer would be needed, which is less likely to undergo phase separation compared to a thicker BAlN layer. Therefore it is important to optimize growth conditions to ensure the thickness of a single-phase wurtzite BAlN layer is at least 50 nm. The AlN template has a similar threading dislocation density of low ~10^9 /cm^2 and surface roughness as our previous report [81]. Trimethylaluminium (TMA), Triethylborane (TEB) and NH_3 were

utilized as precursors. Three BAlN layers were grown on three AlN/sapphire templates. Growths of the first and second BAlN layers were performed at relatively high temperatures of 1010 ^{o}C with B/III ratios of 12% and 17% in the vapor phase. The third BAlN layer was grown at 860 ^{o}C with a B/III ratio of 17%. To mitigate severe parasitic reactions between TEB and NH_3, FME was used where alternately a 1-s supply of TMA+TEB and 1-s supply of NH_3 were injected into the growth chamber without interruption for all the three growths. A small V/III ratio of 63 was employed for the same purpose. Subsequent to the growth, X-ray diffraction (XRD), transmission electron microscopy (TEM), and Rutherford backscattering spectrometry (RBS) experiments were performed for characterization.

9.3 Result and discussion

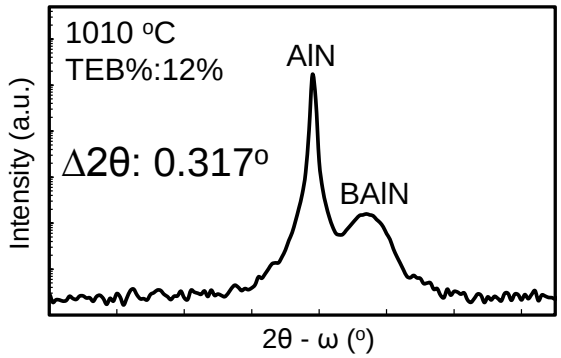

Figure 56. (002) XRD scan of the first BAlN layer grown on AlN/sapphrie template.

Figure 56 shows (002) x-ray diffraction (XRD) peaks of 3-μm AlN template layer and the first BAlN layer at 2θ angles of 36.144^{o} and 36.461^{o}, corresponding to *c*-lattice constants of 4.966 and 4.924Å, respectively. The angular separation Δ2θ is thus 0.317^{o}. The BAlN XRD peak is distinct given the small thickness, indicating good wurtzite crystallinity. It is less probable to accurately determine the B content from XRD alone because of uncertainty of the lattice parameters and strain. However, based on the angular

separation of the XRD peaks and *c*-lattice constant difference, the B content is estimated to be ~6% [92], which is considerably higher than those of high-quality wurtzite BAlN layers reported before [89,91,93].

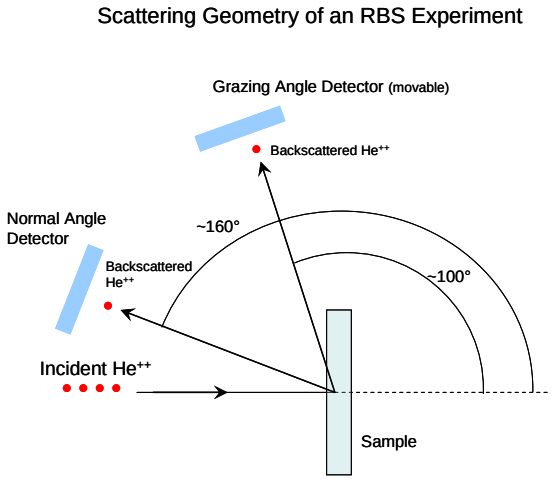

Figure 57. The scattering geometry in the RBS experiment.

To obtain the accurate B content, RBS measurement was conducted on the first BAlN layer. Figure 57 shows the scattering geometry in the RBS experiment [94]. In the compositional analysis, RBS is better than XRD because of independence of strain and defects. RBS spectra were acquired at a backscattering angle of 160^{o} and a grazing angle of 107^{o} with the sample oriented perpendicular to the incident He^{++} ion beam with an energy of 2.275 MeV. The sample was rotated or tilted with a small angle to present a random geometry to the incident beam. This avoids channeling in both the layer and substrate. The use of two detector angles can significantly improve the measurement accuracy for composition when thin surface layers need to be analyzed. Since the BAlN layer is thinner than 100 nm, "ion channeling" was utilized to reduce backscattering signal from the substrate. This results in improved accuracy in the composition of layers

containing elements that overlay with the substrate signal, typically light elements such as oxygen, nitrogen and carbon.

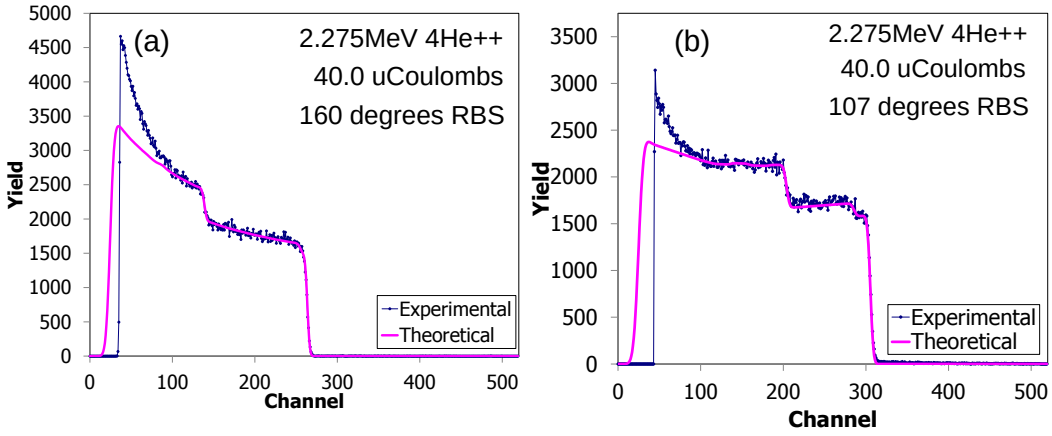

Figure 58. Experimental spectra and theoretical fitting from the detector at the backscattering and grazing angles of (a) 160^{o} and (b) 107^{o}.

As shown by Figure 58 (a)-(b), spectra are fit by applying a theoretical layer model and iteratively adjusting elemental concentrations and thickness until good agreement is found between the theoretical and the experimental spectra. The B-content is determined to be 5.5%, which is consistent with the XRD analysis and represents a much higher content than that of previously reported single-phase wurtzite BAlN [89,91,93].

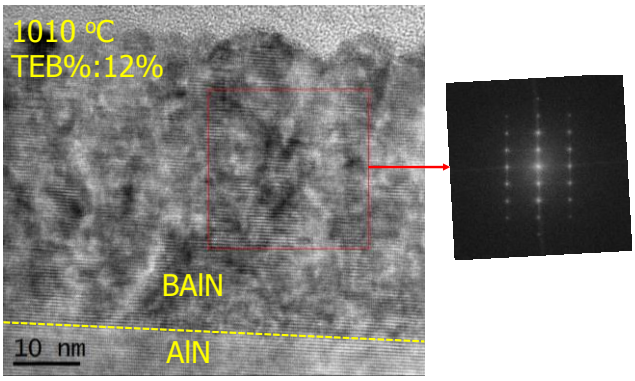

Figure 59. Cross-sectional TEM analysis of the first BAlN layer sample: a high-resolution TEM under *a*-zone axis ([11-20] projection), and (b) the FFT diffraction pattern of one portion of TEM image, showing a wurtzite structure.

Figure 59 shows a high-resolution cross-sectional TEM image taken along the *a*-zone axis ([11-20] projection) and diffraction pattern after fast-Fourier transform (FFT) of the first BAlN layer sample. A sharp interface between the AlN and BAlN layer is observed. In addition, the BAlN film exhibits a highly ordered lattice throughout the entire 50-nm thickness without the polycrystalline columnar structures found in previous reports [92,95]. The FFT image confirms a wurtzite structure oriented along *c*-axis, which is consistent with the XRD analysis related to Figure 56.

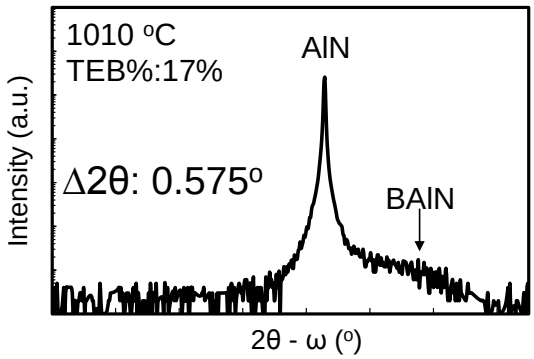

Figure 60. (002) XRD scan of the second BAlN layer sample.

Figure 60 shows the (002) XRD pattern of the second BAlN sample. Though the angular separation Δ2θ between the AlN and BAlN peaks increases to 0.575°, the intensity of BAlN peak is significantly dampened compared with that in Figure 56. This indicates poor wurtzite crystallinity.

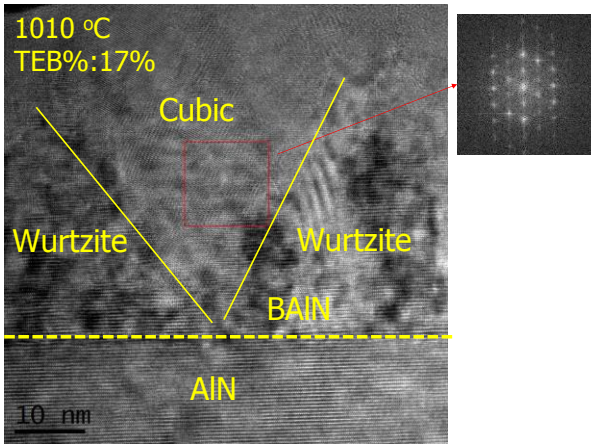

Figure 61. Cross-sectional TEM analysis of the second BAlN layer sample: a high-resolution TEM under *a*-zone axis ([11-20] projection), and the FFT diffraction pattern of the cubic region, showing a cubic structure.

To investigate the crystallinity and microstructure, the high-resolution cross-sectional TEM analysis was conducted similar to the one related to Figure 59. As shown in Figure 61 (a), mixed crystallinities are found including wurtzite and cubic regions. The cubic region originates from the AlN/BAlN interface and gradually expands in size as the BAlN layer thickness becomes larger. It also forms planar interface with the wurtzite structure. It may be caused by B-rich sites at the beginning of BAlN growth due to a higher B/III ratio. It possess highly-tilted lattice with respect to the *c*-plane. It is noted that the dislocation density in the cubic region is much reduced compared to the wurtzite region. This can be because dislocations from the wurtzite region cannot propagate into the cubic region, since the nature of the slip planes and burgers vectors are different. For the hexagonal wurtzite phase, screw dislocations propagate perpendicular to the basal plane with a Burgers vector equal to the c-parameter (about 0.5 nm) while dislocations in the cubic phase are on (111) basal planes and the Burgers vector is about 3 nm. Thus the slip planes and displacement are different in the two crystal structures. As a result, one dislocation cannot propagate from one to the other.

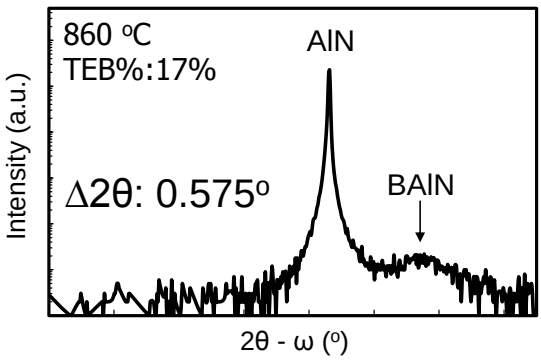

Figure 62. (002) XRD scan of the third BAlN layer sample.

Figure 62 shows the (002) XRD pattern of the third BAlN sample. A distinct BAlN peak is observed. The angular separation Δ2θ between the AlN and BAlN peaks is 0.575°. Based on the angular separation Δ2θ and RBS-determined B content of the first BAlN layer, the B content of the third BAlN layer is estimated to be 10%. The intensity of BAlN peak is relatively stronger compared with that of the second BAlN layer. This implies that a lower temperature is not desired for the formation of cubic structure, though its potentially negative impact on material quality must be taken into account.

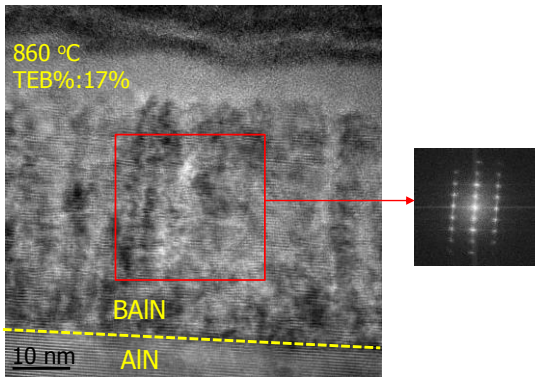

Figure 63. Cross-sectional TEM analysis of the third BAlN layer sample: a high-resolution TEM under *a*-zone axis ([11-20] projection), and the FFT diffraction pattern of one portion of TEM image, showing a wurtzite structure.

The high-resolution cross-sectional TEM analysis was conducted to investigate the crystallinity and microstructure. As shown in Figure 63, the wurtzite crystallinity exists throughout the BAlN layer without observation of the cubic structure. However, there is a

tendency towards formation of columnar, stacking fault, and small-angle grain boundary formation as a result of the use of a lower temperature of 860 ^{o}C. Such issues would need to be resolved for the growth of high performance device containing this material.

9.4 Conclusion

In summary, single-phase wurtzite BAlN layers with relatively high B contents of 5.5% and 10% and a thickness of 50 nm were demonstrated at temperatures of 1010 and 860 ^{o}C with B/III ratios of 12 and 17%, respectively. The formation of BAlN cubic structure was found to happen at the higher B/III ratio of 17% at 1010 ^{o}C. The TEM analysis shows that the cubic structure initiated at the BAlN/AlN interface due to B-rich sites and suppressed the propagation of dislocation from the wurtzite region into itself. Lowering the temperature from 1010 to 860 ^{o}C effectively suppressed the formation of cubic structure at the B/III ratio, though degradation of material quality is observed as a result of the lower temperature.

10 CONCLUSION AND FUTURE WORK

In this dissertation, a variety of studies focusing on III-nitride deep-ultraviolet (DUV) edge-emitting lasers and vertical cavity surface-emitting lasers (VCSELs) on sapphire and AlN substrates have been elaborated. These works have notable significance in the pursuit of electrically-pumped DUV edge-emitting and surface-emitting laser diodes (LDs). Despite meaningful progresses shown in this dissertation, tremendous works are required to grow and fabricate an electrically-pumped DUV LD. These include further advancement and exploration of existing and new works, respectively. Detailed conclusion and future works are shown below.

First, growth of high-Al AlGaN heterostructures at a high temperature of 1250 ^{o}C by metalorganic chemical vapor deposition (MOCVD) was found to lead to transverse electric (TE)-dominant DUV lasing at 266.0 nm with a low threshold of 124 kW/cm^2. Superluminescence at 259.7 nm from surface emission of AlGaN multiple quantum wells (MQWs) on the sapphire substrate was obtained by using the similar growth condition. The 259.7 nm is the shortest reported wavelength for superluminescence from AlGaN MQWs. Thus the high temperature growth shows potential in achieving high quality AlGaN heterostructures which is attributed to enhancement of surface mobility of Al atoms.

Second, a detailed growth temperature dependence study of crystalline quality of AlN layers on sapphire substrates was conducted at 1050-1250 ^{o}C by MOCVD. At lower temperatures, the AlN layers show inferior quality with surface pits and high X-ray diffraction (XRD) ω-scan full-width at half maximums (FWHMs) due to insufficient Al atom mobility. At a large temperature range of 1086-1212 ^{o}C, smooth and coalesced surface was obtained and the XRD FWHMs reduced significantly. This indicates sufficient

Al atom mobility in this range that was largely considered to be low for the AlN layer growth by MOCVD. Above 1212 ^{o}C, longer diffusion lengths of Al atoms than the step terrace width formed surface macro-steps, increasing surface roughness. This study suggests that high-quality AlN layers on sapphire may be achieved at a temperature as low as 1086 ^{o}C which is reachable by most of the III-nitride MOCVD systems.

Third, a simple three-step method was developed to grow high-quality planar AlN layers on sapphire substrates at relatively low temperatures without the use of epitaxial lateral overgrowth (ELO) or pulse atomic layer epitaxy (PALE) methods. The three-layer structure comprised a 15-nm thick buffer layer, a 50-nm thick intermediate layer, and a 3.4-μm thick AlN layer grown at temperatures up to 1130^{o}C. The AlN layer surface had low root-mean-square (RMS) roughness of 0.50 and 0.07 nm for 20×20 and 1×1 μm^2 AFM scans. Band-edge emission was observed at 208 nm and the total threading dislocation density was 2.5×10^9 /cm^2, comparable to those of some AlN layers grown at significantly higher temperatures. The residual impurity concentrations were also comparable to those of AlN layers grown at higher temperatures. This study shows that high quality AlN layers on sapphire can be grown at achievable temperatures for most of the MOCVD systems. In future, efforts are needed to continue to bring down the dislocation density to low 10^8 cm^{-2} for a high internal quantum efficiency close to unity.

Fourth, state-of-the-art optically-pumped DUV lasers were demonstrated at 256 and 249 nm with record-low thresholds of 61 and 95 kW/cm^2 at room temperature (RT) from AlGaN heterostructures on sapphire substrates. These low thresholds are attributed to the optimization of active region and waveguide layer as well as the use of high-quality AlN layers on sapphire. The lasing above threshold was dominated by transverse-electric

(TE) polarization indicating the heavy-hole (HH) band was the upmost valence band in the AlGaN MQWs.

Fifth, transverse-magnetic (TM) dominant DUV lasers was demonstrated from optically-pumped AlGaN heterostructures on sapphire at RT. The lasers at 239, 242, and 243 nm had low thresholds of 280, 250, and 290 kW/cm^2, respectively. The crystal-field split-off hole (CH) and HH valence bands crossed as shown by no peak wavelength difference between the TE-polarized and TM-polarized emission. The reported polarization of optically-pumped lasers was summarized, showing rapid variation of polarization between TE- and TM-dominance at 243-249 nm for the lasers on sapphire. This is attributed to a dramatic change in the TE-to-TM gain coefficient ratio in the vicinity of TE-TM switch. In future, successful p-doping of high-Al AlGaN or other suitable materials is required to eventually pave the way for an electrically-pumped LD.

Sixth, single-phase wurtzite BAlN layers with high-B content of up to 10% were grown by MOCVD. This is important for the development of III-nitride distributed Bragg reflectors (DBRs) for vertical cavity surface-emitting lasers (VCSELs), because such materials are expected to be optically transparent, and have large refractive index contrast and close lattice with high-Al AlGaN materials. In future, it is important to obtain thick BAlN/AlN or BAlN/AlGaN DBRs with abrupt interfaces and maintain the wurtzite structure to achieve high reflectivity and large stopband. Doping studies of BAlN materials is also needed to obtain conductive DBRs.

REFERENCES

[1] H. Morkoc, Handbook of Nitride Semiconductors and Devices, vol. 1, WILEY-VCH Verlag GmbH & Co. KGaA, Weinheim (2008).

[2] Modified from the image in Gallium nitride. In Wikipedia, the Free Encyclopedia (2015).

[3] J. H. Edgar, Properties of Group III Nitrides (1994).

[4] H. M. Manasevit, Appl. Phys. Lett. 12, 156 (1968).

[5] Courtesy of AIXTRON SE.

[6] K. H. Li, X. Liu, Q. Wang, S. Zhao and Z. Mi, Nat. Nanotechnol. 10, 140 (2015).

[7] S. Zhao, X. Liu and Z. Mi, presented at the 57th Electronic Materials Conference, Columbus, Ohio, USA, 25 June 2015.

[8] H. Yoshida, Y. Yamashita, M. Kuwabara, and H. Kan, Appl. Phys. Lett. 93, 241106 (2008).

[9] T. C. Lu, T. T. Kao, S. W. Chen, C. C. Kao, H. C. Kuo, and S. C. Wang, Appl. Phys. Lett. 92, 141102 (2008).

[10] K. Omae, Y. Higuchi, K. Nakagawa, H. Matsumura, and T. Mukai, Appl. Phys. Express 2, 052101 (2009).

[11] T. Wunderer, C. Chua, Z. Yang, J. Northrup, N. Johnson, G. Garrett, H. Shen, and M. Wraback, Appl. Phys. Express 4, 092101 (2011).

[12] Z. Lochner, X. H. Li, T. T. Kao, Md. M. Satter, H. J. Kim, S. C. Shen, P. D. Yoder, J. H. Ryou, R. D. Dupuis, K. Sun, Y. O. Wei, T. Li, A. M. Fischer, and F. A. Ponce, Phys. Status Solidi A 210, 9 (2013).

[13] Z. Lochner, T. T. Kao, Y. S. Liu, X. H. Li, Md. M. Satter, S. C. Shen, P. D. Yoder, J. H. Ryou, R. D. Dupuis, Y. O. Wei, H. Xie, A. M. Fischer, and F. A. Ponce, Appl. Phys. Lett. 102, 101110 (2013).

[14] M. Imura, H. Sugimura, N. Okada, M. Iwaya, S. Kamiyama, H. Amano, I. Akasaki, and A. Bandoh, J. Cryst. Growth 310, 2308 (2008).

[15] J. Mickevicius, J. Jurkevicius, K. Kazlauskas, A. Zukauskas, G. Tamulaitis, M. S. Shur, M. Shatalov, J. Yang, and R. Gaska, Appl. Phys. Lett. 100, 081902 (2012)

[16] W. W. Chow and M. Kneissl, J. Appl. Phys. 98, 114502 (2005).

[17] V. N. Jmerik, A. M. Mizerov, A. A. Sitnikova, P. S. Kop'ev, S. V. Ivanov, E. V. Lutsenko, N. P. Tarasuk, N. V. Rzheutskii, and G. P. Yablonskii, Appl. Phys. Lett. 96, 141112 (2010).

[18] M. Imura, H. Sugimura, N. Okada, M. Iwaya, S. Kamiyama, H. Amano, I. Akasaki, and A. Bandoh, J. Cryst. Growth 310, 2308 (2008).

[19] G. Liu, J. Zhang, X. H. Li, G. S. Huang, T. Paskova, K. R. Evans, H. Zhao, and N. Tansu, J. Crystal Growth, 340, 66 (2012).

[20] Courtesy of Monocrystal.

[21] Courtesy of Hexatech Inc.

[22] R. Collazo, J. Xie, B. E. Gaddy, Z. Bryan, B. Kirste, M. Hoffmann, R. Dalmau, B. Moody, Y. Kumagai, T. Nagashima, Y. Kubota, T. Kinoshita, A. Koukitu, D. L. Irving and Z. Sitar, Appl. Phys. Lett. 100, 191914 (2012).

[23] M. Kneissl, T. Kolbe, C. Chua, V. Kueller, N. Lobo, J. Stellmach, A. Knauer, H. Rodriguez, S. Einfeldt, Z. Yang, N. M. Johnson, and M. Weyers, Semicond. Sci. Tech. 26, 1 (2011).

[24] H. Hirayama, S. Fujikawa, N. Noguchi, J. Norimatsu, T. Takano, K. Tsubaki, and N. Kamata, Phys. Status Solidi A 206, 1176 (2009).

[25] U. Zeimer, V. Kueller, A. Knauer, A. Mogilatenko, M. Weyers, and M. Kneissl, J. Cryst. Growth 377, 32 (2013).

[26] H. Hirayama, S. Fujikawa, J. Norimatsu, T. Takano, K. Tsubaki, and N. Kamata, Phys. Status Solidi C 6, S2, S356 (2009).

[27] M. Imura, K. Nakano, G. Narita, N. Fujimoto, N. Okada, K. Balakrishnan, M. Iwaya, S. Kamiyama, H. Amano, I. Akasaki, T. Noro, T. Takagi, and A. Bandoh, J. Cryst. Growth 298, 257 (2007).

[28] Z. Chen, R. S. Q. Fareed, M. Gaevski, V. Adivarahan, J. W. Yang, J. Mei, F. A. Ponce, and M. A. Khan, Appl. Phys. Lett. 89, 081905 (2006).

[29] L. Jastrzebski, J. Cryst. Growth 63, 493 (1983).

[30] R. P. Gale, R. W. McClelland, C. C. Fan, and C. O. Bozler, Appl. Phys. Lett. 41, 545 (1982).

[31] P. Vohl, C. O. Bozler, R. W. McClelland, A. Chu, and A. J. Strauss, J. Cryst. Growth 56, 410 (1982).

[32] O. H. Nam, M. D. Bremser, T. S. Zheleva, and R. F. Davis, Appl. Phys. Lett. 71, 2638 (1997).

[33] Y. Takahashi, H. Imai, M. Hosaka, M. Kawasaki, and I. Sunagawa, Eur. J. Mineral. 16, 6 (2004).

[34] Q. Paduano and D. Weyburne, Jpn. J. of Appl. Phys. 44, 4 (2005).

[35] Z. Chen, S. Newman, D. Brown, R. Chung, S. Keller, U. K. Mishra, S. P. Denbaars, and S. Nakamura, Appl. Phys. Lett. 93, 191906 (2008).

[36] F. Brunner, H. Protzmann, M. Heuken, A. Knauer, M. Weyers, and M. Kneissl, Phys. Status Solidi C 5, 1799 (2008).

[37] O. Reentila, F. Brunner, A. Knauer, A. Mogilatenko, W. Neumann, H. Protzmann, M. Heuken, M. Kneissl, M. Weyers, and G. Trankle, J. Cryst. Growth 310, 4932 (2008).

[38] M. Imura, K. Nakano, N. Fujimoto, N. Okada, K. Balakrishnan, M. Iwaya, S. Kamiyama, H. Amano, I. Akasaki, T. Noro, T. Takagi, and A. Bandoh, Jpn. J. Appl. Phys. 46, 1 (2007).

[39] N. Okada, N. Kato, S. Sato, T. Sumii, T. Nagai, N. Fujimoto, M. Imura, K. Balakrishnan, M. Iwaya, S. Kamiyama, H. Amano, I. Akasaki, H. Maruyama, T. Takagi, T. Noro, and A. Bandoh, J. Cryst. Growth 298, 349 (2007).

[40] M. Imura, K. Nakano, T. Kitano, N. Fujimoto, N. Okada, K. Balakrishnan, M. Iwaya, S. Kamiyama, H. Amano, I. Akasaki, K. Shimono, T. Noro, T. Takagi, and A. Bandoh, Phys. Status Solidi C 203, 1626 (2006).

[41] M. L. Nakarmi, B. Cai, J. Y. Lin, and H. X. Jiang, Phys. Status Solidi A 209, 1 (2012).

[42] N. Fujimoto, T. Kitano, G. Narita, N. Okada, K. Balakrishnan, M. Iwaya, S. Kamiyama, H. Amano, I. Akasaki, K. Shimono, T. Noro, T. Takagi, and A. Bandoh, Phys. Status Solidi C 3, 6 (2006).

[43] S. Hearne, E. Chason, J. Han, J. A. Floro, J. Figiel, J. Hunter, H. Amano and I. S. T. Tsong, Appl. Phys. Lett. 74, 356 (1999).

[44] V. Hoffmann, A. Knauer, C. Brunner, S. Einfeldt, M. Weyers, G. Trankle, K. Haberland, J.-T. Zettler, and M. Kneissl, J. Cryst. Growth 315, 5 (2011).

[45] N. Kato, S. Sato, H. Sugimura, T. Sumii, N. Okada, M. Imura, M. Iwaya, S. Kamiyama, H. Amano, I. Akasaki, H. Maruyama, T. Takagi, and A. Bandoh, Phys. Status Solidi C 5, 6 (2008).

[46] A. Kakanakova-Georgieva, D. Nilsson, and E. Janze´n, J. Cryst. Growth 338, 52 (2012).

[47] J. P. Zhang, H. M. Wang, W. H. Sun, V. Adivarahan, S. Wu, A. Chitnis, C. Q. Chen, M. Shatalov, E. Kuokstis, J. W. Yang, and M. Asif Khan, J. Electron Mater. 32, 5 (2003).

[48] Y. Wu, A. Hanlon, J. F. Kaeding, R. Sharma, P. T. Fini, S. Nakamura, and J. S. Speck, Appl. Phys. Lett. 84, 912 (2004).

[49] H. Li, T. C. Sadler, and P. J. Parbrook, J. Cryst. Growth 383, 72 (2013).

[50] M. Kneissl, Z. Yang, M. Teepe, C. Knollenberg, O. Schmidt, P. Kiesel, N. M. Johnson, S. Schujman, and L. J. Schowalter, J. of Appl. Phys. 101, 123103 (2007).

[51] X. Q. Shen, M. Shimizu, and H. Okumura, Jpn. J. Appl. Phys. 42, 1293 (2003).

[52] X. Q. Shen, H. Matsuhata, and M. Shimizu, Appl. Phys. Lett. 111, 103529 (2005).

[53] X. Q. Shen, H. Matsuhata, T. Ide, and M. Shimizu, J. Appl. Phys. 111, 103529 (2012).

[54] A. Kakanakova-Georgieva, R. R. Ciechonski, U. Forsberg, A. Lundskog, and E. Janzen, Cryst. Growth Des. 9 (2), 880 (2009).

[55] A. Rice, R. Collazo, J. Tweedie, R. Dalmau, S. Mita, J. Xie, and Z. Sitar, J. Appl. Phys. 108, 043510 (2010).

[56] B. N. Pantha, R. Dahal, M. L. Nakarmi, N. Nepal, J. Li, J. Y. Lin, H. X. Jiang, Q. S. Paduano, and D. Weyburne, Appl. Phys. Lett. 90, 241101 (2007).

[57] K. Kanaya and S. Okayama, J. Phys. D: Appl. Phys. 5 43 (1972).

[58] Z. Bryan, I. Bryan, S. Mita, J. Tweedie, Z. Sitar, and R. Collazo, Appl. Phys. Lett. 106, 232101 (2015).

[59] X. H. Li, Y. O. Wei, S. Wang, H. Xie, T. T. Kao, Md. M. Satter, S. C. Shen, P. D. Yoder, T. Detchprohm, R. D. Dupuis, A. M. Fischer, and F. A. Ponce, J. of Cryst. Growth. 414, 76 (2015).

[60] X. H. Li, J. H. Ryou, T. Detchprohm, and R. D. Dupuis, unpublished, wherein the AlN layer was grown under similar conditions as the AlN template layer in this study except that the growth temperature was 1300 ºC.

[61] M. A. Khan, M. Shatalov, H. P. Maruska, H. M. Wang, and E. Kuokstis, Jpn. J. Appl. Phys. 44, 7191 (2005).

[62] D. Lester, F. A. Ponce, M. G. Craford, and D. A. Steigerwald, Appl. Phys. Lett. 66, 1249 (1995).

[63] K. Ban, J. I. Yamamoto, K. Takeda, K. Ide, M. Iwaya, T. Takeuchi, S. Kamiyama, I. Akasaki, and H. Amano, Appl. Phys. Express 4, 052101 (2011).

[64] H. Hirayama, T. Yatabe, N. Noguchi, T. Ohashi, and N. Kamata, Appl. Phys. Lett. 91, 071901 (2007).

[65] T. Takano, Y. Narita, A. Horiuchi, and H. Kawanishi, Appl. Phys. Lett. 18, 3567 (2004).

[66] H. Sun, J. Woodward, J. Yin, A. Moldawer, E. F. Pecora, A. Y. Nikiforov, L. D. Negro, R. Paiella, K. Ludwig, D. J. Smith, and T. D. Moustakas, J. Vac. Sci. Technol. B 31, 03C117 (2013).

[67] Y. S. Liu, Z. Lochner, T. T. Kao, Md. M. Satter, X. H. Li, J. H. Ryou, S. C. Shen, P. D. Yoder, R. D. Dupuis, Y. O. Wei, H. Xie, A. M. Fischer, and F. A. Ponce, Phys. Status Solidi C 11, 2 (2014).

[68] J. Xie, S. Mita, Z Bryan, W. Guo, L. Hussey, B. Moody, R. Schlesser, R. Kirste, M. Gerhold, R. Collazo, and Z. Sitar, Appl. Phys. Lett. 102, 171102 (2013).

[69] W. Guo, Z Bryan, J. Xie, R. Kirste, S. Mita, I. Bryan, L. Hussey, M. Bobea, B. Haidet, M. Gerhold, R. Collazo, and Z. Sitar, J. Appl. Phys. 115, 10 (2014).

[70] A. Rice, R. Collazo, J. Tweedie, R. Dalmau, S. Mita, J. Xie, and Z. Sitar, J. Appl. Phys. 108 043510 (2010).

[71] J. R. van Look, S. Einfeldt, O. Kruger, V. Hoffmann, A. Knauer, M. Weyers, P. Vogt, and M. Kneissl, Photon. Technol. Lett. 22, 6 (2010).

[72] T. T. Kao, Y. S. Liu, Md. M. Satter, X. H. Li, Z. Lochner, J. H. Ryou, P. D. Yoder, T. Detchprohm, Y. O. Wei, H. Xie, A. M. Fischer, F. A. Ponce, R. D. Dupuis, and S. C. Shen, Appl. Phys. Lett. 103, 211103 (2013).

[73] N. M. Johnson, B. Cheng, S. Choi, C. L. Chua, C. Knollenberg, J. E. Northrup, M. R. Teepe, T. Wunderer, and Z. Yang, presented at the 9th International Symposium on Semiconductor Light Emitting Devices, Berlin, Germany, 23 July 2012.

[74] M. Martens, F. Mehnke, C. Kuhn, C. Reich, V. Kueller, A. Knauer, C. Netzel, C. Hartmann, J. Wollweber, J. Rass, T. Wernicke, M. Bickermann, M. Weyers, and M. Kneissl, Photon. Technol. Lett. 26, 4 (2014).

[75] Z. Bryan, I. Bryan, J. Xie, S. Mita, Z. Sitar, and R. Collazo, Appl. Phys. Lett. 106, 142107 (2015).

[76] J. E. Northrup, C. L. Chua, Z. Yang, T. Wunderer, M. Kneissl, N. M. Johnson, and T. Kolbe, Appl. Phys. Lett. 100, 021101 (2012).

[77] X. H. Li, T. Detchprohm, T. T. Kao, Md. M. Satter, S. C. Shen, P. D. Yoder, R. D. Dupuis, S. Wang, Y. O. Wei, H. Xie, A. M. Fischer, F. A. Ponce, T. Wernicke, C. Reich, M. Martens, and M. Kneissl, Appl. Phys. Lett. 105, 141106 (2014).

[78] K. B. Nam, J. Li, M. L. Nakarmi, J. Y. Lin, and H. X. Jiang, Appl. Phys. Lett. 84, 5264 (2004).

[79] H. Kawanishi, M. Senuma, and T. Nukui, Appl. Phys. Lett. 89, 041126 (2006).

[80] S. V. Ivanov, D V Nechaev, A. A. Sitnikova, V. V. Ratnikov, M. A. Yagovkina, N. V. Rzheutskii, E. V. Lutsenko, and V. N. Jmerik, Semicond. Sci. Technol. 29, 084008 (2014).

[81] X. H. Li, S. Wang, H. Xie, Y. O. Wei, T. T. Kao, Md. M. Satter, S. C. Shen, P. D. Yoder, T. Detchprohm, R. D. Dupuis, A. M. Fischer, and F. A. Ponce, Phys. Status Solidi B 252, 5 (2015).

[82] J. Zhang, H. Zhao, and N. Tansu, Appl. Phys. Lett. 97, 111105 (2010).

[83] T. M. Al Tahtamouni, J. Y. Lin, and H. X. Jiang, Appl. Phys. Lett. 101, 042103 (2012).

[84] S. H. Park and J. I. Shim, Appl. Phys. Lett. 102, 221109 (2013).

[85] Z. Bryan, I. Bryan, S. Mita, J. Tweedie, Z. Sitar, and R. Collazo, Appl. Phys. Lett. 106, 232101 (2015).

[86] X. H. Li, T. T. Kao, Md. M. Satter, Y. O. Wei, S. Wang, H. Xie, S. C. Shen, P. D. Yoder, A. M. Fischer, F. A. Ponce, T. Detchprohm, and R. D. Dupuis, Appl. Phys. Lett. 106, 041115 (2015).

[87] T. Kolbe, A. Knauer, C. Chua, Z. Yang, S. Einfeldt, P. Vogt, N. M. Johnson, M. Weyers, and M. Kneissl, Appl. Phys. Lett. 97, 171105 (2010).

[88] R. G. Banal, M. Funato, and Y. Kawakami, Phys. Rev. B 79, 121308 (2009).

[89] S. Watanabe, T. Takano, K. Jinen, J. Yamamoto, and H. Kawanishi, Phys. Status Solidi C 0, 2691 (2003).

[90] A. Nakajima, Y. Furukawa, H. Yokoya, and H. Yonezu, J. Cryst. Growth, 278, 437 (2005).

[91] T. Akasaka and T. Makimoto, Appl. Phys. Lett. 88, 041902 (2006).

[92] X. Li, S. Sundaram, Y. E. Gmili, T. Moudakir, F. Genty, S. Bouchoule, G. Patriarche, R. D. Dupuis, P. L. Voss, J. P. Salvestrini, and A. Ougazzaden, Phys. Status Solidi A 212, 4 (2015).

[93] A. Y. Polyakov, M. Shin, W. Qian, M. Skowronski, D. W. Greve, and R. G. Wilson, J. Appl. Phys. 81, 1715 (1997).

[94] Courtesy of Evans Analytical Group.

[95] X. Li, S. Sundaram, Y. El Gmili, F. Genty, S. Bouchoule, G. Patriache, P. Disseix, F. Réveret, J. Leymarie, J.-P. Salvestrini, R. D. Dupuis, P. L. Voss, and A. Ougazzaden, J. of Cryst. Growth. 414, 119 (2015).